8-2020

Characterizing the Unsteady Dynamics of Cylinder-Induced Shock Wave/Transitional Boundary Layer Interactions Using Non-Intrusive Diagnostics

Elizabeth Lara Lash
elash@utk.edu

To the Graduate Council:

I am submitting herewith a dissertation written by Elizabeth Lara Lash entitled "Characterizing the Unsteady Dynamics of Cylinder-Induced Shock Wave/Transitional Boundary Layer Interactions Using Non-Intrusive Diagnostics." I have examined the final electronic copy of this dissertation for form and content and recommend that it be accepted in partial fulfillment of the requirements for the degree of Doctor of Philosophy, with a major in Aerospace Engineering.

John D. Schmisseur, Major Professor

We have read this dissertation and recommend its acceptance:

Phillip A. Kreth, James Coder, Kivanc Ekici, Ryan Glasby, Christopher Combs

Accepted for the Council:

Dixie L. Thompson

Vice Provost and Dean of the Graduate School

(Original signatures are on file with official student records.)

Characterizing the Unsteady Dynamics of Cylinder-Induced Shock Wave/Transitional Boundary Layer Interactions Using Non-Intrusive Diagnostics

A Dissertation Presented for the

Doctor of Philosophy

Degree

The University of Tennessee, Knoxville

Elizabeth Lara Lash

August 2020

To my parents for their never-ending love and support. And to my family, without whom I would not be the person I am today.

ACKNOWLEDGEMENTS

I would first like to thank my parents, Terry Lash and Liz Vogt, and my brother, Benjamin Lash, for their love and for their confidence and support during this effort. I would also like to thank Erica O'Brien and Diana Giulietti for their encouragement, love, and friendship. Additionally, I would like to thank my advisor, Dr. John Schmisseur, and my dissertation committee: Dr. Phillip Kreth, Dr. Christopher Combs, Dr. James Coder, Dr. Kivanc Ekici, and Dr. Ryan Glasby for their time and attention during this process. There is an entire community at UTSI that works to support student research; in particular, I'd like to thank Gary Payne and Jack LeGeune of the UTSI machine shop for model fabrication, and I'd like to thank research technicians Joel Davenport, Kirk Davenport, Jonathan Kolwyck, and Andrew Davis for wind tunnel testing and support. I'd also like to thank the students and staff of the HORIZON Research Group for their expertise and support towards this effort, particularly Dr. Mark Gragston, James Chism, and Lauren Lester.

This work was supported by the U.S. Office of Naval Research under award number N00014-15-1-2269.

ABSTRACT

The objectives of this study were to provide time-resolved (1) characterizations of shock wave/transitional boundary layer interactions using schlieren flow visualization, and (2) correlations of unsteady shock motion to boundary layer features. The characteristics of cylinder-induced shock wave/transitional boundary layer interactions in a Mach 2 freestream flowfield were studied experimentally. The Reynolds number in the Mach 2 facility was 30×10^6 m^{-1}. Incoming boundary layers were in transitional and fully turbulent states. Characterizing the shock wave motion was based on tracking the position of the shock wave on the model surface in schlieren images. The motion of the shock waves revealed an high-intensity resonance. When analysis of high-speed schlieren images were combined with unsteady pressure-sensitive paint studies, it was concluded that upstream scaling exhibited characteristics of laminar flow interactions, whereas the downstream separation mirrored turbulent interactions. This high-intensity resonance was duplicated using a blunt fin shock generator and an axisymmetric model. Furthermore, the unsteady dynamics of a boundary layer separation precursor upstream of the separation shock was highly correlated to the motion of the upstream influence (*UI*) shock and separation shock. The motion of the *UI* shock, separation shock and boundary layer separation precursor suggest that the unsteadiness in transitional interactions was driven by instabilities in the boundary layer. An initial characterization with changing Reynolds number and edge Mach number was made in the appendix.

TABLE OF CONTENTS

LIST OF FIGURES

NOMENCLATURE

Symbols

a	=	Local speed of sound
C_f	=	Local skin friction coefficient
C_H	=	Stanton number
D	=	Drag force
d	=	Shock generator diameter
df	=	Frequency resolution
f	=	Frequency
f_c	=	Zero-crossing frequency
$f(\eta)$	=	Normalized stream function of the Blasius laminar boundary layer
f_{max}	=	Frequency peak value
G_{xx}	=	Auto-spectral density function
h	=	Shock generator height
h_{tp}	=	Interaction triple point height: distance from model surface to where separation and closure shock intersect
L	=	Model length
L_i	=	Separation shock intermittency region
L_λ	=	Distance between separation shock and closure shock
M	=	Mach number
M_{edge}	=	Mach number at the edge of the boundary layer
P	=	Pressure
P_∞	=	Freestream pressure
Re_L	=	Freestream Reynolds number based on model length
Re_θ	=	Momentum thickness Reynolds number
Re_x	=	Unit Reynolds number
Re_{Xsep}	=	Boundary layer separation Reynolds number
St	=	Strouhal number
U	=	Freestream velocity
U_e	=	Boundary layer edge velocity

u	=	Velocity component in the x-direction
V	=	Velocity
v	=	Velocity component in the y-direction
x	=	Flow direction
y	=	Wall-normal direction

Greek Symbols

α	=	Angle of attack
α_3	=	Skewness
α_4	=	Kurtosis
δ_{99}	=	Boundary layer thickness
δ^*	=	Boundary layer displacement thickness
$\gamma_{\lambda 1}$	=	Separation shock intermittency
γ_{UI}	=	Upstream influence shock intermittency
λ_1	=	Separation shock
λ_2	=	Closure shock
η_f	=	Total skin friction drag coefficient
ρ_{xx}	=	Correlation function
σ	=	Standard deviation
σ^2	=	Variance
θ	=	Boundary layer momentum thickness
τ_w	=	Wall shear stress

Superscripts & Subscripts

∞	=	Freestream
0	=	Stagnation or total

Abbreviations & Acronyms

AFT	=	Amplification Factor Transport transition model
BL	=	Boundary Layer
CFD	=	Computational Fluid Dynamics

DNS	=	Direct Numerical Simulation
DSMC	=	Direction Simulation Monte Carlo
MPI	=	Message Passing Interface
NACA	=	National Advisory Committee for Aeronautics
NaN	=	Not a Number
NASA	=	National Aeronautics and Space Administration
PDF	=	Probability Density Function
PIV	=	Particle Image Velocimetry
PLS	=	Planar Laser Scattering
POD	=	Proper Orthogonal Decomposition
RANS	=	Reynolds-Averaged Navier-Stokes
SA	=	Spalart-Allmaras turbulence model
SBLI	=	Shock Wave/Boundary Layer Interactions
STBLI	=	Shock Wave/Turbulent Boundary Layer Interactions
TALon	=	Tennessee Aerothermodynamics Laboratory
UI	=	Upstream Influence
uPSP	=	Unsteady Pressure-Sensitive Paint
UTSI	=	University of Tennessee Space Institute
XSWBLI	=	Shock Wave/Transitional Boundary Layer Interactions

Chapter One

INTRODUCTION & LITERATURE REVIEW

Shock wave/boundary layer interactions (SBLI) are a significant source of technical risk and uncertainty in the design and operation of practically all high-speed vehicles [1]. The occurrence of such interactions can lead to extreme local thermal loads, local acoustic loads, structural fatigue, inlet unstart, and ultimately, vehicle failure [2]. Although interactions in laminar and fully turbulent boundary layers have been widely studied [1],[3]-[10], investigations involving a shock wave and a boundary layer transitioning from laminar to turbulent states have been mostly neglected due to their complexity and sensitivity [11]-[16]. Design trends have shifted towards decreasing the size of hypersonic vehicles and increasing the laminar boundary layer regime on external flow surfaces, in order to increase vehicle efficiency by reducing viscous drag [17]. Achieving these design optimization objectives requires an improved understanding of the fundamental characteristics associate with shock wave/transitional boundary layer interactions (XSWBLI).

The impact that shock wave/boundary layer interactions have on supersonic vehicles became apparent with the rapid technological development during the post-World War II era in the United States. During this time, there was a dramatic push for the development of high-speed flight vehicles and increased flight vehicle performance. Starting in the 1940s, the National Advisory Committee for Aeronautics (NACA, which became the National Aeronautics and Space Administration, NASA, in 1958) partnered with the military for the X-plane program to develop and test increasingly complicated aircraft to push the limits of human flight. The first time that humans piloted a craft that flew supersonic was in 1947 with the X-1 vehicle. In 1953, the D-558-2 Skyrocket surpassed Mach 2, and in 1956, the X-2 flew above Mach 3 [18]. The X-15 experimental

vehicle first flew in 1959 and was a pioneering technological development for high-speed flight. Its world record for the highest speed recorded by a piloted, powered aircraft was set by the X-15A-2 in 1967 at Mach 6.7 at 102,100 feet; this record has yet to be broken [19]. A photograph of this craft in flight is provided in Figure 1.1 with a dummy ramjet (circled) on the lower surface near the ventral fin.

Figure 1.1. Photograph of the X-15A-2 with the dummy ramjet (circled) attached. Image courtesy of NASA, 1967.

It was during this record-breaking flight that the real concerns of shock wave/boundary layer interactions were revealed. As the X-15A-2 decelerated from its maximum burnout, a heating warning in the engine bay alerted the pilot to execute an emergency landing. An SBLI that impinged on the vehicle ahead of the ventral fin had destroyed the protective ablator material in that region and penetrated the airframe structure. This shock impingement resulted in higher than expected heating loads on the external surfaces [18]. Images of the damage on the ventral fin as a result of the SBLI are shown in Figure 1.2. In addition to this damage, a shock wave from the dummy ramjet interacted with the shock wave from the ventral fin, creating a shock-shock interaction

near the intersection of the ramjet with the main airframe. The combination of the aforementioned SBLI and this shock-shock interaction weakened the structural attachment to such an extent that the dummy ramjet detached from the vehicle.

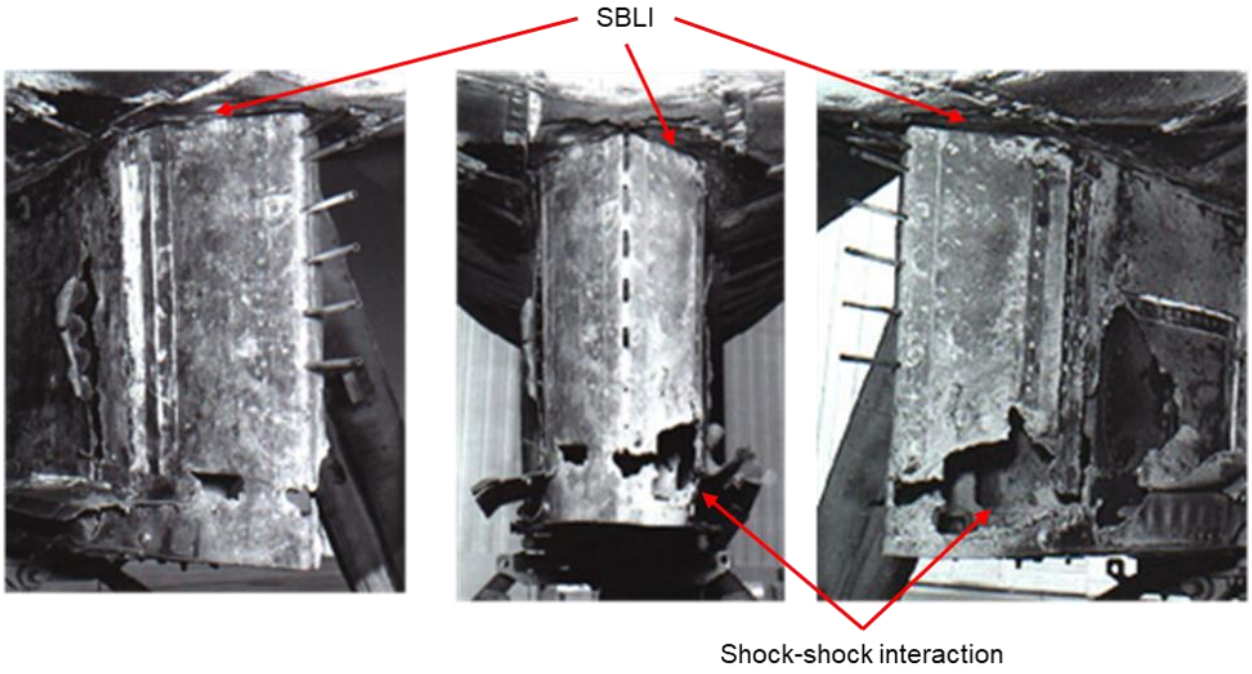

Figure 1.2. Images of the damage to the ventral fin on the underside of the X-15A-2 vehicle [18].

It was evident from this test flight that more research into the unsteady nature of SBLI was needed if high-speed flight was to continue. Although ground tests in wind tunnels of the X-15A-2 were conducted and the entire structure was covered in an ablative material to protect it from the thermal loads such high speeds induce, the impact and scale of localized thermal and acoustic loading was not well understood; this continues to be a subject of foundational research.

1.1 Motivation

Although transitional boundary layer interactions have been explored in the past, the primary focus of these studies was on the mean structure of the flow, and not the dynamic behavior of the interaction region. Furthermore, the majority of investigations of the interaction dynamics focused on pressure distributions based on discrete sensors along the model surface and other more intrusive diagnostics. As increasing high-speed vehicle efficiency becomes necessary for the practical application of hypersonic technology, it is crucial to understand the aerodynamic impact of shock wave/transitional boundary layer interactions. Characteristics previously observed in laminar interactions (streamwise-separation scales) and turbulent interactions (heat transfer rates) are observed in conjunction with one another in transitional interactions. There is also the potential for increased loading compared to turbulent interactions [20]. SBLI in general scale to the incoming boundary layer thickness, but they are sensitive to the Reynolds number as well as boundary layer state. These competing effects and the array of contributing components help motivate the current investigation into transitional interactions.

1.2 Literature Review

This section summarizes the history of prior experimental and computational efforts to characterize shock wave/boundary layer interactions (SBLI), including the unique characteristics of laminar, transitional, and turbulent boundary layers and the challenges that they present to studying shock wave interactions within boundary layers of each state. This section also includes an overview of the more recent research efforts that have informed this work.

1.2.1 Classification of Interaction Structures

There are many different types of SBLI that exist on flight vehicles with various shock generators, incoming boundary layer states, boundary layer scales, Reynolds numbers, and Mach numbers. Gaitonde [3] provides an overview of many of the interaction configurations previously studied in the literature. Examples of these shock generator configurations are shown in Figure 1.3. Perhaps the most studied are the nominally two-dimensional interactions generated by impinging shocks and compression ramps as illustrated in (a) and (b) of Figure 1.3. The difficulty in interpreting results from these configurations in ground test facilities are the imposed three-dimensional effects from the test section sidewalls, corner flows, and model edge effects that occur on the spanwise limits of the experiment.

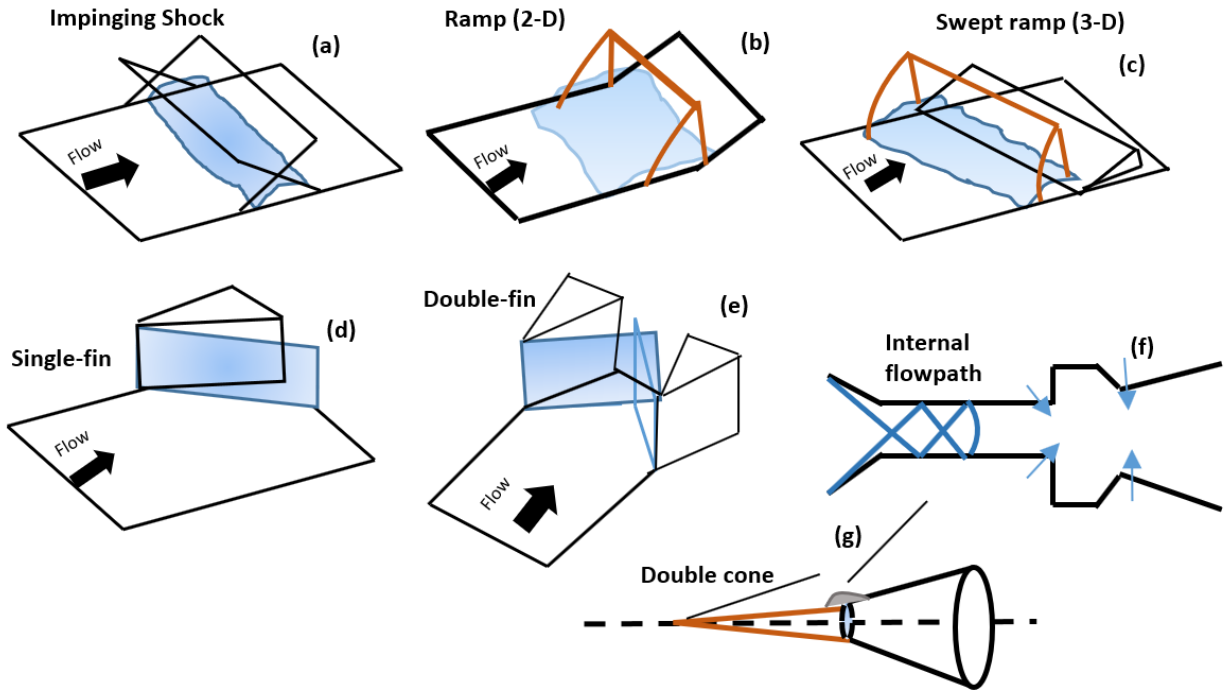

Figure 1.3. Shock generator configurations traditionally employed for fundamental studies of SBLI. Image adapted from Gaitonde [3].

Three-dimensional interactions include those generated by swept ramps (c) and sharp fins (d). In swept ramp configurations, there is a strong cross-flow component that disrupts the closed-loop recirculation effects observed in two-dimensional interactions. The sharp fin also generates a swept interaction and heavily mirrors the interaction structure of the swept ramp in that they both have the same basic structure. Double-fin configurations (e) typically are used for more complex interactions associated with canonical air-breathing inlet structures. Along those lines, internal flowpaths of air-breathing vehicles can be simulated using ducts to evaluate a shock train, as shown in (f). Some axisymmetric shock generators are cylinder flares or double cones, as illustrated in (g), that are not influenced by the spanwise boundary limits observed in two-dimensional interactions.

All of the configurations presented in Figure 1.3 are examples of shock generators used in ground test facilities. As previously mentioned, there are many other factors that impact the characteristics of SBLI other than the geometric shock generator. For example, shock waves may also result from flow distortion, such as boundary layer separation. Other variables that impact the flow physics include the state of the incoming boundary layer and its characteristic features, including Reynolds number and Mach number. Descriptions of these incoming flowfield variables and how they affect the shock wave dynamics of SBLI will be considered in the subsequent sections.

1.2.2 General Interaction Structure

The SBLI studied here is representative of one occurring on external flow surfaces where the fuselage of a hypersonic or supersonic body intersects with a control surface (wing, stabilizer, *etc*.) or a discontinuity results in a shock wave impinging on a boundary layer further downstream [1]. The primary focus of this work is on a vertical cylinder shock generator on a flat plate model; although blunt fin shock generators are also briefly examined. This configuration generates an interaction that is nominally two-dimensional (spanwise symmetric) on the symmetry plane. This avoids the effects of sidewall contamination with the interaction region and allows for shock generation at any location

along the boundary layer evolution. Furthermore, the strength and scale of the interactions are easily controlled by varying the cylinder height and diameter [21].

The shock wave structure for this interaction is illustrated in Figure 1.4. As with other interactions with separation, the inviscid shock bifurcates into a separation shock, λ_1, and a downstream closure shock, λ_2. The size of the separation region resulting from this interaction is scaled by the cylinder diameter, d, and the incoming boundary layer thickness, δ_{99} [22]. The different regions of unsteadiness considered in this work are the motion of the shock waves, and the location of boundary layer separation. Boundary layer separation is a result of the adverse pressure gradient generated by a change in pressure on the model surface; the boundary layer is considered separated from the surface when the flow begins to travel in the opposite direction of the freestream or the skin friction goes to zero [23]. The intermittent region, L_i, is the region of unsteady oscillation of the separation shock. The upstream influence (*UI*) shock as defined by Dolling *et al.* [24] appears intermittently and is also unsteady. The *UI* shock also represents the farthest upstream point where the influence of the boundary layer separation is observed and emanates from the separation shock foot, moving upstream. This feature is an important indicator of transitional interactions, as will be discussed in subsequent chapters.

One of the other scaling parameters used to describe this lambda-shock interaction is the triple point height, h_{tp}, where the inviscid shock bifurcates into the separation and closure shocks. The flow along the centerline between the inviscid bow shock and the cylinder face is subsonic, but the flow just below the triple point remains supersonic [25]. This results in a supersonic jet from an Edney interaction [26] that emanates from the triple point and impinges on the cylinder face. Away from the centerline in the outboard region (spanwise area), the boundary layer separation is swept downstream in counter-rotating horseshoe vortices [27],[28].

The inherently unsteady motion of this shock structure as a result of the separation takes on a “breathing” motion with an inflationary stage and a collapsing stage. In the inflationary stage, flow between the inviscid shock and the cylinder face is entrained in the separated region of the boundary layer, pushing the separation shock upstream. When the separation shock moves farther away from the cylinder face, the inviscid shock

weakens and less fluid is pushed into the separation region. This leads to the collapsing stage, where the separation shock moves downstream again, which strengthens the inviscid shock, and begins another inflationary stage [25].

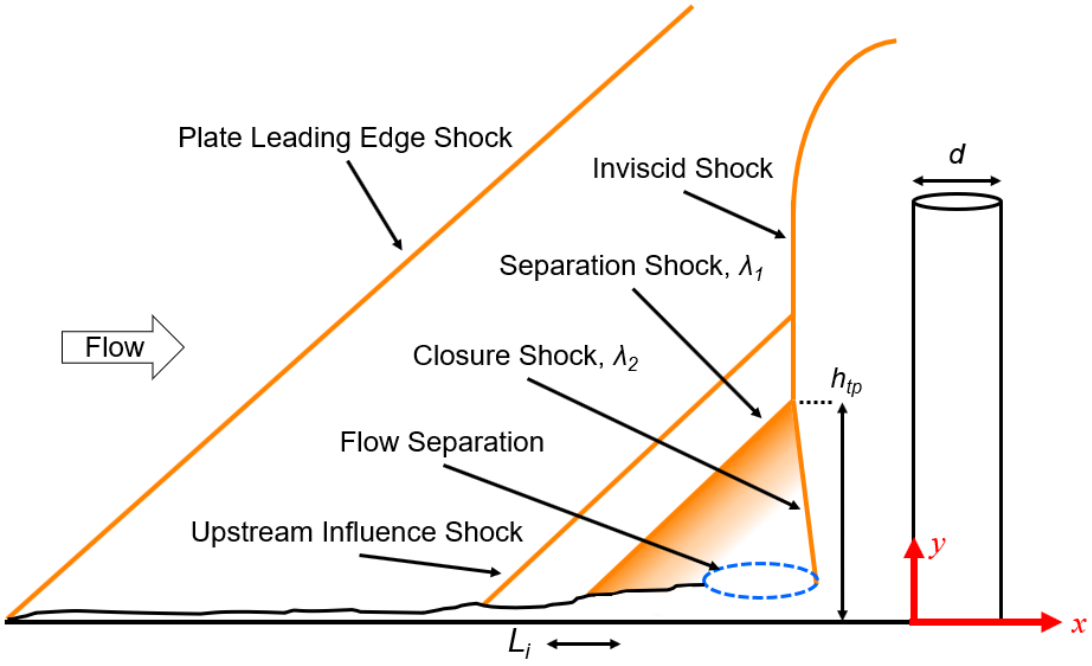

Figure 1.4. Schematic of the vertical cylinder-generated SBLI with corresponding variable definitions.

When using shock generators of this type (vertical cylinders or blunt fins), the height of the shock generator should be semi-infinite with respect to the interaction region in order to maintain a normal bow shock so that the cylinder height is not a factor of the interaction scaling. Previous investigations established that although a specific value of the ratio of cylinder height, h, to diameter, d, cannot be given since h_{tp} is a function of the Mach number and the Reynolds number, a general guideline of $h/d > 2.4$ is in most cases sufficient [22]. For all data presented in this work, the frame of reference origin is at the base of the shock generator with positive x in the streamwise direction parallel to the model surface and positive y normal to the model surface.

1.2.3 Interactions in Laminar Boundary Layers

There are three regime classifications for the viscous layer near a surface with a moving fluid that defines the boundary layer: laminar, transitional, and turbulent. Each has its own unique characteristics, which are important to understand as the incoming boundary layer state greatly impacts the scaling and dynamics of SBLIs. Laminar boundary layers are characterized by relatively smooth, continuously varying properties in the wall-normal direction that are frequently visualized as layers moving over top each other that are inefficient at transporting freestream momentum to the surface. This makes them more prone to separating from the surface. This means that the extent of upstream boundary layer separation (and separation shock location) for a laminar interaction is larger than the other regimes, and the separation scaling decreases with an evolving transitional boundary layer until a fully turbulent incoming boundary layer is achieved [14].

A laminar boundary layer can be described for a flat plate model that is parallel to a two-dimensional flow with a constant freestream velocity, U, using the Blasius equation [29]. This is a third order, non-linear ordinary differential equation with no-slip boundary conditions. This can be applied to solve for laminar boundary layer characteristics such as displacement thickness, δ^*, momentum thickness, θ, wall shear stress, τ_w, and the viscous drag force, D [23]. When a rapid increase in the static pressure along the model occurs in the streamwise direction, the boundary layer separates from the model surface. Using Bernoulli's equation (even though it's being applied to a viscous flow) to compare velocities at the end of the boundary layer and at a point within it, it can be shown that a given pressure gradient will produce a larger change in velocity at the location within the boundary layer [30]. This leads to a reversal of the flow near the model surface that presents an obstacle for the upstream flow and the boundary layer separates. In addition to the reversal of the flow direction at the separation point, the skin friction becomes zero [30].

One of the first studies to evaluate laminar interactions was by Young *et al.* [28] who considered SBLI generated by blunt fins for a variety of freestream Mach numbers and Reynolds numbers using oil flow visualization and pressure transducers. Some of the critical observations made were the greater dependence on Reynolds number that

laminar interactions had compared to turbulent interactions; as the Reynolds number increased, the location of boundary layer separation moved farther upstream from the blunt fin leading edge until transition occurred, which then decreased the scale of the separated region. The area of influence in the outboard region was also larger for laminar than turbulent interactions [28]. This effect was also observed by Dolling and Brusniak [31] for two different boundary layer thicknesses in turbulent interactions. By increasing the Reynolds number, the incoming boundary layer thickness decreases. They observed a change in the frequency of oscillation of the separation shock motion for blunt fin shock generators as a result of this thinner boundary layer, which was independent of the model scaling of the shock generator divided by the incoming boundary layer thickness, d/δ_{99} [32].

The shape of wall-pressure distributions along the centerline for shock wave/laminar boundary layer interactions take the same general shape: an initial and gradual rise in pressure to an eventual plateau. The normalized pressure for this relatively high-pressure plateau may be found from the following expression based upon correlations by Hill [33] and is independent of the shock generator geometry.

$$\frac{P}{P_\infty} = 1 + 1.218{M_\infty}^2\left[\left({M_\infty}^2 - 1\right) Re_{Xsep}\right]^{-1/4} \tag{1.1}$$

Laminar boundary layer interactions are generally considered resolvable by modern computational methods [34]. A significant effort by the Air Force Office of Scientific Research (AFOSR) was made to collect experimental data to validate the computational Navier-Stokes and direct simulation Monte Carlo (DSMC) code predictions for low-enthalpy, laminar interactions generated by a hollow cylinder flare and double cone [34]. The largest source of uncertainty within this study was the effect of nonequilibrium thermo-chemistry [34]. Despite this, efforts continue to improve these models in order to characterize more complicated configurations at higher Mach numbers that are difficult to conduct using traditional ground test methods, but represent more realistic operational conditions. Two recent examples are for hollow cylinder flare [35] and

blunt fin [36] shock generators. For the hollow cylinder flare case, Navier-Stokes and ideal gas equations were used to model existing experimental data for a Mach 10 freestream by comparing the effect of grid size in the computations on the comparable surface pressure and heat transfer rates, to good agreement [35]. A similar computation by Mortazavi and Knight [36] was performed using a solution to the unsteady Navier-Stokes and ideal gas equations for a blunt fin that is swept away from the boundary layer surface for a Mach 14 freestream flow. For that effort, the numerical code was able to resolve the localized high pressure and heat transfer rates, as well as the unsteady motion of the shock wave oscillations [36].

Finally, Lee and Gross [37] were able to use direct numerical simulations (DNS) to evaluate the effect of a swept impinging shock on a laminar boundary layer at two different Mach numbers. The objective was to characterize the effect this swept impingement would have on the flow similarity and validate the existence of a steady global mode observed in the interaction region from prior computations [37].

1.2.4 Interactions in Turbulent Boundary Layers

Turbulent boundary layers are classified by the eddies that disrupt the layers of fluid that classify laminar boundary layers. For decades, turbulent boundary layer interactions have been the primary focus for SBLI research for two main reasons: first, turbulent boundary layers have historically been considered to be more likely for large flight vehicles; second, the inherent unsteadiness of these interactions have more severe effects on the model surfaces through comparatively increased pressure loads and heat transfer rates. One way this can be illustrated is by evaluating the total skin friction drag coefficients for both laminar and turbulent flows. Blasius [29] developed expressions to describe laminar boundary layers through normalizing by dimensionless quantities. His solution relates the total skin friction drag coefficient, η_f, to the freestream Reynolds number based on the total length of the model, Re_L. Due to the complexity of the flow, a turbulent equivalent could not be determined theoretically, but rather is based upon empirical data to form an approximation. These relations revealed that the frictional shear stresses are greater for a turbulent boundary layer than in a laminar boundary layer.

A close approximation in relating the heat transfer for boundary layers based upon skin friction (or *vice versa*) is through the Reynolds analogy. A good summary of the different forms of the Reynolds analogy for compressible turbulent boundary layers is provided in Ref. [38]. The most general relation originally described by Reynolds related the Stanton number, C_H, and the local skin friction coefficient, C_f. The Stanton number relates the heat transfer coefficient to the fluid density, velocity, and specific heat. Chi and Spalding [39] later refined the Reynolds analogy. As previously discussed, the skin friction coefficients for turbulent boundary layers will be greater than for laminar boundary layers. This means that the Stanton number will also be higher and the rate of heat transfer to the surface will thus also be greater for turbulent boundary layers than for laminar boundary layers.

One of the primary sources of uncertainty in turbulent interactions is the source of the inherent unsteadiness in the flow. More so than with laminar interactions, correlating the unsteady turbulent fluctuations in both the incoming boundary layer and within boundary layer separation has been the primary focus when attempting to address this uncertainty [40]. Turbulent boundary layers by nature are unsteady with many different scales of eddies and motion. An example of this unsteadiness is provided in Figure 1.5 for a vertical cylinder generated interaction with a fully turbulent boundary layer in a Mach 2 freestream flow. Three pressure transducers were located in the boundary layer freestream upstream of the interaction region, under the mean location of the separation shock, λ_1, and in the boundary layer separation region prior to reattachment. The sensors associated with the separation shock and in the boundary layer separation region have been offset for clarity. The relative levels of unsteadiness between the three sensors is clear, with the freestream turbulent pressure fluctuating less than 1 kPa, the pressure under the separation shock fluctuating by approximately 5 kPa, and under the separated boundary layer by about 25 kPa.

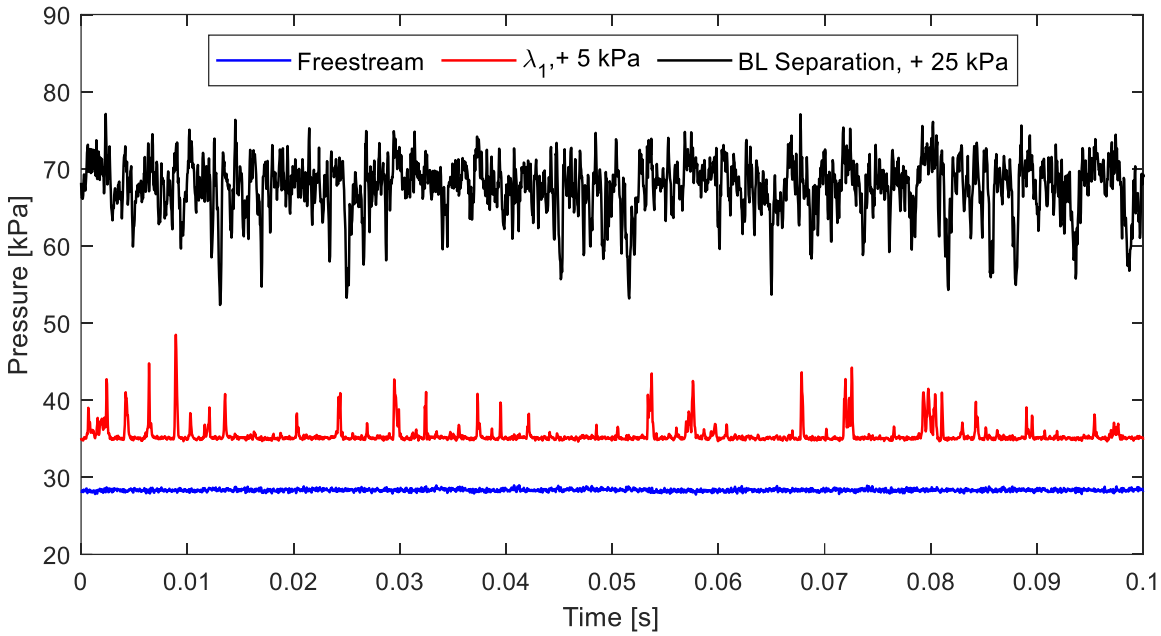

Figure 1.5. Time histories of three pressure transducers for a fully turbulent shock wave/boundary layer interaction generated by a vertical cylinder in a Mach 2 freestream.

In addition to the time histories, the normalized power spectral density functions provide a good indicator of which frequencies are contributing to the unsteady pressure measurements. The spectra for the same three transducers shown in Figure 1.5 are provided in Figure 1.6 where the autospectral density function has been normalized by the frequency and the variance of the signal. The freestream boundary layer fluctuations are at a much higher frequency than the separation shock and boundary layer separation pressure signals, indicating that the presence of boundary layer separation acts as a low-pass filter of the freestream turbulence levels.

Because turbulence is so effective at mixing within the boundary layer, drag, heat transfer, and mass transfer are increased compared to laminar interactions [41]. This is visualized by Figure 1.7 for a laminar (a) and turbulent (b) boundary layer profile with the *y*-axis the wall-normal scaling of y/δ and the *x*-axis the Mach number [42].

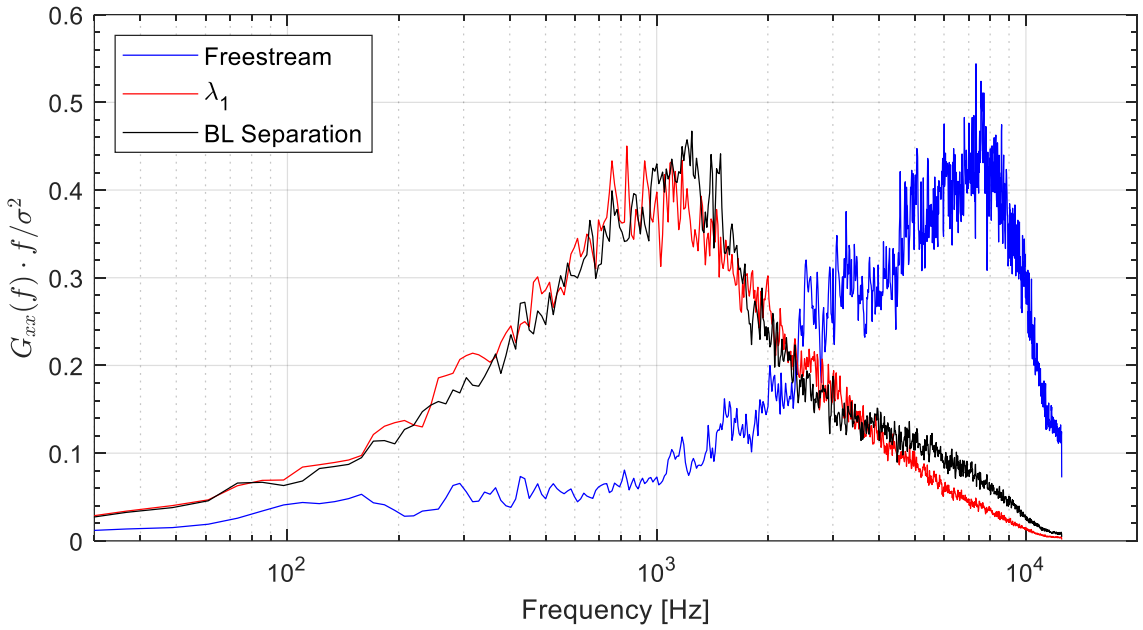

Figure 1.6. Normalized power spectral density functions for three pressure transducers in a fully turbulent boundary layer interaction.

As can be observed from the two boundary layer profiles, the sonic line is much closer to the model surface for the turbulent state than the laminar state, revealing that more of the freestream momentum gets transferred to the surface and more momentum exists closer to the surface than for the laminar interaction.

Young *et al.* [28] also looked at incoming turbulent boundary layer interactions in their work, keeping the focus on the differences in interaction scaling and pressure loads in comparison to laminar interactions. Because turbulent boundary layers are less susceptible to separation than laminar boundary layers, the separation scale decreases and once a fully turbulent incoming boundary layer state is achieved, further changes to the interaction scaling are not expected. In fact, Westkaemper [43] showed that the upstream separation distance for cylinder-induced turbulent interactions remained constant at 2.65*d* for a wide range of Mach numbers and Reynolds numbers.

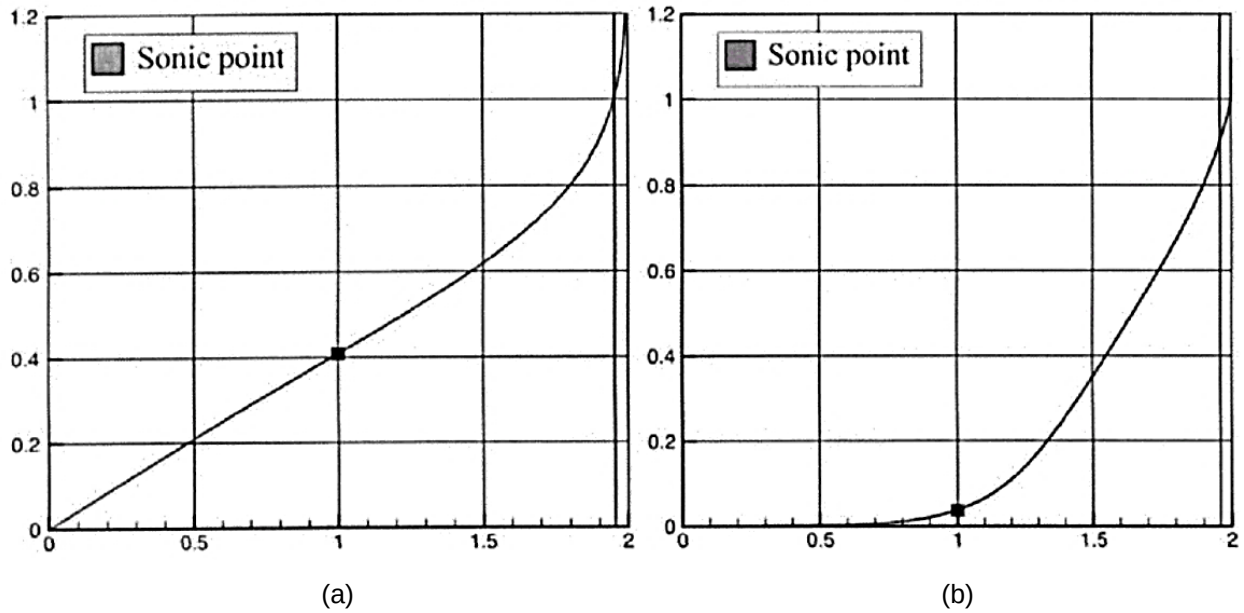

(a) (b)

Figure 1.7. Boundary layer profile comparison for (a) laminar boundary layer and (b) turbulent boundary layer for a Mach 2 freestream flow over a flat plate with sonic point labeled. *Y*-axis scaling is y/δ, *x*-axis is Mach number [42].

Early mathematical models showed that the dominant cause of the separation shock wave oscillations was a result of the incoming turbulent boundary fluctuations [44]. Dolling and Brusniak [31] later came to a different conclusion after evaluating the normalized pressure distributions in the incoming boundary layer and under the separation shock foot for a variety of shock generators. They attempted to determine if there was a correlation between the frequency of oscillation of the shock wave and the bursting frequency of turbulent eddies in the boundary layer and concluded this not to be the case since the large eddy frequencies in the boundary layer varied from 30-40 kHz, yet the shock wave motion was from 200 Hz – 2 kHz [31]. They proposed that it was the fluctuations of the separated flow behind the shock that drives the shock motion [31]. Early blunt fin shock generator work by Gonsalez and Dolling [45] evaluated the intermittent region (the distance between the upstream influence line and separation shock locations) length scales and the zero-crossing frequency, f_c, of the separation shock for varying angles of blunt fin sweep; they showed that f_c is very sensitive to the intermittent region scale through the Strouhal number. They attribute this correlation to

the essentially constant mean shock speed when it oscillates upstream and downstream around the mean position [45].

More recent work used advanced diagnostics to determine the source of unsteadiness of the separation shock, or at least to better understand different contributions to the unsteadiness. Beresh *et al.* in 2002 [46] used high-speed particle image velocimetry (PIV) to demonstrate a correlation between the incoming turbulent boundary layer and the separation shock motion. Specifically, upstream boundary layer accelerations in the lower third of the incoming boundary layer were highly correlated to the motion of the separation shock wave at frequencies of 4-10 kHz [46], which is significantly lower than the aforementioned large eddy frequencies of 30-40 kHz. One limitation of this study was the ability to resolve shock unsteadiness frequencies only up to 4 kHz [46].

A computational model primarily based on PIV data was able to correlate the low-frequency entrainment downstream of the separation shock to the unsteady motion of the separation bubble [47]. Piponniau *et al.* [47] observed only small variations in the upstream turbulent boundary layer conditions that did not correlate to the large-amplitude motion of the separation bubble. This is seemingly in contradiction to the idea that the separation shock unsteadiness is a result of upstream boundary layer characteristics. However, these upstream characteristics considered by Piponniau *et al.* [47] were only of the incoming superstructures, not the near wall regions as described by Beresh *et al*. [46]; furthermore, Piponniau *et al.* [47] make note that the low-frequency correlation model only applies in compressible flows where a separated and reattached boundary layer downstream of the shock wave exists. Boundary layer separation for turbulent interactions is not always present.

Clemens and Narayanaswamy [40] provide an overview of existing data up to 2014 that focus on the source of this low-frequency unsteadiness in the interaction system. Although they acknowledge that upstream boundary layer fluctuations are an important source of unsteadiness, the impact of this source is highly dependent on characteristics of the downstream separation [40]. For example, correlations between the separation shock motion and pressure fluctuations in the separation region led to the conclusion that

the separated flow drives the interaction unsteadiness, especially since the pressure fluctuations preceded the shock motion [40]. However, as Brusniak and Dolling [48] observed, upstream structures could influence the separated flow, thus displacing the separation shock wave. Clemens and Narayanaswamy [40] further add that the nature of the upstream boundary layer fluctuations is not as important as the frequency and amplitude of the fluctuations. Finally, they conclude that the separation shock acts as a low-order dynamical system influenced by both the upstream boundary layer and the downstream fluctuations [40].

A similar argument was made by Poggie *et al.* [49] who was able to apply a theory developed by Plotkin [44] that demonstrated that the broadband perturbations in the incoming boundary layer lead to the low-frequency motion of the separation shock. Poggie *et al.* [49] showed that the separation shock unsteadiness behaves as an amplifier of large-scale disturbances (10-1,000 Hz) in the incoming boundary layer when comparing computational models to experimental data collected both in ground test facilities and flight test missions. It is evident that there are competing or complimentary sources of separation shock unsteadiness for turbulent interactions, especially for approximately two-dimensional interactions with closed recirculation regions. Where the unsteady source originates from, and to what level of contribution each source makes, is still an ongoing source of research with new and better diagnostics and analysis regularly revealing new information [50].

1.2.5 Transitional Boundary Layers

The ability to describe and predict boundary layer transition from laminar to turbulent states is of continuing interest. There are several parameters that influence the transition process such as: Reynolds number, Mach number, pressure, temperature, surface roughness, leading-edge effects, and freestream turbulent levels [51]. It is important to emphasize that transition is a process that occurs over a region, as opposed to a singular event at a finite location. Schetz [30] describes the general process as two-dimensional disturbances that grow and break into three-dimensional disturbances that then break down into localized spots of turbulence that then merge together to form a

turbulent boundary layer. The two-dimensional disturbances in the laminar boundary layer are known as Tollmien-Schlichting (T-S) waves. Turbulence may also originate from a source that leads to unstable vortices, such as from the wake of a surface roughness element [52]. A waterfall chart that describes the process of instability growth and breakdown to turbulence is provided in Figure 1.8. When performing boundary layer transition experiments in ground test facilities, the freestream turbulence levels must be considered. The turbulence from test section sidewalls, for example, can influence the boundary layer of the test model to induce transition faster than the model would experience in a quiet facility or during a flight test [53]. In particular, larger freestream disturbances could lead to bypass transition, as illustrated in Figure 1.8 via “bypass mechanisms”.

Linear stability theory can accurately describe the evolution of very small disturbances in laminar boundary layers, but is not adequate for the large fluctuating levels in turbulent flows [52]; however, this theory could be used to estimate the onset of transition. Anderson [55] outlines how self-similar solutions may be used to describe hypersonic boundary layers, where other three-dimensional instabilities impact the transition process, such as crossflow components or Görtler vortices [56],[57].

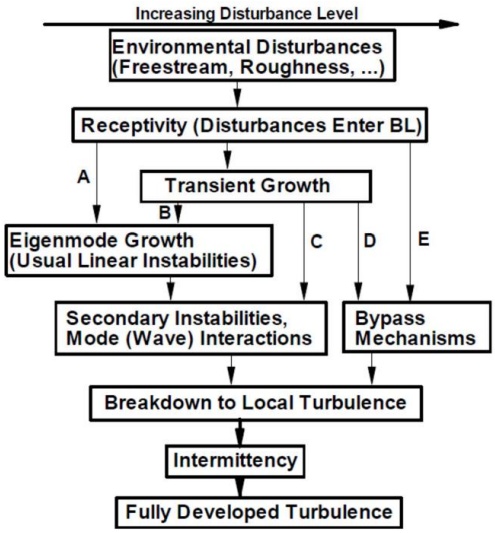

Figure 1.8. Waterfall plot describing the mechanisms that lead to boundary layer transition. Image adapted from [54], courtesy of J.D. Schmisseur.

These various contributors to boundary layer transition make transition not only difficult to predict, but highly dependent on the specifics of the flowfield; this includes for identical freestream flow conditions, but around different wind tunnel model geometries. However, the advancement of computational efforts has allowed for transition contributors to be isolated from ground test facility effects, particularly through DNS and improved transition models. Recently, von Deyn *et al*. [58] were able to simulate the bypass transition process with artificially generated freestream turbulence and distributed surface roughness. They successfully compared the process with an undisturbed laminar boundary layer transitioning naturally. Specifically, von Deyn *et al.* [58] observed the bypass transition as a result of larger roughness elements inducing secondary streak instabilities; this differs from bypass transition induced solely by freestream turbulence in that no localized growing turbulent spots were observed. Computational methods are also being used to predict transition onset. Zhou *et al.* [59] applied an improved k-ω-γ transition model to the X-51A flight vehicle for both its external surface and for the scramjet engine, and they were able to match the experimentally acquired transition data.

The momentum thickness Reynolds number, Re_θ, can be useful for predicting boundary layer transition with a stability limit (linear disturbances, inviscid limits [60]) based on the freestream turbulence intensity as defined by van Driest and Blumer [61]. This was explored experimentally by Wang *et al.* [62] who evaluated the impact of increased freestream turbulence levels on the boundary layer transition over a flat plate and compared the results to other models for accuracy. They defined an unstable laminar flow as different from laminar or transitional flow, and looked specifically at early turbulent flow just downstream of transition in comparison to fully turbulent flow. One interesting result was that the streamwise turbulence intensity near the wall was larger for transition than the maximum value observed in turbulent normal shear stress profiles [62]. Furthermore, long-period unsteadiness was observed in the low freestream disturbance laminar flow cases downstream of the theoretical instability limit that was not observed before transition in the high disturbance flows.

Predicting and characterizing boundary layer transition for practical applications is critical to the design of high-speed vehicles, but are highly sensitive to a variety of flow

parameters. Since transitional boundary layers and turbulent boundary layers have peak rates of heat transfer greater than laminar boundary layers [63], knowing where transition begins and ends can help inform where to place thermal protection systems, which could change the weight distribution of the vehicle. Or, if a certain boundary layer state is desirable at a certain location on the vehicle, then tripping elements to induce transition may need to be used, and precise placement of those elements is necessary. Since transitional boundary layers are a continued source of study, there are many possible contributing factors to the resulting unsteady shock motion for an XSWBLI.

1.2.6 State of the Art

In this section, an overview of the history of transitional interactions specifically is presented, as well as prior work that more directly relates to this dissertation.

One of the earliest studies of transitional interactions by Chapman *et al.* [64] in 1958 reported that such interactions were highly unsteady compared to the relatively steady behavior of laminar and turbulent interactions. The unsteady surface pressure measurements were found to depend on the location of the boundary layer transition relative to the boundary layer separation and reattachment positions. Transitional boundary layer separations were characterized by an abrupt pressure increase at the transition location, more particularly when the transition location was immediately upstream of the reattachment [64]. Later, Kaufman *et al.* [65] evaluated blunt fin turbulent interactions in an attempt to have an accurate flow model to compare to analytical methods for predicting peak loads. In the course of their experiments, transitional interactions were also evaluated. In particular, they noted the strong dependence on the incoming boundary layer state to the increased level of unsteadiness for transitional, compared to turbulent, interactions, although the boundary layer separation scales with fin diameter [65]. What was unique about the Kaufman *et al.* [65] work was the focus not only on the model surface pressure distribution and schlieren imaging, but the increased pressure load from the Type IV Edney [26] shock impingement on the blunt fin face.

Transitional interactions generated by a compression corner were studied by Heffner *et al.* [20] who found that the heat transfer rates in transitional regions rapidly

reached those in turbulent boundary layers and that the extent of separated flow decreased with increasing Reynolds numbers. This observation implies that the boundary layer transition region in front of the compression corner decreased with increased Reynolds number; thus, as the boundary layer evolves to fully turbulent, the scale of the interaction decreased [20]. This behavior is counter to incoming laminar interactions, where increases in Reynolds number saw increases in separation distance as a result of the thinner boundary layer [28],[31]. Another characteristic explored by Korkegi [66] was the impact of transition on the boundary layer separation and shock positions; under certain conditions, they were not in the same location. Korkegi [66] observed a break and inflection in the boundary layer separation line with the onset of transition with the inflection point upstream of the bow shock shape for a blunt fin generated interaction. Korkegi [66] attributed this to the distortion of the bow shock near the plate surface as a consequence of the upstream separated flow region.

More recent efforts to examine the dynamic behavior of transitional interactions took place at the University of Texas at Austin in the early 2000s [12]-[14]. Using a cylinder mounted normally to a flat plate, Dolling *et al.* [12] used kerosene-lampblack images to determine the separation location as a function of the cylinder position on the plate surface. The separation distance upstream of the cylinder decreased as the distance from the plate leading edge increased [12]. This same behavior was observed by Young *et al.* [28] in the 1960s who used blunt fin shock generators to compare laminar and turbulent interactions via pressure transducers and schlieren imaging.

Murphree *et al.* [13], [14] expanded upon the work of Dolling *et al.* [12] using a vertical cylinder on a flat plate model by employing schlieren imaging, planar laser scattering (PLS) visualization, kerosene-lampblack surface flow visualization, and PIV to characterize the interaction. While previous work in SBLI frequently used schlieren or intrusive diagnostic measurement techniques (*i.e.* hot wires), this work was one of the first attempts at non-intrusive planar flow diagnostics. Murphree *et al.* [14] confirmed that the boundary layer separation distance from the leading edge of the shock generator decreases as the incoming boundary layer transitions to fully turbulent. The PLS imaging results from Murphree *et al.* [14] were consistent with the kerosene-lampblack images,

and further revealed a series of turbulent spots in the interaction region upstream of the vertical cylinder. These observed turbulent spots were described as disturbances caused by boundary layer transition and appear to remain constant, which means that as individual spots propagate downstream, new spots appear where the old spots previously were. Murphree *et al*. [14] observed that as the spots propagate through the shock structures, the boundary separation scale increases, implying that the spots are pockets of relatively lower velocity that are less resistant to boundary layer separation. Murphree *et al.* [14] also visually observed similar interaction results when using both tripped and un-tripped boundary layers. The ability to use tripped or un-tripped boundary layers was corroborated by Benay *et al.* [67] when testing transitional SBLI on an axisymmetric cylinder-flare model for high Reynolds numbers using roughness elements by comparing normalized pressure distributions along the model surface for constant stagnation pressure and Reynolds number.

One interesting trend that Murphree *et al*. [13] noticed when comparing their results to those of Kaufman *et al.* [65] was in the normalized separation scales based on the state of the incoming boundary layer for varying Mach numbers and shock generator diameters. Particularly, Figure 1.9 shows the separation shock scaling (λ_{sep}/d) at 4.5d for incoming laminar interactions, before an incoming turbulent interaction scale asymptote at approximately 2d upstream of the shock generator. Between these values, the separation scaling decreases approximately linearly. The boundary layer scale on the x-axis was characterized by the location of separation, x_{sep}, and the location of the end of transition, x_{trans} (4.1 in), measured from the flat plate leading edge.

Recent work addressing boundary layer transition include Franko and Lele [63] while Sandham *et al.* [68] evaluated transitional interactions at hypersonic freestream conditions. Both studies focused on characterizing the flowfield using heat transfer coefficients, computations, and infrared thermography. They found that the heat transfer rate was higher in transitional, as opposed to fully turbulent, boundary layer regions. Giepman *et al.* [16] employed PIV to study transitional interactions from an oblique shock reflection, where the scale and strength of the induced boundary layer separation decreased as the boundary layer evolved to fully turbulent. In their results, the fully

turbulent boundary layer interaction showed no separation, where the transitional interaction did separate the boundary layer [16].

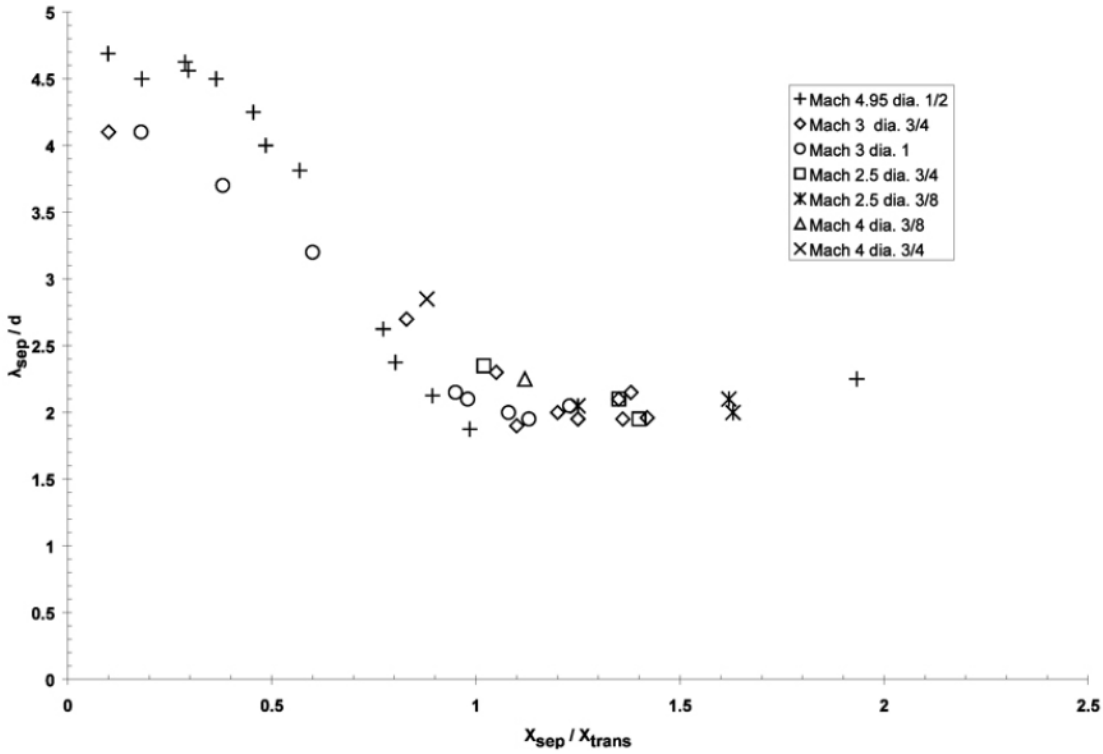

Figure 1.9. Normalized separation shock scaling for varying Mach number and shock generator diameters [13].

1.3 Scope of the Current Work

The main objective of the current study is to provide (1) time-resolved characterizations of shock wave/transitional boundary layer interactions, and (2) correlations of unsteady shock motion to the boundary layer state. The interactions discussed in this study are investigated using qualitative and quantitative optical diagnostics. The focus is on extracting quantitative information from traditional schlieren imaging. This ensures the non-intrusive nature of the data acquisition and offers a new

technique where quantified shock wave characteristics can be made without the added time and expense of model modifications to accommodate other diagnostic techniques. Furthermore, using schlieren as the basis for dynamic characterization can inform what additional diagnostic and where for any subsequent evaluations of this flowfield. Using this as the primary method of experimental data collection, the dynamics of shock wave behavior for transitional interactions are characterized as the incoming boundary layer evolves from an approximately steady, laminar state to an unsteady turbulent state. In addition, correlating the shock wave dynamics to boundary layer state will provide key insights into sources of unsteadiness. Furthermore, both vertical cylinder and blunt fin shock generators are compared to provide verification that any effects from the cylinder wake do not propagate upstream to impact the shock wave dynamics. This is consistent with previously discussed studies [12]-[14], [28], [31], [36], [43], [48], [65].

Shock wave dynamics are primarily characterized by tracking the shock position in a series of high-speed schlieren images that provide time-resolved statistical and spectral information though a MATLAB algorithm developed at UTSI. The effects of the incoming boundary layer states are varied by changing the position of the shock generator on the model surface. Models consist of both flat plates and an axisymmetric cone; however, the interaction is still assumed to be nominally two-dimensional in the centerline plane for all configurations presented in this study.

The results of this research will provide insight into the fundamental physics of how transitional interactions behave in high-speed inlets, external control surfaces, and body junctions that will advance the development of high-speed vehicles.

Chapter Two

TRANSITIONAL INTERACTIONS IN A MACH 2 FREESTREAM

The first set of experiments in this study were conducted in the Mach 2 blowdown wind tunnel facility at the University of Tennessee Space Institute (UTSI). This chapter will focus on comparing the unsteady shock dynamics for sample transitional and fully turbulent interactions for vertical cylinder and blunt fin shock generators on two model surfaces. A more in-depth analysis of this data is provided in the following chapter.

2.1 Mach 2 Experimental Setup

As previously mentioned, UTSI has a Mach 2 low-enthalpy blowdown wind tunnel in which these initial experiments were performed. The test section has a constant cross-section of 203 mm × 203 mm (8 in × 8 in). Air is supplied as the test gas from a 23.6 m^3 bottle farm compressed to a nominal pressure of 20 MPa. The stagnation pressure is maintained by a control valve at approximately 240 kPa ± 6. The storage tank pressure is sufficient to allow for continuous run times up to two minutes, although run times for this study were typically less than 30 seconds. The flow is not heated and the air is cooled by expansion through the mass control valve, resulting in stagnation temperatures of approximately 285 K ± 8. The freestream velocity is on average 500 m/s, resulting in a nominally freestream Mach number of 2 and a freestream Reynolds number of 30×10^6 m^{-1} ± 5%. Optical access for the experiments was provided by BK7 glass windows on the test section sidewalls and ceiling. Further details pertaining to this experimental facility are provided by Rice *et al*. [69] and Peltier *et al*. [70] A schematic of this facility is provided in Figure 2.1.

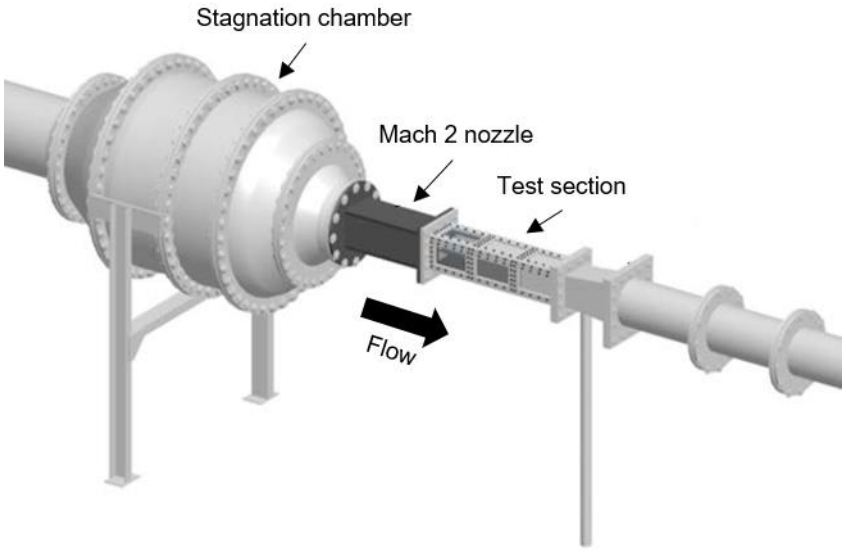

Figure 2.1. Schematic of the UTSI Mach 2 blowdown wind tunnel. Figure adapted from Kocher *et al.* [71].

2.1.1 Flat Plate & Vertical Cylinder Model Geometry

The first flowfield examined was based on a steel flat plate with a test surface of 203 mm × 182 mm that spanned the Mach 2 test section in order to keep the flow as two-dimensional as possible. The flat plate model was pylon-mounted to the test section floor and had a 10° sharp leading edge. In order to prevent flow separation at the leading edge, the model was mounted at a -5.4° (±1°) angle of attack. Based upon oblique shock relations, the edge Mach number was 1.8 and the freestream edge velocity reduced to 464 m/s behind the leading-edge shock. A vertical, brass cylinder 3.175 mm (0.125 in) in diameter (d) and 12.7 mm (0.5 in) tall (h) was mounted to the flat plate surface. The model height was four times the diameter in order to satisfy the recommendation of Dolling and Bogdonoff [72] that the cylinder height should be at least 2.4 times the diameter in order to be considered semi-infinite with respect to the interaction region. A semi-infinite height was desirable to eliminate the cylinder height as a scaling variable of the shock interaction. However, it is important to note that prior work suggests the semi-infinite scaling is also dependent on the incoming boundary layer thickness as described by Dolling [31] and Combs *et al.* [73]. A sketch of the flat plate model with the cylinder

installed is shown in Figure 2.2. The cylinder attachment holds the cylinder in place through top mounted screws in a downstream slot. This allows for precise cylinder locations downstream of the leading edge of the plate with positions varying from 6*d* (19.05 mm) to 25*d* (79.4 mm). The cylinder mounting holes were 112 mm downstream from the leading edge to prevent interference with the evolving boundary layer on the test region.

A laminar boundary layer on this model was not observed with transition starting almost immediately at the model leading edge. There were significant differences in shock wave behavior for varying cylinder positions, however, allowing for the use of this model for the study of transitional interactions. Based upon schlieren images, the turbulent boundary layer thickness was approximately 0.5 mm.

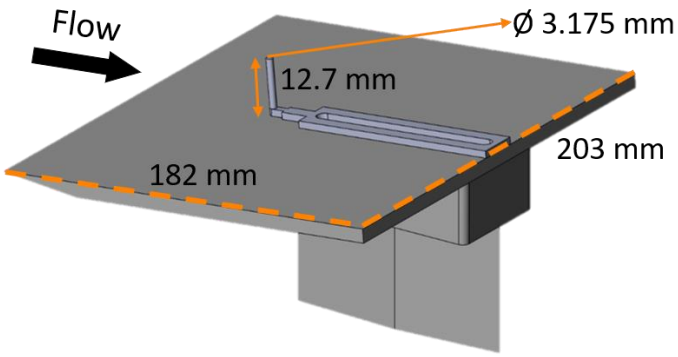

Figure 2.2. Schematic of the flat plate model for Mach 2 experiments with vertical cylinder shock generator.

2.1.2 Flat Plate & Blunt Fin Model Geometry

In addition to a vertical cylinder, a blunt fin shock generator was also tested on the same flat plate model. The blunt fin was 3.175 mm (0.125 in) diameter, 12.7 mm (0.5 in) tall, and 17.8 mm (0.7 in) long. The length of the fin is approximately $5.5\delta_{99}$ to eliminate concerns regarding effects from a wake from the vertical cylinder [74]. This model was mounted to the same flat plate model previously described. A schematic showing the blunt fin model on the flat plate is provided in Figure 2.3.

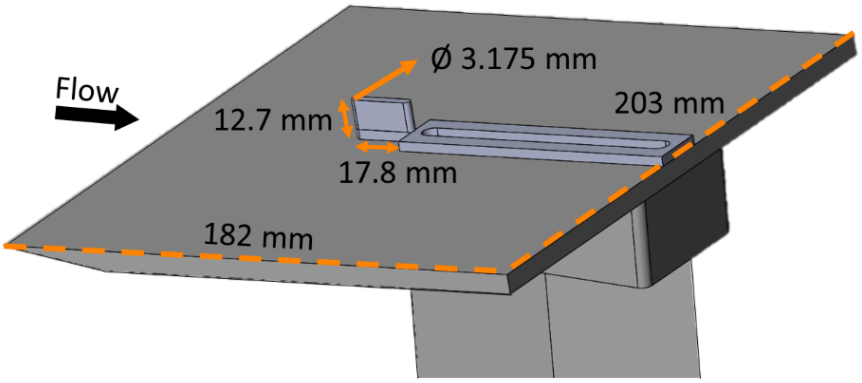

Figure 2.3. Schematic of the flat plate model for Mach 2 experiments with blunt fin shock generator.

2.1.3 Axisymmetric Cone & Vertical Cylinder Model Geometry

In addition to evaluating whether the wake of the vertical cylinder shock generator impacted the shock dynamics, the finite span of the flat plate model was a concern as a possible source of the high-intensity unsteadiness of the separation shock motion. In order to eliminate that as a source of concern, a vertical cylinder on a cone model was also examined. The author would like to thank Dr. Mark Gragston, James Chism, and Lauren Lester for designing and collecting this data set. A 10° half-angle cone at the front end of a cylindrical body was strut mounted to the test section floor; the cone angle was chosen to match the Mach edge condition of 1.8 to that of the flat plate model. The vertical cylinder was designed to be identical to the one used in the flat plate experiments with a diameter of 3.175 mm (0.125 in) and a height of 12.7 mm (0.5 in). The cylinder could be placed perpendicular to the cone surface at three discrete locations from the cone nose: x/d = 6.25, 9.5, or 12.5. Figure 2.4 shows the cone model with the vertical cylinder in the 12.5d position. The cone nose is approximately in the center of the test section so as to avoid sidewall contamination on the natural evolution of the boundary layer.

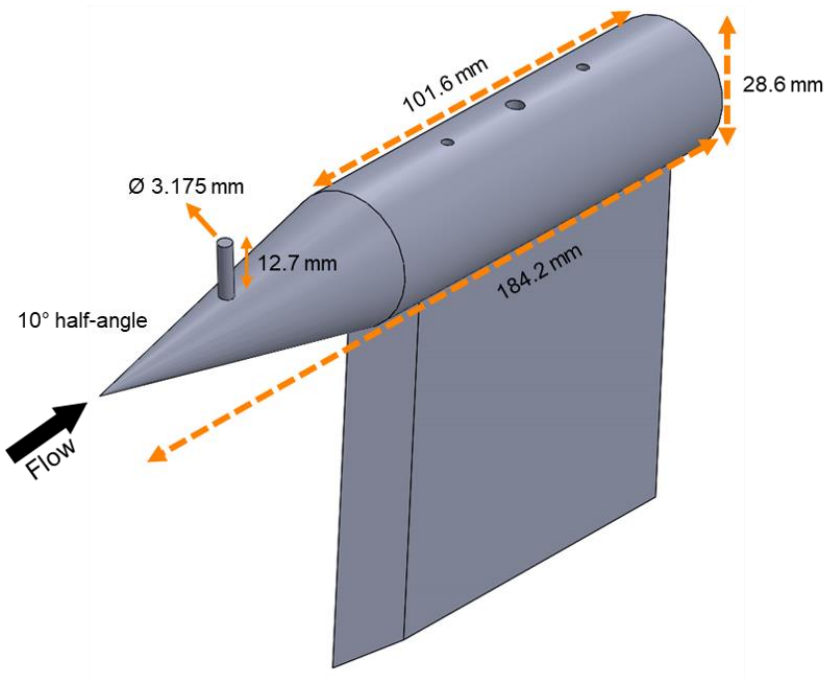

Figure 2.4. 10° half-angle cone model schematic with the vertical cylinder installed 12.5*d* downstream from the cone nose. The vertical cylinder can be placed in any of three positions by rotating the cylindrical body on the strut.

2.1.4 Schlieren Flow Visualization & Analysis Methods

The primary diagnostic used for this work was schlieren flow visualization. A traditional Z-type optical setup was employed using two, 2.67 m focal length mirrors. A schematic of this setup is shown in Figure 2.5. There were slight differences in the setup depending on the model used and based upon hardware availability at the time. A Photron FASTCAM Mini UX100 high-speed camera was employed to acquire images with a selected frame rate of 100 kHz (1024 × 32 pixel resolution) with a 150 mm lens for the initial flat plate and vertical cylinder experiments. The maximum pixel resolution for this camera is 1280 × 1024 pixels at 4 kHz, however, the operational acquisition frame rate was based upon experience gained through previous experiments that revealed an acquisition > 25 kHz was best suited to statistically resolve the dynamics of the shock wave motion [75]. Approximately 25,000 to 50,000 images were acquired during each run. A pulsed light-emitting diode (Luminus Devices CBT-140) provided high-intensity

pulsed light with a 700 ns pulse duration to effectively freeze the motion of the shock structures in each image. This light source was developed by Dr. Phillip Kreth at UTSI and was based on the work of Willert *et al.* [76].

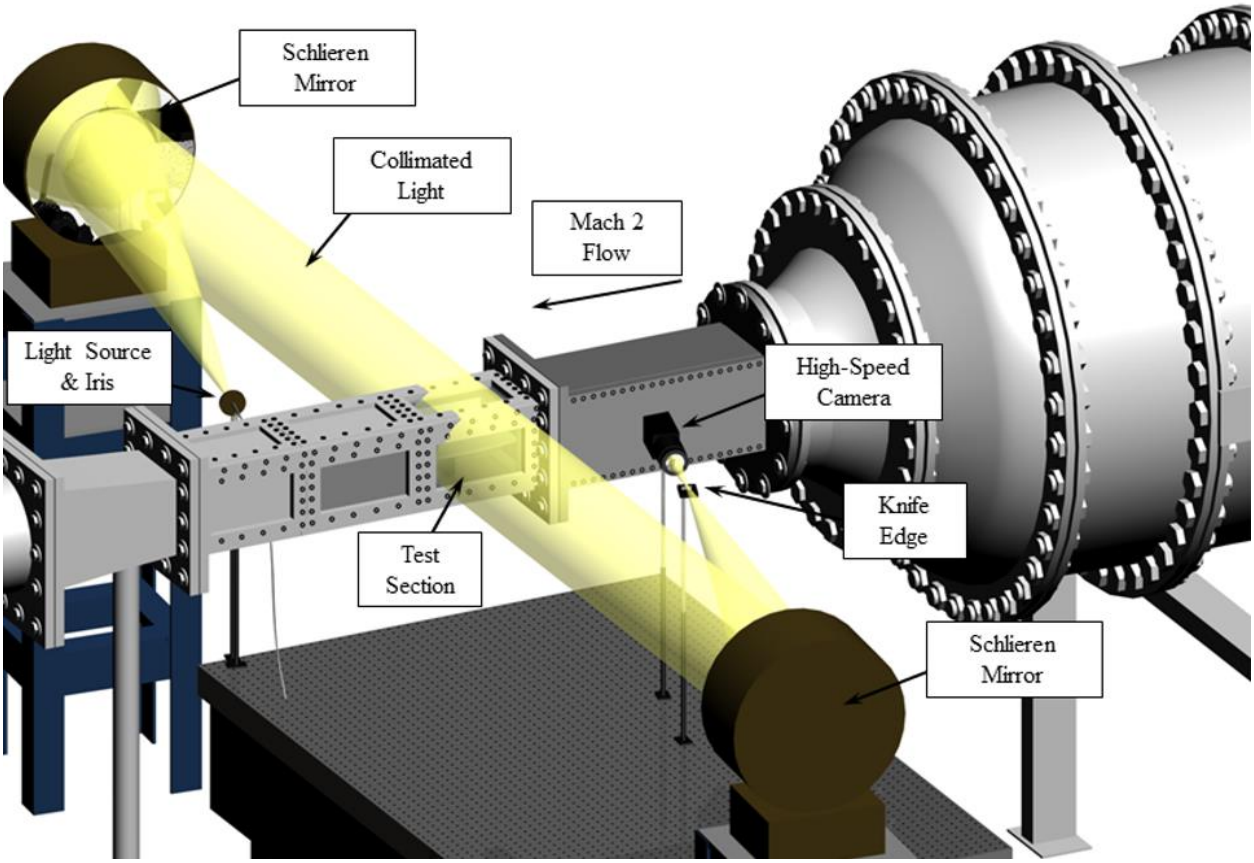

Figure 2.5. Schematic of the high-speed schlieren experimental setup in the UTSI Mach 2 facility [77].

A different camera was employed for the blunt fin experiments, but in the same configuration as Figure 2.5. A Photron FASTCAM SA-Z high-speed camera with a 300 mm lens at a selected frame rate of 200 kHz (1024 × 72 pixel resolution) was used. The higher acquisition rate was to maximize the temporal resolution of the interaction unsteadiness until the limit that the spatial resolution would allow. The maximum pixel resolution of this camera is 1024 × 1024 pixels at 20 kHz. The camera/lens combination

enables increased imaging rates from prior experiments and greater magnification. Approximately 100,000 images were saved during each run in order to match the same time scale as the vertical cylinder setup. The same pulsed light-emitting diode was used at a 1 μs pulse width. The axisymmetric cone model experiments were conducted using the same Z-type schlieren optical setup with the Photron FASTCAM SA-Z high-speed camera at a 100 kHz frame rate (640 × 280 pixel resolution) and the same pulsed light-emitting diode.

A full field of view image for the flat plate and cylinder experimental setup is provided in Figure 2.6. The interaction region of interest encompasses the leading edge of the flat plate model to the trailing edge of the cylinder. The plate is positioned such that shocks emanating from the nozzle/test section junction do not interfere with the natural development of the boundary layer on the plate for any of the tested vertical cylinder or blunt fin positions. This remains true for the axisymmetric cone model as well.

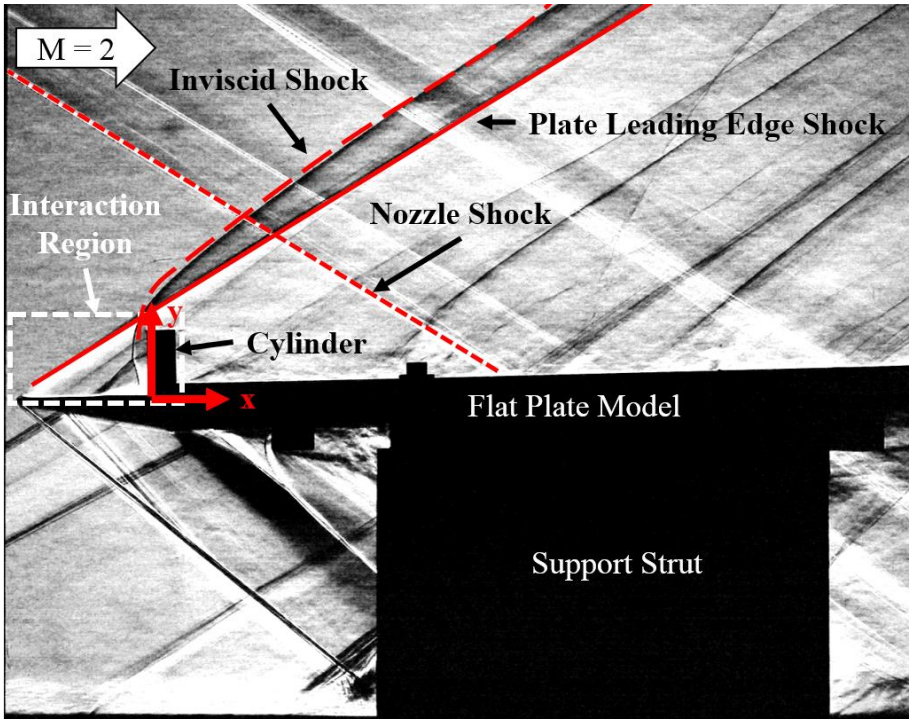

Figure 2.6. Global field of view for schlieren imaging for the Mach 2 freestream experiments. The focus of this work is on the interaction region, highlighted in the figure. Flow is from left to right.

A processing algorithm in MATLAB was developed by Combs *et al.* [78] to track the motion of each of the interaction features identified in Figure 1.4 in acquired schlieren images. This algorithm is discussed in greater detail by Combs *et al.* [78], who validated the technique by comparing the high-speed schlieren to high-speed surface pressure fluctuations for a fully turbulent SBLI. A detailed discussion of the algorithm and its validation is provided in Combs *et al.* [78], but some of the principle features are summarized here. All distances were non-dimensionalized by the measured shock generator diameter. As discussed by Combs *et al.* [78], the estimated position uncertainty of the shock detection system is ±8.2% (±0.2*d*). This analysis considered quantifiable uncertainties in the measurement of the diameter, the perceived width of the shock structures, the intersection location of the structures with the model surface, the angle of the structures, and the resolution of the images. Only cases where the separation shock was detected in more than 95% of the images were considered. During the processing of the schlieren images, the MATLAB algorithm occasionally failed to correctly detect the separation shock or the *UI* shock. If the algorithm encountered difficulties in identifying these features, then it assigned an *NaN* (not a number) for that image. Images where no *UI* shock was detected were left unchanged, since that feature is inherently intermittent. A best-guess interpolation for the separation shock position was applied using method 3 of the *inpaint_nans* function in MATLAB to evaluate difficult images [79].

2.2 Mach 2 Preliminary Data Results & Discussion

Prior to schlieren imaging data collection, preliminary surface oil flow experiments were performed in order to understand the mean separation structure and scaling upstream of the shock generator for the flat plate and vertical cylinder model. These images were acquired with the Photron FASTCAM Mini UX100 at a 50 Hz frame rate and 1280 × 1024 pixel resolution. Motor oil (5W-30) was mixed with titanium dioxide in a 4:1 ratio by volume for this technique. Oil flow images for a variety of cylinder positions on the flat plate model are shown in Figure 2.7. These images were taken from the top of the test section looking down on the top surface of the plate with the flow direction from left

to right and the cylinder is highlighted by a black circle. Only one image was selected from each run since oil flow visualization is a mean diagnostic, not a time-resolved one. The lack of laminar boundary layer on this model was partially determined from these oil flow images based on the separation structure, which supports the idea that the boundary layer begins transition close to the flat plate leading edge.

The shape of the separation is initially smooth, hyperbolic, and relatively symmetric. However, as the cylinder moves farther downstream, the spanwise deformities in the separation structure develop to such a degree that a maximum and minimum separation distance from the leading edge of the vertical cylinder may be identified. This is most evident in the *x/d* = 8 image. Once the interaction evolves to fully turbulent, the separation structure is once again smooth and symmetric around the centerline as shown in the *x/d* = 25 image.

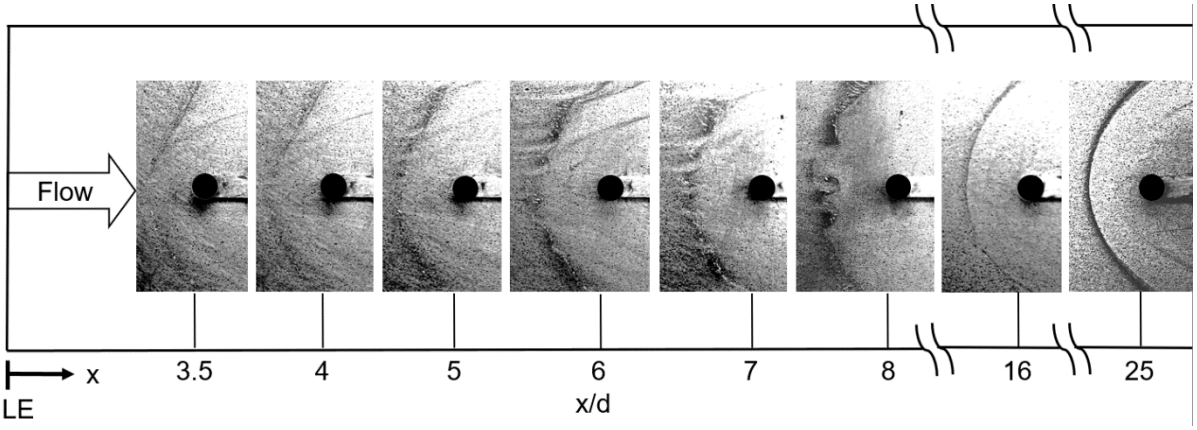

Figure 2.7. Surface oil flow visualization of the boundary layer separation as the cylinder moves downstream of the plate leading edge. Flow is from left to right.

The differences between these two cylinder positions are highlighted in Figure 2.8 with (a) for *x/d* = 8 and (b) *x/d* = 25. The apparent spanwise variation in the separation structure is indicative of a transitional interaction, and the resulting asymmetric shape remains across the entire interaction region, not just at the centerline. It is interesting that

this discontinuous shape is present in the mean, characteristic structure. The maximum and minimum centerline separation distances upstream of the cylinder are also labeled in Figure 2.8 for the transitional interaction. When a transitional interaction oil flow image is scaled and compared to an averaged schlieren image, the maximum separation distance observed in the oil flow image matches the location of the *UI* shock and the minimum separation distance matches the separation shock location in the schlieren image, as shown in Figure 2.8c.

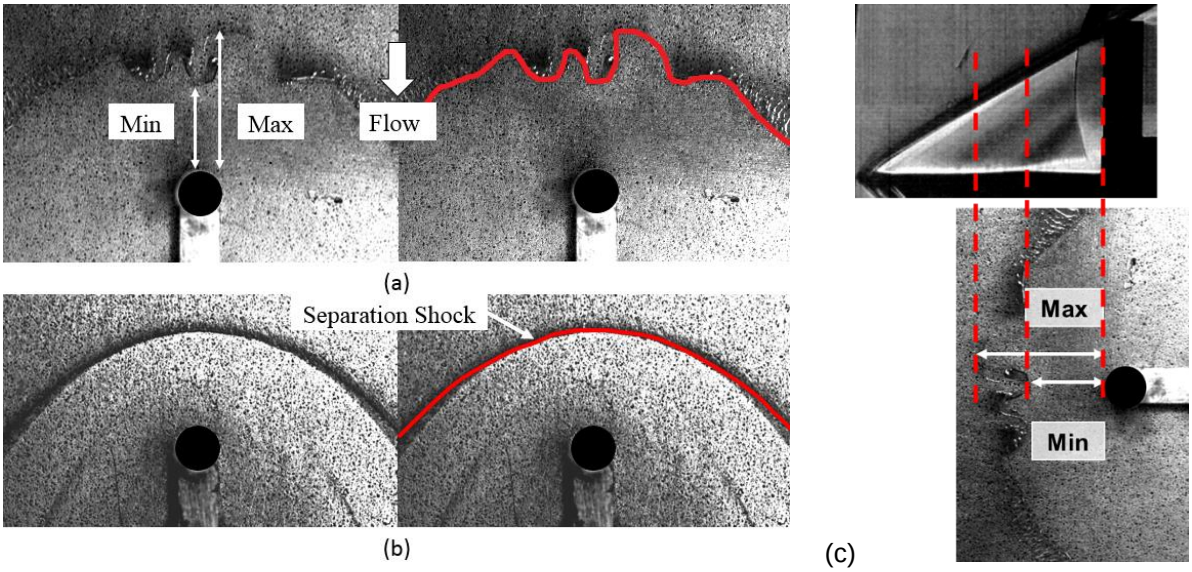

Figure 2.8. Surface oil flow visualization of boundary layer separation at (a) *x/d* = 8 and (b) *x/d* = 25 to compare a transitional and turbulent interaction, respectively, as taken from Figure 2.7. Flow is from top to bottom. (c) Comparison of shock wave location from an averaged schlieren image and boundary layer separation from an oil flow image for a transitional interaction at *x/d* = 8. Flow is from left to right.

A sample schlieren image sequence for the flat plate and vertical cylinder model is presented in Figure 2.9 for a transitional interaction (a) and a turbulent interaction (b). In the last image of each sequence, the shock structures are highlighted with the *UI* shock (green), separation shock, λ_1 (red), and closure shock, λ_2 (blue). The images are sequential from top to bottom and the flat plate model surface is visible for both interactions.

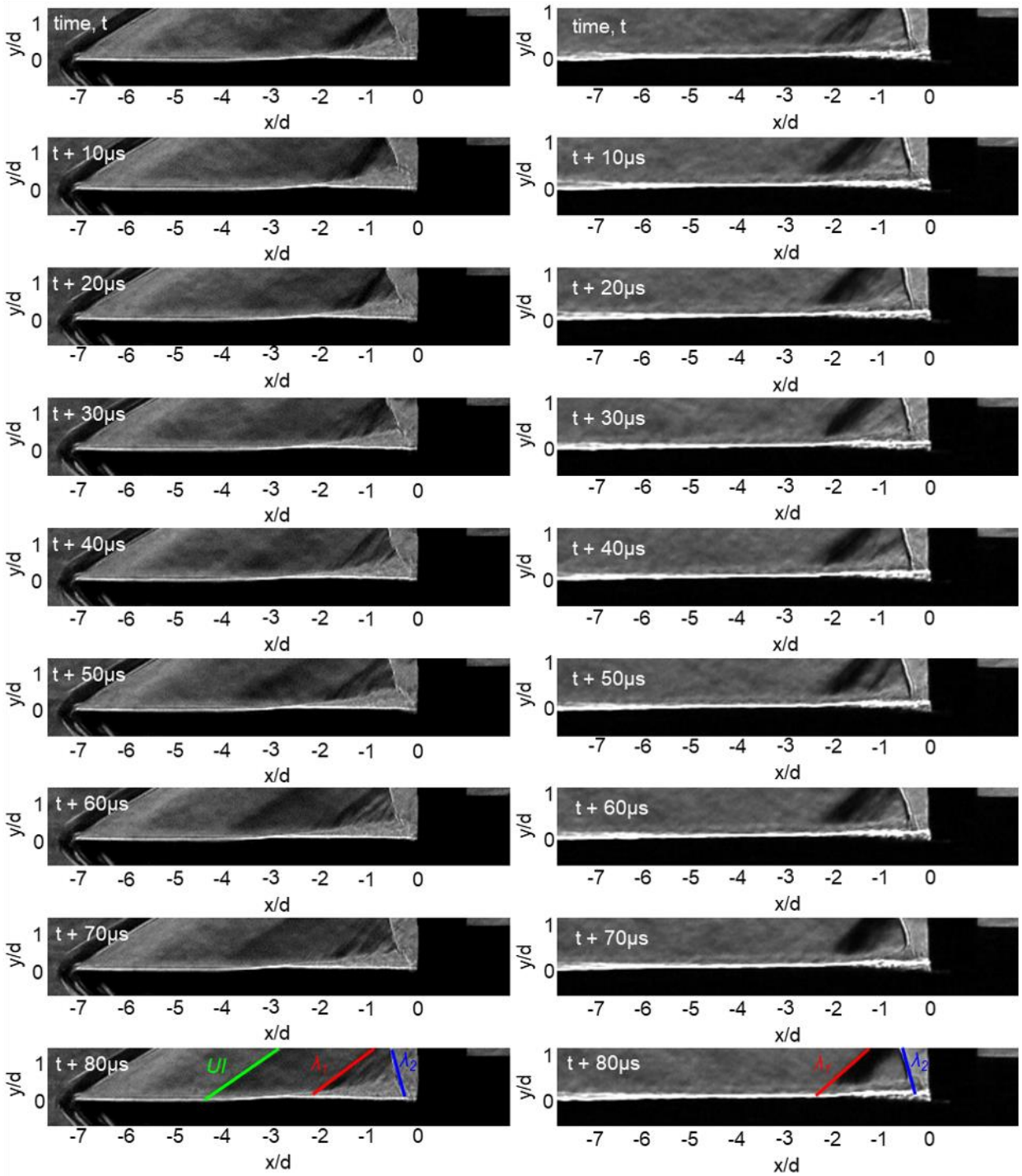

Figure 2.9. Representative schlieren image sequence demonstrating unsteady shock position for an (a) transitional interaction for cylinder position *x/d* = 7 and (b) turbulent interaction for cylinder position *x/d* = 25. In the last image of each sequence, the shock structures are identified. Flow is from left to right.

For the transitional interaction, the leading-edge shock is relatively steady, but the dynamic motion of the separation shock and the intermittency of the *UI* shock are clearly evident. Initially, the *UI* shock is very faint, but grows stronger in intensity and moves upstream during the course of the sequence. The presence of the *UI* shock appears to impact the strength and dynamics of the separation shock. In the first image at *t*, the separation shock is thick and dark. However, as the *UI* shock increases in strength (based on relative level of visibility), the separation shock appears weaker until it's almost difficult to resolve the shock leading edge from the expansion waves behind it at *t*+70*μs* and *t*+80*μs*. Also, a slight thickening in the boundary layer between the *UI* and separation shocks is visible that indicates the beginning of boundary layer separation. This boundary layer thickening feature moves upstream and appears to correlate to the *UI* shock position. At the beginning of the sequence, it is closer to an *x/d* position of -2*d*, but by the end, is at -3*d*. In the turbulent interaction sequence, no *UI* shock is apparent, but there is still evident unsteadiness in the separation shock position and strength. The same onset of separation near the flat plate surface is evident, but it remains almost immediately under the separation shock position or a little downstream of it. For both cases, the closure shock remains relatively steady about -0.25*d* upstream of the vertical cylinder face.

As previously mentioned throughout Chapter One, blunt fins as shock generators have also been historically studied, particularly by Kaufman *et al.*[65] and Dolling *et al.* [31],[72],[74],[80]. Although Kaufman *et al.* [65] did provide some discussion for an incoming transitional boundary layer, the focus of these earlier works has been primarily on turbulent boundary layer interactions in which dynamic surface pressure measurements and rudimentary flow visualization were used to characterize the unsteady shock motion. Furthermore, the emphasis of that effort was generally on the scaling of the separation with the fin diameter or various sweep angles. Recent computational efforts by Mortazavi and Knight [36] focused on the aerothermal effects, but still for only laminar and turbulent interactions. With this in mind, direct comparisons between a vertical cylinder and blunt fin shock generators were performed in order to ensure that the

effects of the cylinder wake did not have a significant impact on the upstream interaction dynamics.

A sample schlieren image sequence for the flat plate and blunt fin model is presented in Figure 2.10 for a transitional interaction (a) and a turbulent interaction (b). In the last image of each sequence, the shock structures are highlighted with the *UI* shock (green), separation shock, λ_1 (red), and closure shock, λ_2 (blue). The images are sequential from top to bottom and the flat plate model surface is visible for both interactions. For the transitional interaction, the leading-edge shock is relatively steady, but the dynamic motion of the separation shock and the intermittency of the *UI* shock are clearly evident. Intermittency in this instance means the intermittent presence of the *UI* shock in the schlieren images. Very similar trends to those presented for the vertical cylinder configuration in Figure 2.9 are qualitatively observed. For example, in the transitional interaction of Figure 2.10a, the *UI* shock begins relatively weak at *t,* then increases in strength to *t* + 80μs. The motion of the *UI* shock from near λ_1 to upstream is also evident. Furthermore, the apparent corresponding weakening of the λ_1 shock as the *UI* shock increases in intensity is also evident. In addition, the location of upstream separation, as evident by a small thickening near the flat plate surface, appears to be highly correlated to the position of the *UI* shock. For the turbulent interaction in Figure 2.10b, the separation shock is much stronger throughout the image sequence than in the transitional interaction of (a), and varies between -2*d* to -3*d* upstream of the blunt fin. In this case, the boundary layer separation adjacent to the model surface remains immediately downstream of the separation shock structure. For both cases, the closure shock, λ_2, is relatively stable -0.25*d* upstream of the blunt fin.

The analysis presented in this work for the cone and vertical cylinder model will be relatively brief, and merely serves to highlight that the full test section span and any resulting sidewall effects on the flat plate model are not a contributing factor to the characteristic nature of the transitional interaction dynamics.

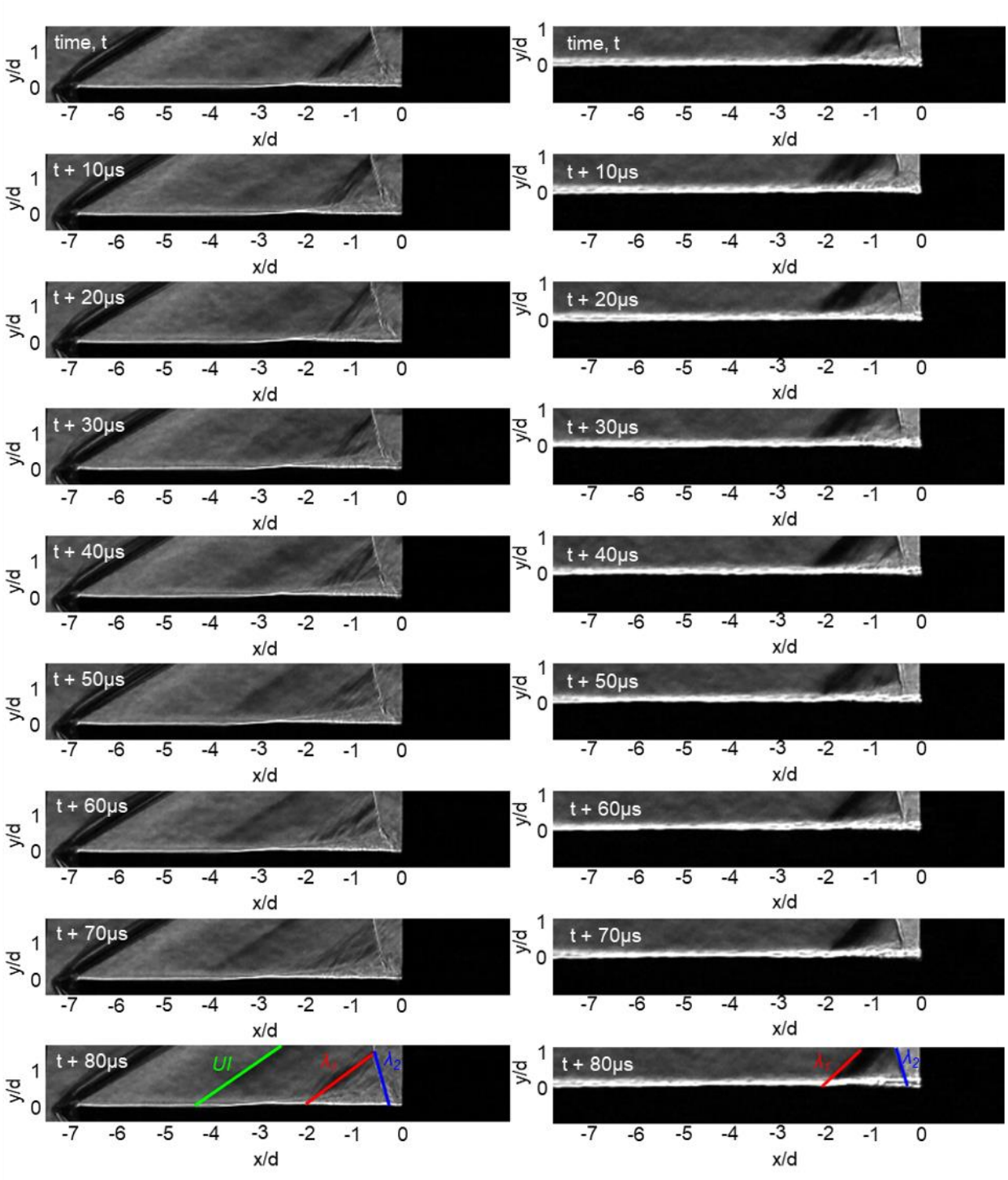

Figure 2.10. Representative schlieren image sequence demonstrating unsteady shock position for an (a) transitional interaction for blunt fin position x/d = 7 and (b) turbulent interaction for blunt fin position x/d = 24. In the last image of each sequence, the shock structures are identified. Flow is from left to right.

A sample schlieren sequence of the interaction region at the three vertical cylinder positions on the cone model is provided in Figure 2.11 with (a) x/d = 6.25, (b) x/d = 9.5, and (c) x/d = 12.5 from the cone nose. The *UI* shock (green), separation shock, λ_1 (red) and closure shock, λ_2 (blue) are labeled in the final images of the image sequence and the flow is from left to right. The leading edge of the vertical cylinder is on the far right-hand side of each image. In the images of Figure 2.11a, the leading-edge shock emanating from the cone nose is the first flow feature visible on the far-left side. For the other two cylinder positions in (b) and (c), a shock from a discontinuity in the test section floor is occasionally visible upstream of the *UI* shock. In Figure 2.11a, the *UI* shock is visible in every image, whereas it is not initially present in either (b) or (c) and slowly emerges. Unlike the transitional interactions on the flat plate model, it is less obvious that the *UI* shock emanates from the separation shock and moves upstream.

The *UI* shock more appears at t + 30μs in (b) and t + 40μs in (c) already distinct from the separation shock before moving upstream. However, for all three cylinder positions, as the relative strength of the *UI* shock increases, the strength of the separation shock decreases, before the separation shock strength recovers. Strength in this instance refers to the increased level of contrast in the schlieren images. This is consistent with the previously discussed transitional boundary layer interactions on the flat plate model and is most evident in Figure 2.11b from t + 40μs to t + 70μs. The presence of the *UI* shock for all three cases is an indicator that a fully turbulent incoming boundary layer was not achieved. For all three cases, the scaling of the separation shock remains between -1.5d and -2d while the *UI* shock is between -2d and -4d upstream of the vertical cylinder. Qualitatively, the closure shock is relatively steadier than on the flat plate model, remaining around -0.2d upstream with very little motion.

Now that some initial oil flow and schlieren visualization images have been presented, it is important to note the difficulties in this setup in evaluating the boundary layer characteristics specifically. The evolution of the boundary layer separation structure, as evidenced by Figure 2.7, indicate that there is an evolution of state within the incoming boundary layer that changes the boundary layer separation structure.

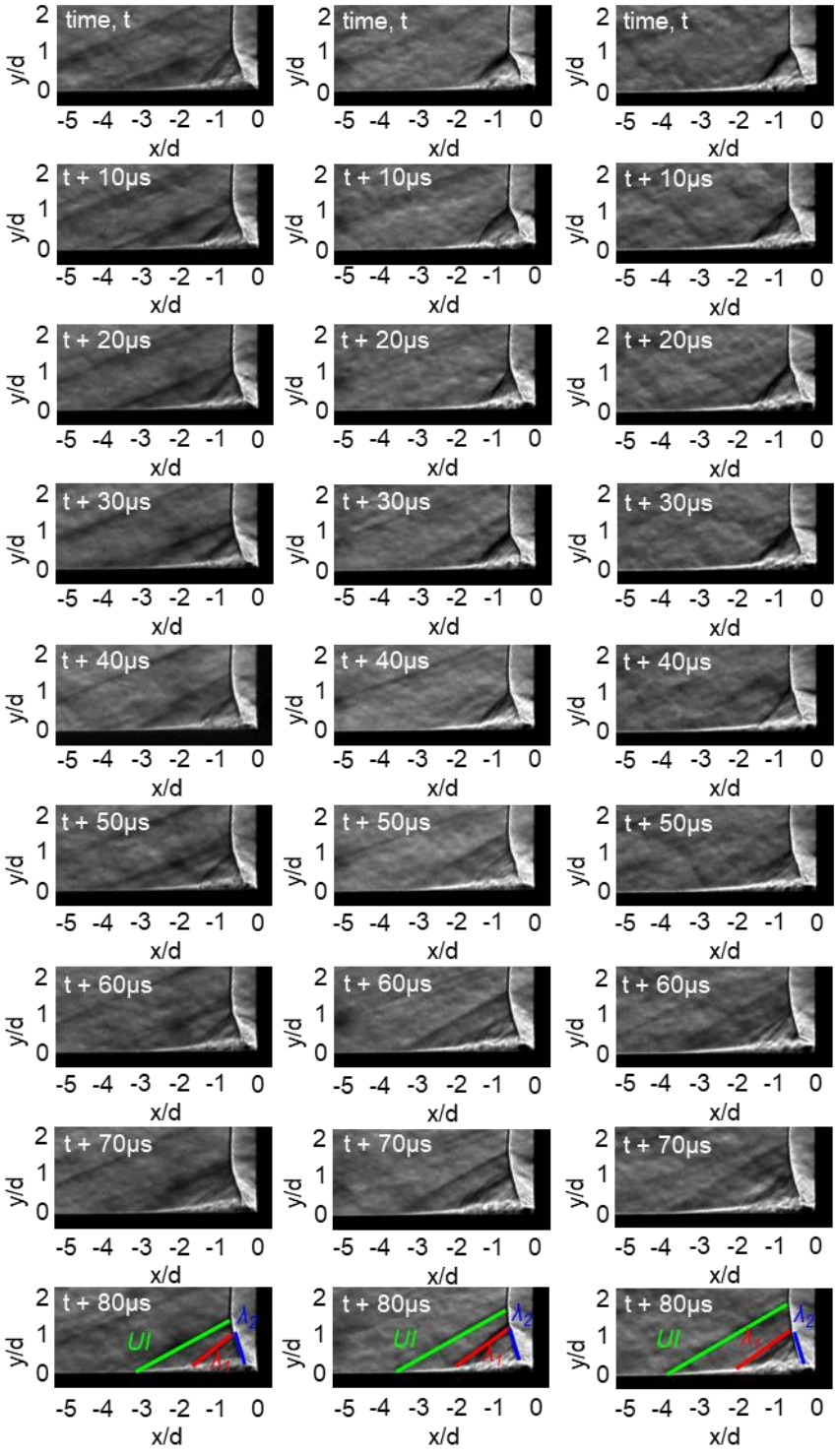

Figure 2.11. Representative schlieren image sequence demonstrating unsteady shock positions for three vertical cylinder locations on a 10° half-angle cone model with (a) *x/d* = 6.25, (b) *x/d* = 9.5, and (c) *x/d* = 12.5. In the last image of each sequence, the shock structures are identified. Flow is from left to right.

However, the path-integrated nature of schlieren combined with the flat plate model spanning the entire wind tunnel test section creates difficulty in discerning characteristic boundary layer observations directly. Furthermore, the relatively high Reynolds number associated with this flowfield creates a very thin boundary layer (~0.5 mm), increasing the difficulty in resolving turbulent structures. The focus of this work will be on how the interaction structure evolves as the boundary layer evolves.

The conclusion that a laminar boundary layer (and thus a laminar interaction) was never achieved was based upon observations of the separation structure and the mean characteristic position of the various shock waves compared to extensive laminar interaction results from the literature. First, the boundary layer separation structure in the oil flow images should look very similar to the turbulent interaction case, but with larger separation scales. The corresponding separation shock, as briefly observed in the schlieren montage figures and will be discussed in greater detail in the subsequent chapter, doesn't change much in scale as the shock generator moves downstream. There is a distinct compression of the *UI* shock and separation shock near the flat plate leading edge, which is counter to the expected behavior as demonstrated by Figure 1.9. In the context of this work, the state of the boundary layer is based on the observations of the interaction structure based on the results from prior work in the literature

One of the simplest methods of looking at the shock position from the shock tracking algorithm is a temporal trace of the shock wave positions upstream of the shock generator. A sample for the separation shock and closure shock for a transitional interaction at x/d = 7 and a turbulent interaction at x/d = 25 are shown in Figure 2.12 below for the flat plate and vertical cylinder model. The difference in mean position of the closure shock, λ_2, between the two interactions is approximately 0.25d, and for the separation shock, λ_1, approximately 0.1d. However, from these traces, it appears as if there is a greater region of unsteady motion for the transitional interaction in Figure 2.12a, with values ranging over 1.5d vs. values ranging over 0.75d for the turbulent interaction in Figure 2.12b. Qualitatively for this same time range of motion, there appears to be a periodic trend to the separation shock motion in the transitional interaction that is not present in the turbulent interaction case.

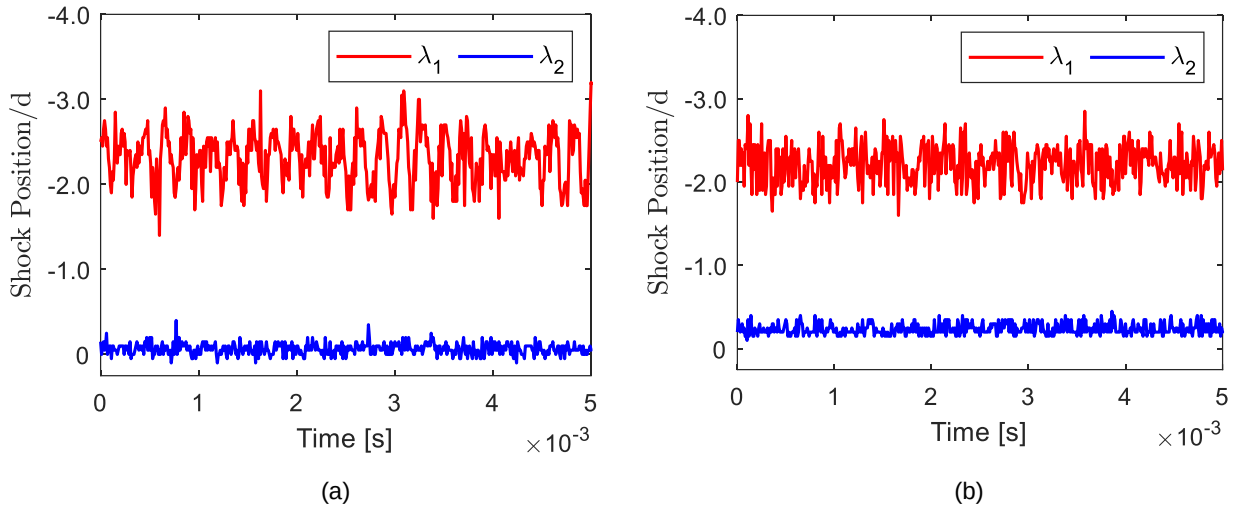

Figure 2.12. Raw temporal plots comparing the separation shock, λ_1, and closure shock, λ_2, locations for a transitional interaction at x/d = 7 (a) and a turbulent interaction at x/d = 25 (b) for a vertical cylinder shock generator.

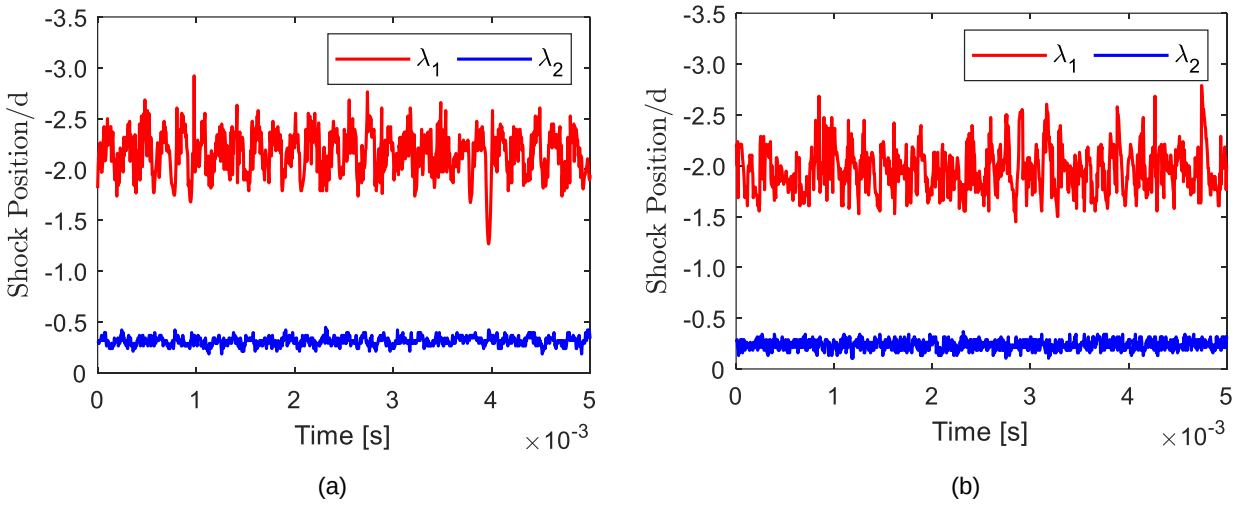

Figure 2.13. Raw temporal plots comparing the separation shock, λ_1, and closure shock, λ_2, locations for a transitional interaction at x/d = 7 (a) and a turbulent interaction at x/d = 24 (b) for a blunt fin shock generator.

Just as with the vertical cylinder interaction, sample temporal plots of the blunt fin generated shock motion are provided. In Figure 2.13, the separation shock and closure shock positions for a transitional interaction at x/d = 7 and turbulent interaction at x/d = 24 are shown in (a) and (b), respectively. The closure shock, λ_2, remains relatively

constant for both positions and has a lower level of unsteadiness compared to the separation shock, λ_1. The separation shock moves closer to the blunt fin face as the incoming boundary layer transitions to turbulent. The separation shock in the transitional interaction case in (a) appears to vary between -1.75*d* and -2.5*d*, whereas in the turbulent interaction in (b) it varies between -1.5*d* and -2.2*d*.

An additional method to evaluate the unsteady motion of the shock wave positions is through probability density functions (PDF). The PDF for the separation shock motion for the same transitional interaction at x/d = 7 and turbulent interaction at x/d = 25 for the flat plate and vertical cylinder model as shown in Figure 2.12 are provided in Figure 2.14. Similar to the observations made of the temporal trace in Figure 2.12, the range of motion of the separation shock upstream of the cylinder is only slightly larger for the transitional interaction than for the turbulent interaction in Figure 2.14. The comparative height of the bins is an indicator of how much time the shock is at that position compared to the other positions. So, although the two separation shocks span similar ranges upstream of the shock generator, the turbulent interaction PDF has a narrower peak than the transitional interaction, meaning the shock feature is located more frequently in the narrow band of -2*d* and -2.5*d*, whereas for the transitional interaction, the probability for a given location is more spread out. Boundary layers continue to grow in thickness, meaning that even though for incoming turbulent interactions the separation scale remains at approximately -2*d* (recall Figure 1.9) the scale continues to decrease from a boundary layer thickness reference.

The PDF of the separation shock for the flat plate and blunt fin shock generator are shown in Figure 2.15 a transitional interaction at x/d = 7 and a fully turbulent interaction at x/d = 24. As expected, the mean position of the separation shock was approximately 0.25*d* closer to the blunt fin face for the turbulent interaction than the transitional interaction [81]. The range of the shock wave motion varies roughly the same for both interactions from -1.5*d* to -2.7*d*. From these two sample cases alone, it is difficult to characterize the evolution of shock wave unsteadiness from incoming transitional to turbulent boundary layers given the relative similarity of their probability profiles.

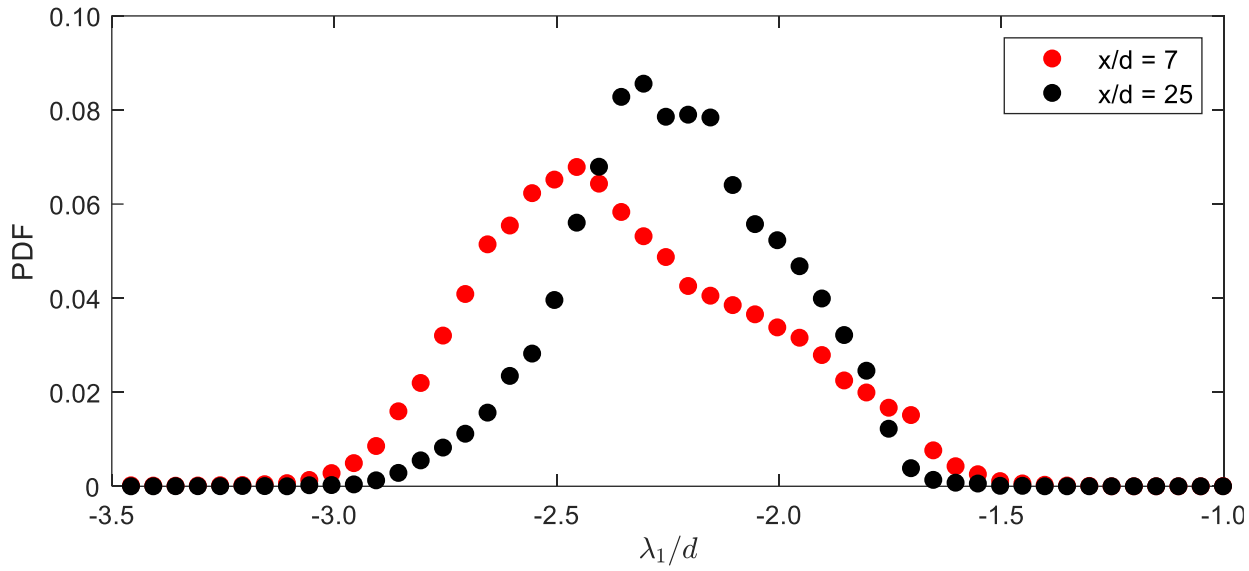

Figure 2.14. Probability density functions of the separation shock motion for a transitional interaction at *x/d* = 7 and a turbulent interaction at *x/d* = 25 for the vertical cylinder shock generator.

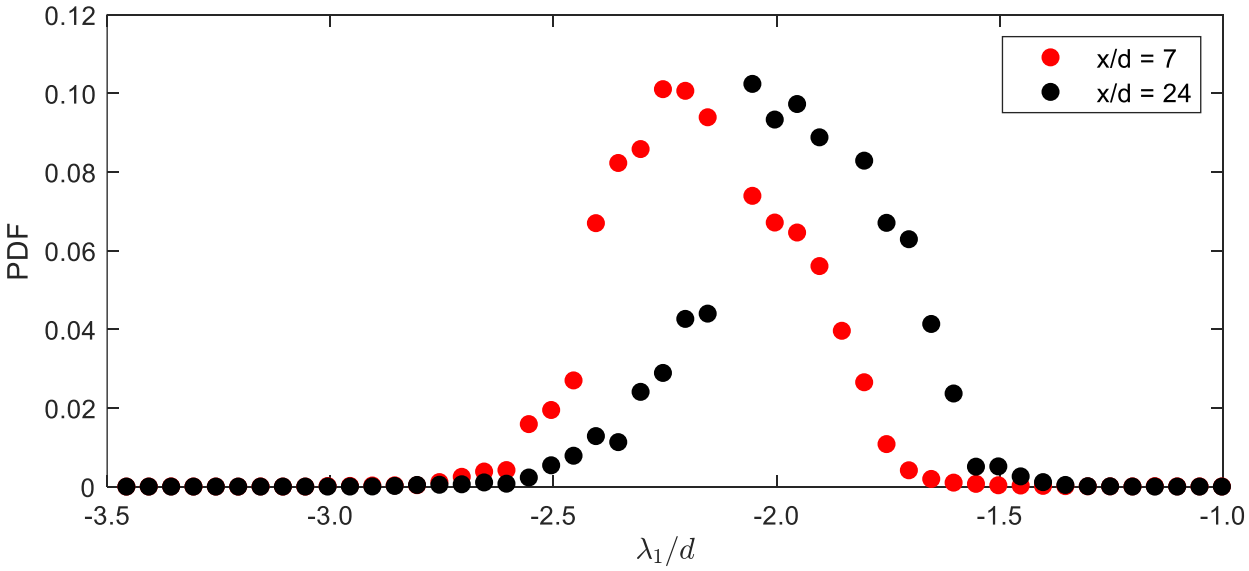

Figure 2.15. Probability density functions of the separation shock motion generated by a blunt fin on a flat plate for a transitional interaction at *x/d* = 7 and a turbulent interaction at *x/d* = 24.

Before discussing the statistical moments for the separation shock in greater detail, it is valuable to compare the PDF of the three shock waves for the transitional interaction of *x/d* = 7 to each other for each of the shock generators on the flat plate model. In Figure 2.16, the same PDF of the separation shock at *x/d* = 7 from Figure 2.14 is compared to the *UI* shock and closure shock from the same test run. The *UI* shock PDF appears to have a slight right tail (positive skew, see Figure 3.2), which was expected given the qualitative observation from the raw schlieren images that the *UI* shock emanates from separation shock and moves upstream as discussed in Figure 2.9. The mean *UI* shock location is -4.4*d* compared to the mean separation shock location of -2.3*d* and closure shock mean of -0.08*d*. The closure shock has a much smaller level of unsteadiness compared to the other two shock structures, varying only from approximately zero to -0.4*d*.

The same comparison for a blunt fin position of *x/d* = 7 is shown in Figure 2.17. In this figure, the same separation shock PDF at from Figure 2.15 is duplicated. The *UI* shock also appears to have a slight right tail (positive skew), which was expected given the qualitative observations of the *UI* shock emanating from the separation shock as discussed in Figure 2.10. The mean *UI* shock location is -4.4*d* compared to the mean separation shock location of -2.2*d* and closure shock mean of -0.29*d*. The closure shock has a much smaller level of unsteadiness compared to the other two shock structures, varying only from approximately -0.13*d* to -0.33*d*.

Some initial differences observed in the PDF between the two shock generators in Figure 2.16 and Figure 2.17 are the more narrow ranges of motion in all three shock waves for the blunt fin shock generator. However, the mean locations of the *UI* and separation shocks are the same for both shock generators. The closure shock in the vertical cylinder interaction remains closer to the cylinder face by approximately the shock tracking algorithm uncertainty of 0.2*d*. Because this difference is so small, this may not be an artifact of the different shock generators, but could be within the analysis uncertainty. However, this may also mean that there is a slight influence on the closure shock characteristics with the immediate relief downstream of the vertical cylinder that the blunt fin length counteracts, resulting in the larger standoff distance.

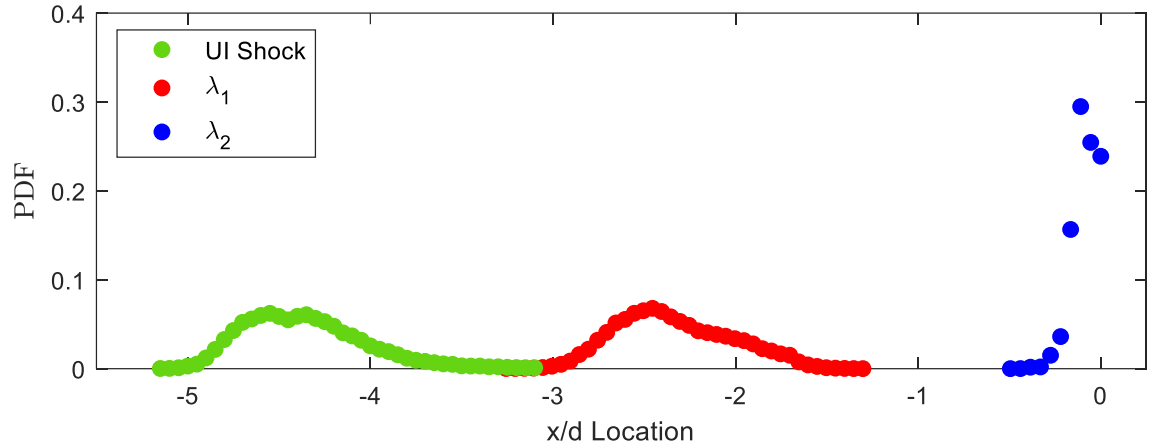

Figure 2.16. Probability density functions of the *UI* shock, separation shock, and closure shock motion for a transitional interaction at vertical cylinder position *x/d* = 7.

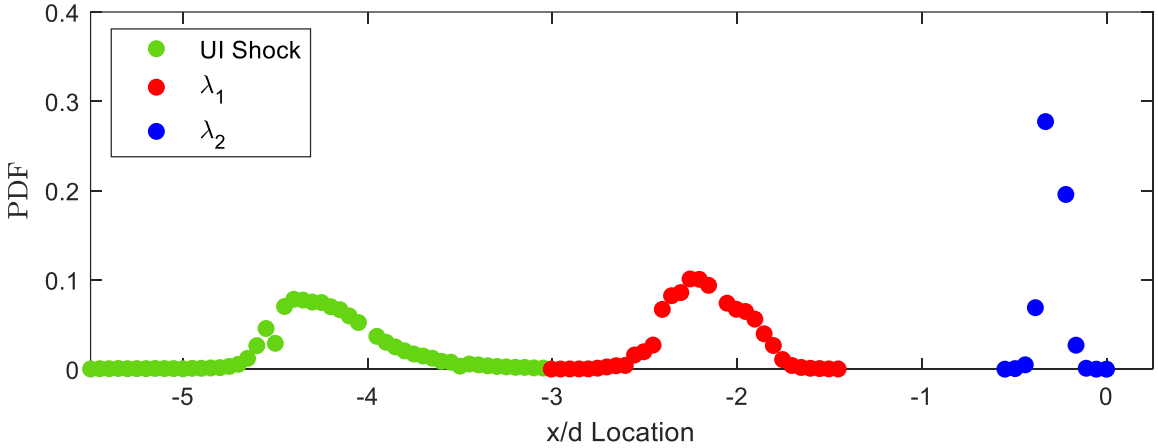

Figure 2.17. Probability density functions of the *UI* shock, separation shock, and closure shock motion for a transitional interaction at blunt fin position *x/d* = 7.

This chapter introduced the experimental conditions in the Mach 2 facility, the three model configurations, and provided an initial analysis of the differences between transitional interactions and turbulent interactions for the vertical cylinder and blunt fin shock generators on the flat plate model. The evolution of the statistical moments of these shock waves and a spectral characterization as the incoming boundary layer evolves to fully turbulent is provided in the subsequent chapter. A more in-depth comparison

between the vertical cylinder and blunt fin shock generators on the flat plate model is also discussed. Notable characteristics of the cylinder on the cone model are also presented in Chapter Three.

Chapter Three

EVOLUTION OF INTERACTION DYANMICS WITH VARYING BOUNDARY LAYER CONDITIONS

The previous chapter provided a description of the experiment and a preliminary introduction to the initial differences in the interaction behavior for incoming transitional and turbulent boundary layers. The focus of this chapter will be to evaluate how the unsteady dynamics change with an evolving incoming boundary layer and compare the results between the different shock generators.

3.1 Varying Shock Generator Position Data Results & Discussion

Statistical moments for the separation shock for various vertical cylinder positions are shown in Figure 3.1. These provide a more accurate representation of the motion of the shock waves. A total of eight cylinder positions were evaluated as a part of this analysis: x/d = 6, 7, 8, 9, 10, 11, 15, 25. The mean separation shock location remained between -2d and -2.5d upstream of the cylinder face. There are some interesting trends that result from the standard deviation, skewness, and kurtosis. In Figure 3.1a, the standard deviation, σ, initially increases for transitional interactions from 0.25d to 0.35d, and then decreases for the fully turbulent interaction at x/d = 25 to 0.24d. This indicates that there could be a peak point of unsteady motion for the separation shock within the transitional boundary layer regime, and that transitional interactions are inherently more unsteady than fully turbulent interactions, consistent with the observations from Refs. [3],[11]-[16].

The skewness, α_3, of the separation shock motion is provided in Figure 3.1b, and the kurtosis, α_4, in Figure 3.1c. The first three cylinder positions have a negative

skewness, meaning that the separation shock is skewed closer to the cylinder face resulting in smaller separation distances. The remaining positive skew values indicate larger levels of separation upstream of the cylinder face with the largest skew towards the end of transition at *x/d* = 15. The skewness then decreases again for the fully turbulent interaction at *x/d* = 25. A skew of zero could indicate a Gaussian distribution.

The kurtosis in Figure 3.1c indicates how outliers in the separation shock position affect the mean value. There is a general decrease in the kurtosis in the transitional region from approximately 3 to 2.3. The kurtosis then increases again to 2.7 for the fully turbulent interaction at *x/d* = 25. A Gaussian distribution has a kurtosis of 3. Given the low levels of skewness and the relatively small standard deviations for the different cylinder positions, kurtosis values around 3 are not surprising. It is consistent that the turbulent interaction, which had a near zero skew, has an almost Gaussian distribution. However, overall, there were relatively few outliers for any of the cylinder positions that affected the mean values of the separation shock.

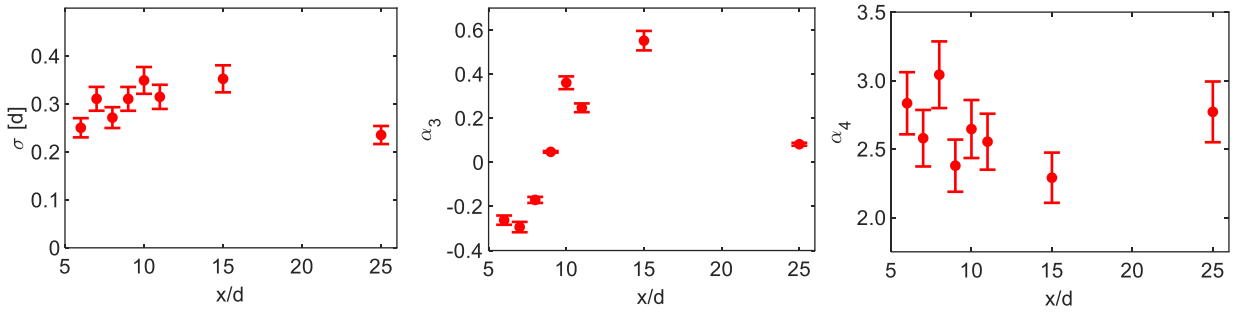

Figure 3.1. Statistical moments for the separation shock foot motion for varying cylinder locations: (a) standard deviation, (b) skewness, and (c) kurtosis.

The same statistical moments for the *UI* shock are shown in Figure 3.2. Data for the *UI* shock at a cylinder position of *x/d* = 25 are not included, because the *UI* shock is not present for a fully turbulent incoming boundary layer interaction. As *x/d* increases, the standard deviation increases from 0.22*d* to 0.51*d*, implying larger levels of unsteadiness.

The decrease to 0.42*d* at *x/d* = 15 could be a result of the decrease in the *UI* shock intermittency in the flow (see Figure 3.3). The same cylinder location that had the maximum standard deviation for the separation shock is not the same location as the maximum standard deviation for the *UI* shock. This implies that there is not a correlation between the relative level of unsteadiness between the separation and *UI* shocks.

The skewness of the UI shock location for every cylinder position evaluated in Figure 3.2b was negative. This is counter-intuitive to the *UI* shock PDF presented in Figure 2.16 for *x/d* = 7; the PDF showed a right tail, which is in line with a positive skew and quantifies the *UI* shock position farther from the separation shock. However, these skew values are all negative, meaning a left tail with positions closer to the separation shock with the average position closer to the cylinder face than the median. There appears to be a relation between those *UI* shock positions with the smallest skew having kurtosis values closer to Gaussian. The cylinder position at *x/d* = 6 had the largest *UI* shock skew at -1.7, and has the largest kurtosis at 9.7. This means that the relatively large left tail impacted the location of the mean *UI* position upstream of the cylinder and its unsteady motion from the separation shock was captured. The rest of the cylinder positions have *UI* kurtosis values between 4.3 and 6. The cylinder position with the largest standard deviation, *x/d* = 11, has a kurtosis of 5.5, meaning there were not many outliers that contributed to this increase in standard deviation.

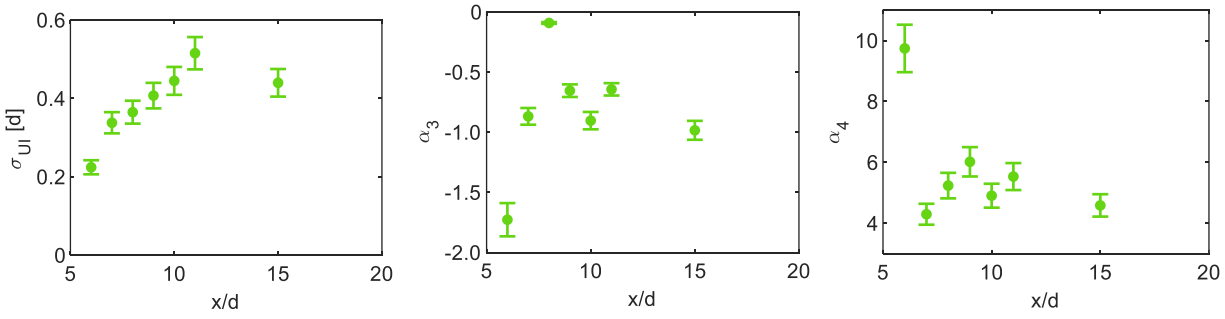

Figure 3.2. Statistical moments for the *UI* shock motion for varying cylinder locations: (a) standard deviation, (b) skewness, (c) kurtosis.

As previously mentioned, the *UI* shock is only a feature of transitional boundary layer interactions as first observed by Dolling and Brusniak [24]. One of the major ways this can be determined is from the *UI* intermittency, γ_{UI}. This is the percentage of time that the shock feature is present during a test run. The *UI* intermittency is shown in Figure 3.3 for the vertical cylinder shock generator. For cylinder positions closest to the flat plate leading edge, the *UI* shock was present approximately 84% of the time. It then drops down to nearly 50%, then to 0.03% for the fully turbulent interaction at x/d = 25. It is this very low value that motivates the exclusion of the *UI* shock data at this position in previous analyses for that shock generator location. The uncertainty associated with γ_{UI} is difficult to quantify; as the feature is intermittent, the primary source of uncertainty would be when the *UI* shock exists in a frame, but the shock tracking algorithm fails to identify its presence. Given that large data sets required the use of the shock tracking algorithm to begin with (50,000-100,000 images), it is not practical to individually track the accuracy of identifying the *UI* shock.

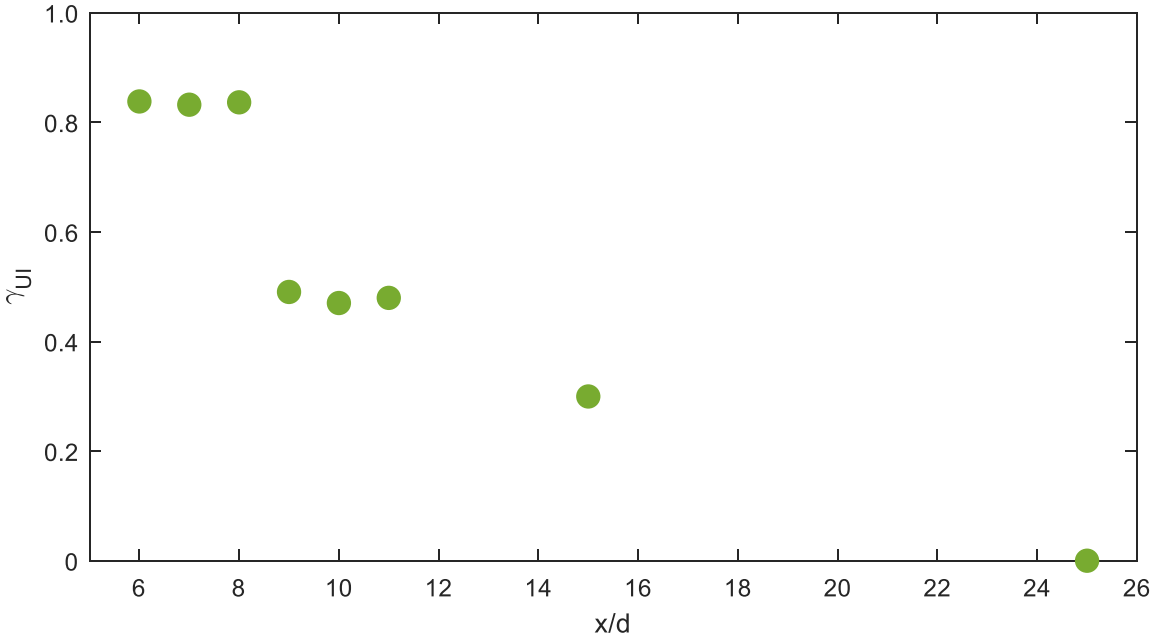

Figure 3.3. The upstream influence shock intermittency at various cylinder positions.

Although the general ~8% uncertainty associated with the shock tracking algorithm, as described in more detail by Combs *et al.* [78], could be applied, this represents the uncertainty in the algorithm identification of the correct position and not the potential for false positives. One method to estimate the uncertainty of γ_{UI} is to take a sample set of a few thousand images and go through by hand and determine how many false identifications the shock tracking algorithm made, then scale that number up based on the total number of images in the test run. That method was not applied for this work.

The statistical moments for the separation shock and *UI* shock are shown below for varying blunt fin positions on the flat plate model. A total of eight blunt fin positions on the flat plate model were evaluated: x/d = 6, 7, 8, 9, 10, 11, 15, and 24. The mean separation shock location for all of the blunt fin locations remained between -1.9d and -2.2d upstream of the blunt fin face. However, some interesting trends in the standard deviation, skewness, and kurtosis of the separation shock and *UI* shock positions are observed. The statistical moments for the separation shock are presented in Figure 3.4. In Figure 3.4a, the standard deviation, σ, decreases from 0.25d to 0.17d from x/d = 6-15, then increases slightly to 0.21d for the fully turbulent interaction at x/d = 24. As the incoming boundary layer evolves to fully turbulent, the overall level of unsteadiness of the separation shock motion decreases.

The skewness, α_3, of the separation shock is shown in Figure 3.4b, and the kurtosis, α_4, is shown in Figure 3.4c. The first two blunt fin positions have a negative skew, meaning that for those transitional interaction cases, the separation shock is downstream (closer to the blunt fin face) of the median position than upstream. This is most likely a result of the *UI* shock influence. For the remainder of the blunt fin locations, the skew is positive, indicating that the probability densities have larger separation distances, with the greatest skewness occurring in the transitional region at x/d = 10. The skewness then decreases again as the incoming boundary layer continues to evolve to fully turbulent.

Towards the onset of transition and with a fully turbulent interaction, the kurtosis was small with values between 3-4 at the start of transition and 3.5 for the fully turbulent case. The kurtosis peaked at 7 at x/d = 10, the same location with the greatest skew. This relatively high kurtosis indicates that there were either the occasional outlier from the

mean, or the separation shock was unsteady within a larger region than the standard deviation implied. For the majority of the transitional interaction positions, the unsteadiness in the shock location has a greater number of extreme values than for the fully turbulent interaction case.

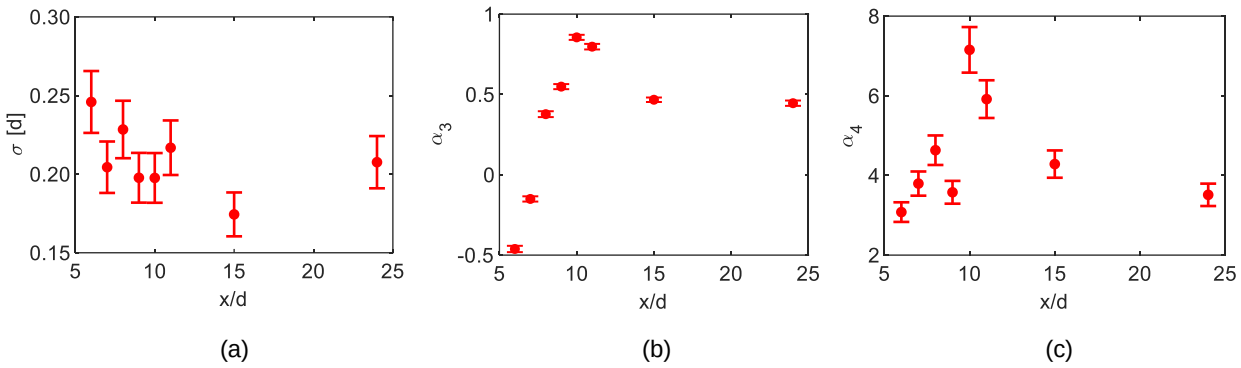

Figure 3.4. Statistical moments for the separation shock foot motion for varying blunt fin locations: (a) standard deviation, (b) skewness, and (c) kurtosis.

These same statistical moments for the *UI* shock are provided in Figure 3.5 for the blunt fin shock generator. In this figure, no data are provided for the *x/d* = 24 location. As the incoming boundary becomes more turbulent, the standard deviation increases from 0.33*d* to 0.98*d* for *x/d* = 6-15, meaning that the relative levels of *UI* shock unsteadiness increase.

The skewness values for the *UI* shock in Figure 3.5b are negative for the majority of the blunt fin locations. This once again indicates a left tail and implies that the shock tracking algorithm was tracking the location close to the separation shock position, with a few outliers upstream of the median position. The same shock generator positions that had the largest levels of skew also had the largest kurtosis levels as shown in Figure 3.5c. Even though the standard deviation increased with increasing blunt fin distance downstream from the flat plate leading edge, the number of outliers affecting the mean value decreased.

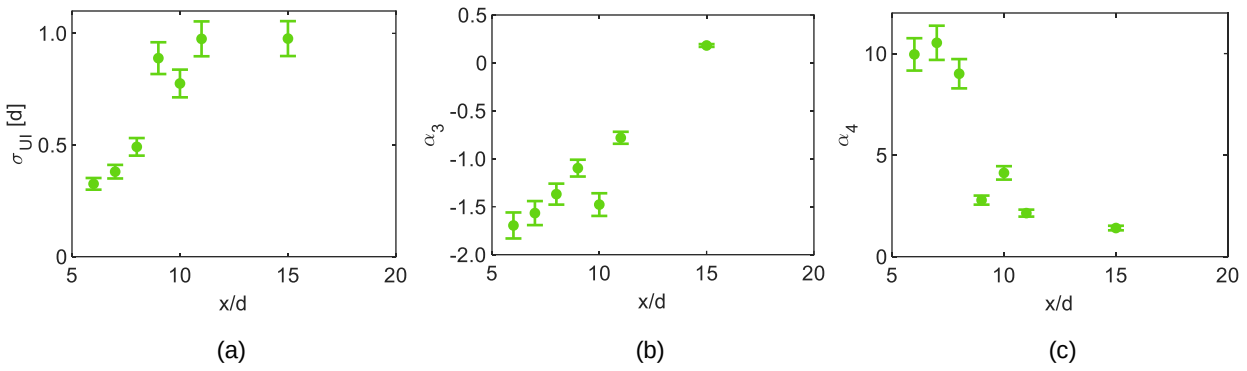

Figure 3.5. Statistical moments for the *UI* shock motion for varying blunt fin locations: (a) standard deviation, (b) skewness, (c) kurtosis.

As previously discussed, the *UI* shock is not present in fully turbulent boundary layers. This is again supported by the *UI* intermittency, γ_{UI}, for the blunt fin shock generator as shown in Figure 3.6. At shock generator positions closest to the flat plate leading edge, the *UI* shock was present nearly 80% of the time. As the incoming boundary layer evolved to fully turbulent, the intermittency of the *UI* shock decreases to 3.5%. It is this low value that motivates neglecting it in the statistical moments of Figure 3.5.

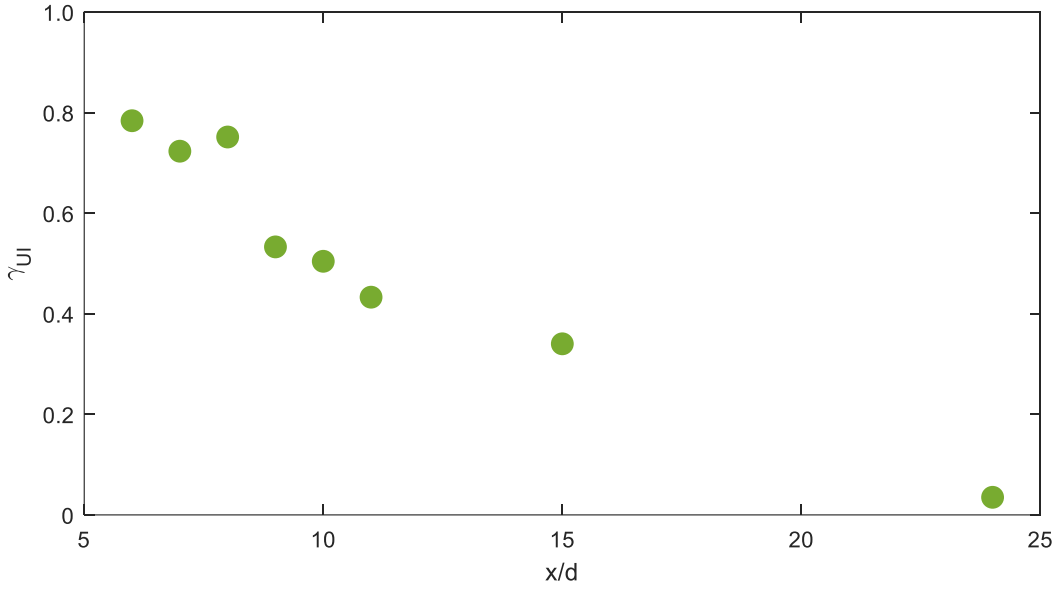

Figure 3.6. The upstream influence shock intermittency at various blunt fin positions.

In addition to the statistical data so far discussed, the unsteady motion of these shock waves may also be described through a spectral analysis. Using the normalized position of the shock features on the model surface, the non-dimensionalized power spectral density (PSD) may be plotted to better understand the frequency of shock wave oscillation. This is fundamentally a measure of the relative power a frequency has in the signal and has been historically applied to a pressure signal. Due to the inherently intermittent nature of the *UI* shock, spectra were not calculated for the feature.

Initially evaluating the same transitional and turbulent interaction cylinder positions of x/d = 7 (a) and x/d = 25 (b), respectively, the PSDs for both the separation and closure shocks are shown in Figure 3.7 for frequencies ranging from 0.1-50 kHz for the flat plate and vertical cylinder model. The spectral content of these data were computed using the MATALB *pwelch* command with an fft-size of 1,024 and a Hann window with 50% overlap. This results in an average of 49 Fourier transforms with a frequency resolution of 97.6 Hz. For the transitional interaction at x/d = 7 presented in Figure 3.7a, the high-intensity resonance for the separation shock is at 4,785 Hz, whereas a smaller intensity resonance for the closure shock is at 4,688 Hz, within the spectral resolution. This implies a correlation between the unsteady motion of the separation and closure shocks. Similar high-intensity resonances were not observed in the spectra for the turbulent interaction of Figure 3.7b, and are consistent with those reported for turbulent interactions from pressure data [31]. These results are also consistent with a review from Dussauge *et al*. [82] who found that the frequency of fluctuations produced by the shock motion are much lower than the characteristic frequencies of turbulent in the incoming boundary layer. Dussauge *et al*. [82] further theorized that the shock wave itself acts as a low-pass filter and thus will only respond to the low-frequency aspect of the excitation.

Since the separation shock PSD exhibited a narrow, high intensity frequency, the evolution of spectra for interactions at varying distances from the model leading edge were examined. The PSDs for the previously analyzed cylinder positions of x/d = 6, 7, 8, 9, 10, 11, 15, and 25 are presented below in Figure 3.8. In (a) is the full range of the signal, whereas (b) is a magnification of the 2 kHz – 9 kHz frequency range.

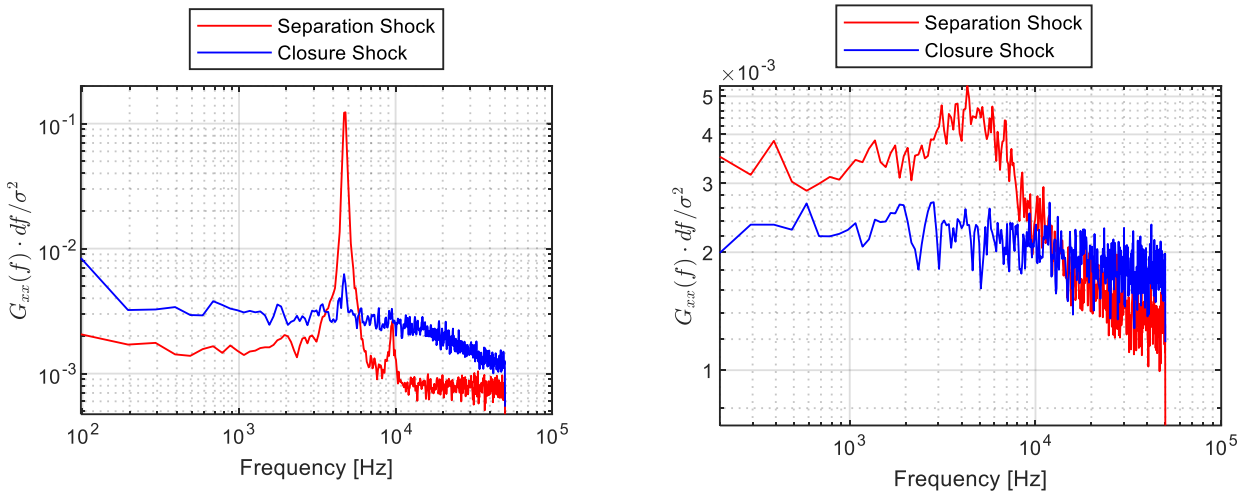

Figure 3.7. Power spectral density of the dynamics of the separation and closure shock waves for a transitional interaction (a) at *x/d* = 7 and a turbulent interaction (b) at *x/d* = 25 for a vertical cylinder shock generator.

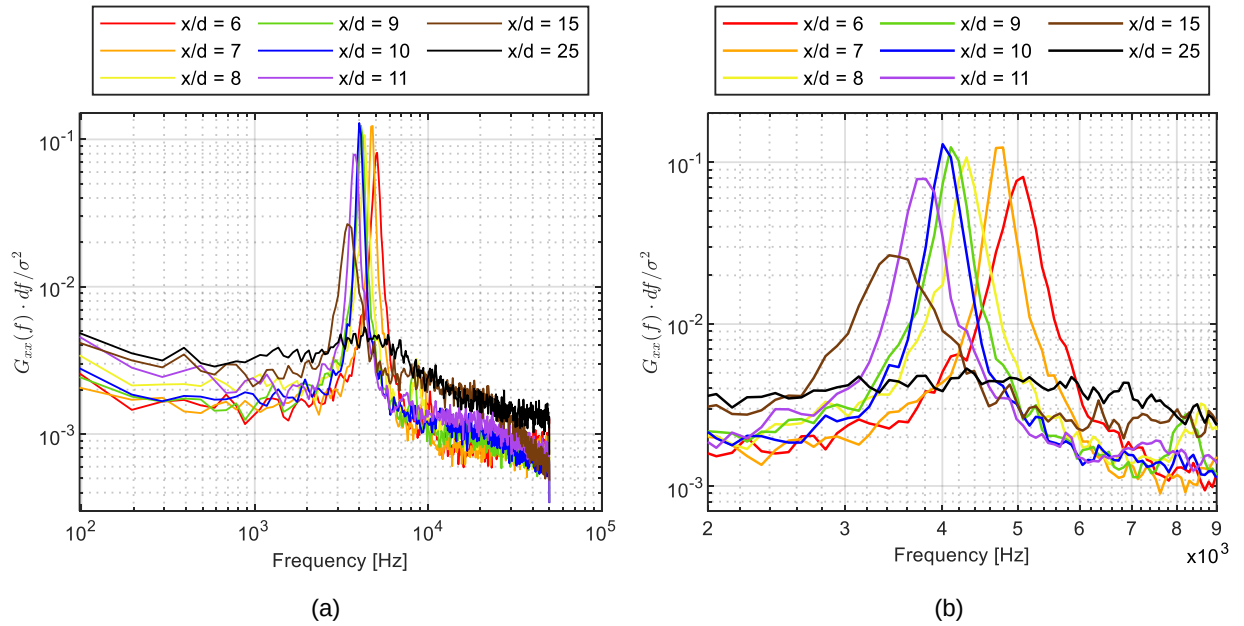

Figure 3.8. Power spectral density functions of the separation shock at various cylinder locations with (a) the complete spectral range and (b) a magnification of 2 – 9 kHz to better visualize the high-intensity resonance.

In this figure, the majority of the spectral content is contained within a mid-frequency range of between 1 – 10 kHz, even for the fully turbulent interaction case at *x/d* = 25. These high-intensity resonant frequencies are only present for cylinder positions *x/d* = 6 – 15. A plot of the frequency at these resonance values is provided for each cylinder position in Figure 3.9. The uncertainty in Figure 3.9 is representative of ± 2 *df*. As the incoming boundary layer evolves to fully turbulent, there is a decrease in the frequency of oscillation of the separation shock. The relative power this high-intensity resonance contributes also decreases, as observed from Figure 3.8b. The increase in frequency for the fully turbulent interaction at *x/d* = 25 is representative of a local maximum. The general trend for the separation shock in turbulent interactions is of broadband noise, as can be better observed in Figure 3.8a. This is most-likely due to the contributions of the high-frequency turbulent content within the boundary layer.

This frequency content may be non-dimensionalized by calculating the Strouhal number (*St*): a way to describe oscillations that include a characteristic length and the velocity of the fluid. The Strouhal number for the separation shock wave motion described above can be defined by equation 3.1. In this equation, *f* is the high-intensity resonance frequency from Figure 3.9 (as derived from Figure 3.8); the characteristic length is described as the average size of the separation bubble, λ_1-λ_2; and U_e is the boundary layer edge velocity (473 m/s).

$$St = \frac{f * (\lambda_1 - \lambda_2)}{U_e} \tag{3.1}$$

The Strouhal number is then multiplied by the square root of *x*, the location of the shock generator from the leading edge of the flat plate, in inches. In this way, the scaling of the Strouhal number accounts for not only the unsteady behavior of the interaction region, but also accounts for the expected growth scale of an incoming laminar boundary in the streamwise direction. A plot of how the Strouhal number varies with the evolving incoming boundary layer is presented in Figure 3.10.

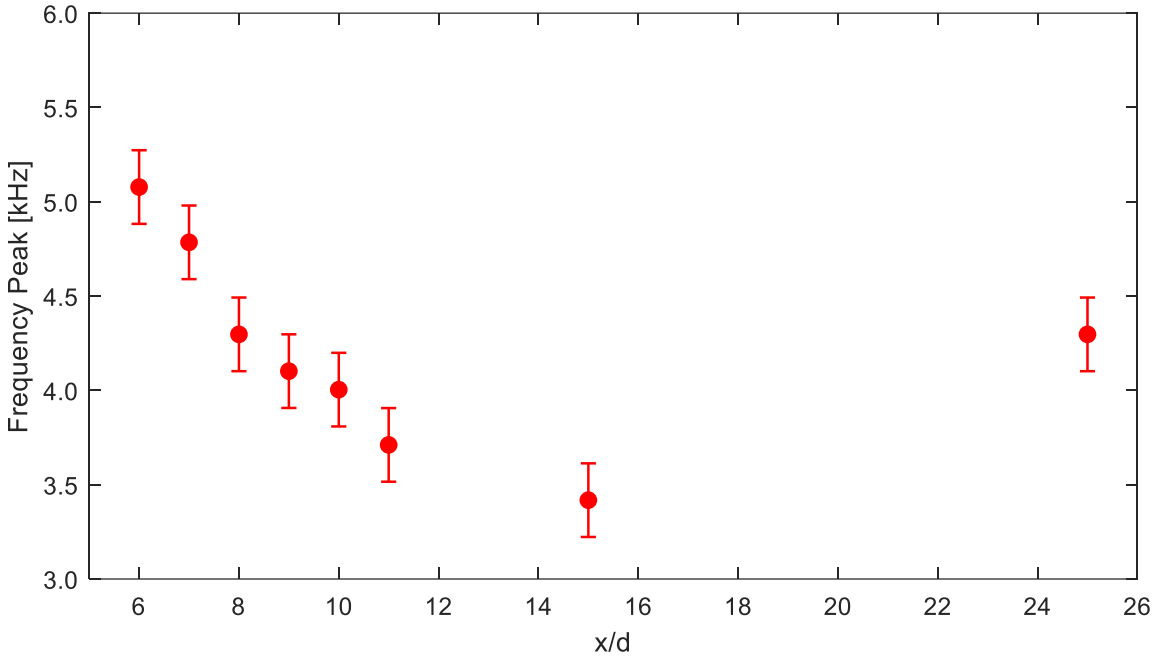

Figure 3.9. High-intensity frequency resonances for the separation shock at various vertical cylinder locations as taken from the PSDs presented in Figure 3.8. Error bars are representative of ± 2 *df*.

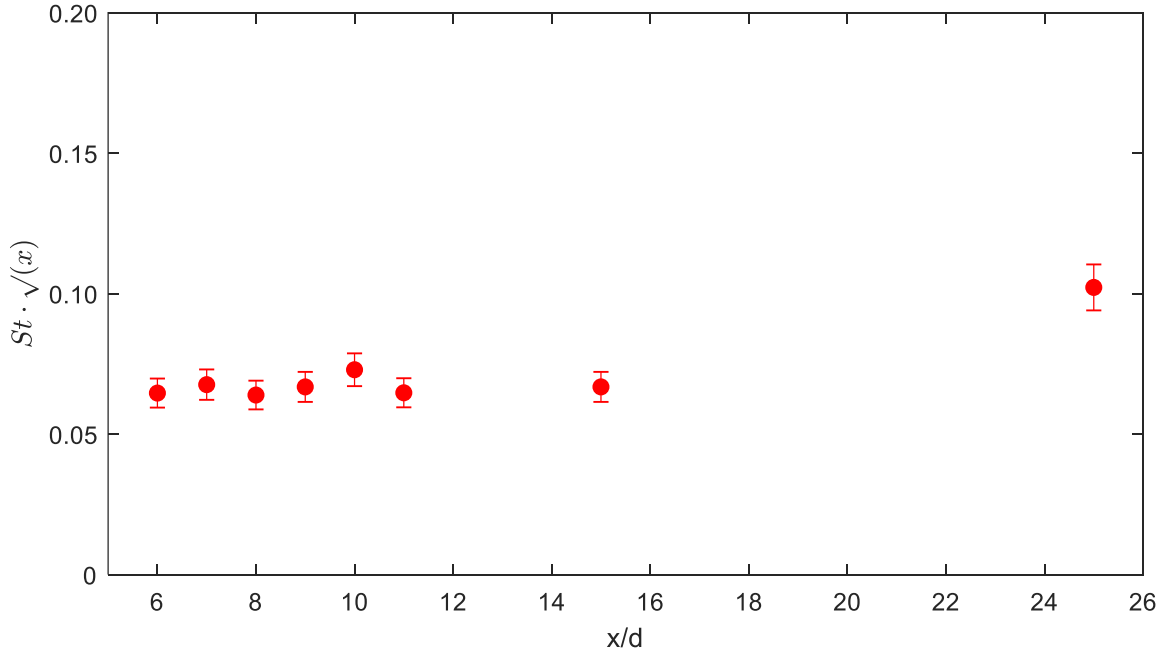

Figure 3.10. Strouhal number based on high-intensity frequency of separation shock motion for various cylinder positions.

The range of Strouhal numbers remains between 0.06 – 0.07 for transitional interactions, which is consistent with the findings of Erengil and Dolling [83] and Clemens and Narayanaswamy [84] who found that the Strouhal number remained relatively constant around 0.0225 for blunt fins, sharp fins, and ramps as shock generators for a variety of sweep angles.

The normalized power spectral density (PSD) distributions of the shock features as derived from the shock tracker are presented for the blunt fin shock generator for a transitional interaction case at *x/d* = 7 and a turbulent interaction case at *x/d* = 24 in Figure 3.11. The spectral content of these data were computed using the MATALB *pwelch* command with an fft-size of 1,024 and a Hann window with 50% overlap. For the image sampling rate of 200 kHz, this results in an average of 98 Fourier transforms with a frequency resolution of 195 Hz. The high intensity resonances for both shock waves in the transitional interaction of Figure 3.11a have frequencies of 5,078 Hz, implying a similar correlation between the two as observed for the interaction with the cylinder shock generator. No such correlation is apparent for the fully turbulent interaction in Figure 3.11b, and neither are high-intensity resonances observed in either shock wave motion. However, a local maximum for the separation shock has a frequency of 6,445 Hz.

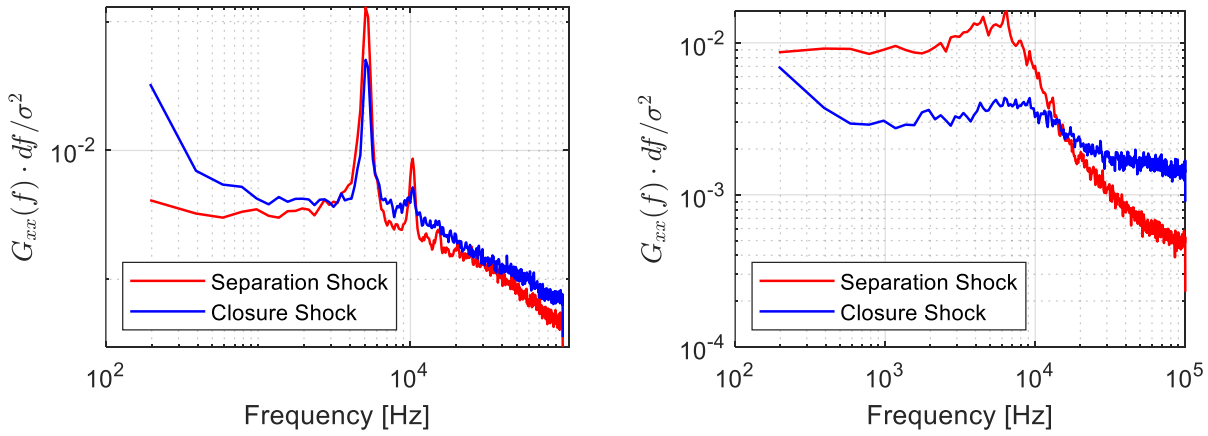

Figure 3.11. Power spectral density of the dynamics of the separation and closure shock waves for a transitional interaction (a) at *x/d* = 7 and a turbulent interaction (b) at *x/d* = 24 for a blunt fin shock generator.

The blunt fin positions presented below are consistent with the locations used in the previous statistical analysis: *x/d* = 6, 7, 8, 9, 10. 11. 15, and 24. In Figure 3.12a, the relative concentration of the high-intensity resonance stays between 1 kHz and 10 kHz, previously discussed as a mid-frequency range. There's a gradual roll-off in PSD intensity after *f* > 10 kHz, meaning there's little relative contribution of high frequency content. In the magnified image of Figure 3.12b, there's a shift in the resonance of decreasing frequencies until the fully turbulent broad band noise is achieved at *x/d* = 24, when the turbulent eddies fully dampen out the separation shock motion.

The Strouhal number for the high-intensity resonance from Figure 3.12b are shown in Figure 3.13. There is a consistent trend as the incoming boundary layer evolves, and then an increase for a fully turbulent interaction that is consistent with other shock wave/boundary layer interactions [83],[84]. The fully turbulent case at *x/d* = 24 has the highest Strouhal number of 0.128, and the smallest Strouhal number is 0.053 at *x/d* = 9. Strouhal numbers associated with the separation shock wave are typically around 0.0225 [84].

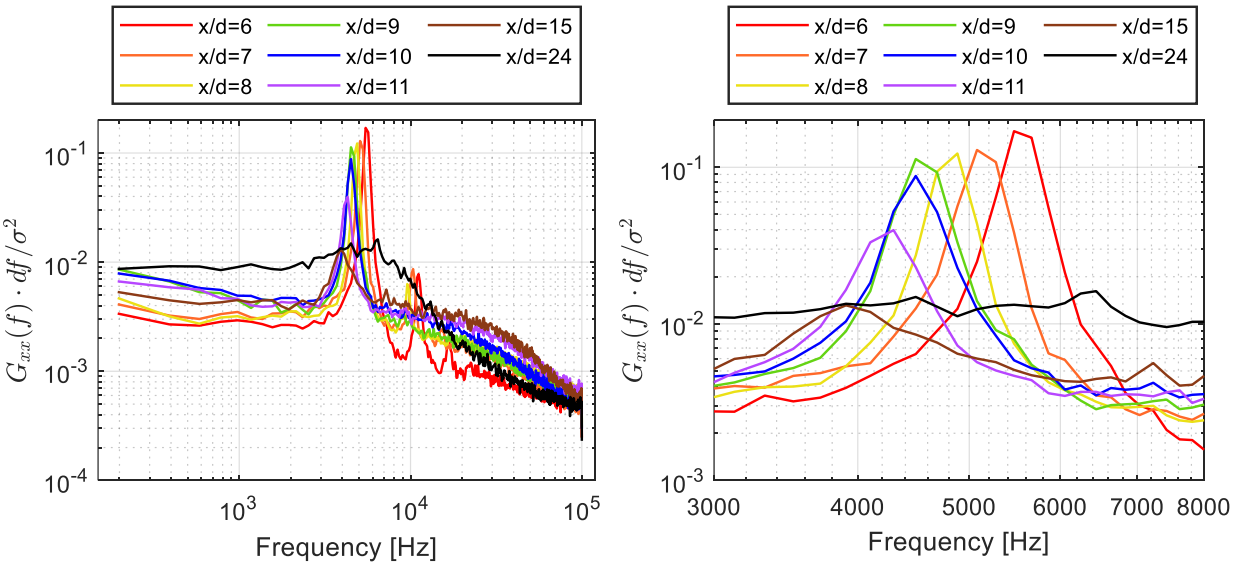

Figure 3.12. Power spectral density functions of the separation shock at various blunt fin locations with (a) the complete spectral range and (b) a magnification of 3 kHz – 8 kHz to better visualize the high-intensity resonance.

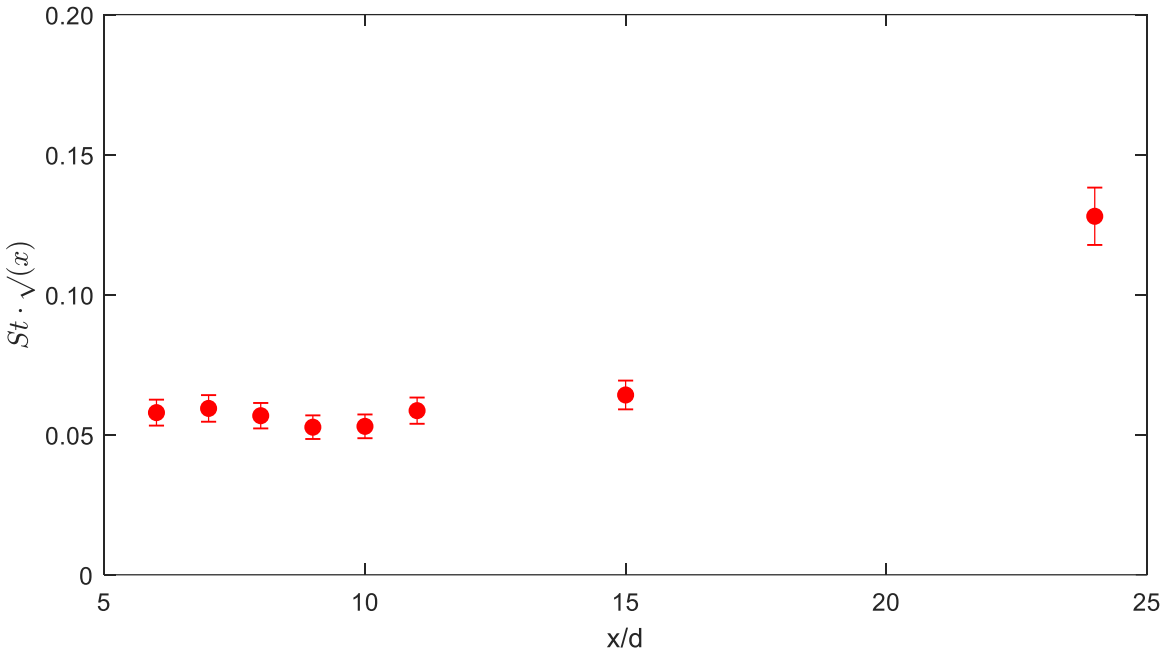

Figure 3.13. Strouhal number based on high-intensity frequency of separation shock motion for various blunt fin positions.

Although identical results were not observed for the blunt fin shock generator, similar unsteady motion of the separation shock and trends in the statistics of the three shock features were observed. A more comprehensive comparison between the vertical cylinder and blunt fin shock generators is discussed in Section 3.2.

3.2 Blunt Fin and Vertical Cylinder Shock Generator Comparisons

The original intent of generating the shock waves with a blunt fin model was to determine what, if any, effect the wake of the vertical cylinder had on the flowfield dynamics. With that in mind, the statistical and spectral results from the vertical cylinder and blunt fin analyses of the previous section are compared to each other here. Figure 3.14 shows the mean shock locations for the two shock generators; filled in circles are for the cylinder and open circles are for the blunt fin. Recall that there were some small differences in the data collection between the vertical cylinder and blunt fin shock

generators, primarily that the cylinder data was acquired at 100 kHz and the blunt fin data at 200 kHz. In order to compensate, however, the same length of time was analyzed between the two shock generators. The closure shock marker size approximately represents the error associated with the mean position, and has relatively good agreement between the two shock generators with about 0.2*d* difference (note this is within the uncertainty of the shock tracking algorithm).

The overall trend of each of the three shock features remains consistent, with the greatest difference occurring towards the end of transition for the *UI* shock for *x/d* = 9-15 where the scaling distance continued to increase for the cylinder model. At *x/d* = 15, the difference in the mean positions of the *UI* shock is 1.8*d*. The divergence in the *UI* shock around *x/d* = 10 could be a factor of the intermittency as γ_{UI} is approximately 50% for both shock generators at this location (see Figure 3.15). The greatest difference in the separation shock mean is at *x/d* = 10 with a difference of 0.65*d*. The similarity in the mean positions of the *UI* and separation shock at *x/d* = 6 and 7 is the result of a compression effect near the flat plate leading edge, which results in the increase in shock wave scaling with an incoming transitional boundary layer until a fully turbulent interaction is achieved [75]. From the literature (Figure 1.9 [13]), the scaling of the interaction structure is expected to decrease as the incoming boundary layer evolves to a fully turbulent state. Although traditionally reported based on the separation shock or boundary layer separation point, the *UI* shock in Figure 3.14 exhibits the same decrease in scaling discussed in the literature that results with the breakdown to turbulent eddies in the boundary layer resisting boundary layer separation. The separation and closure shock mean position for both shock generators with fully turbulent interactions (*x/d* = 24 and 25) are within the margin of error of each other. From Figure 3.14, it appears that the interaction between the two shock generators are qualitatively the same for both transitional and turbulent interactions.

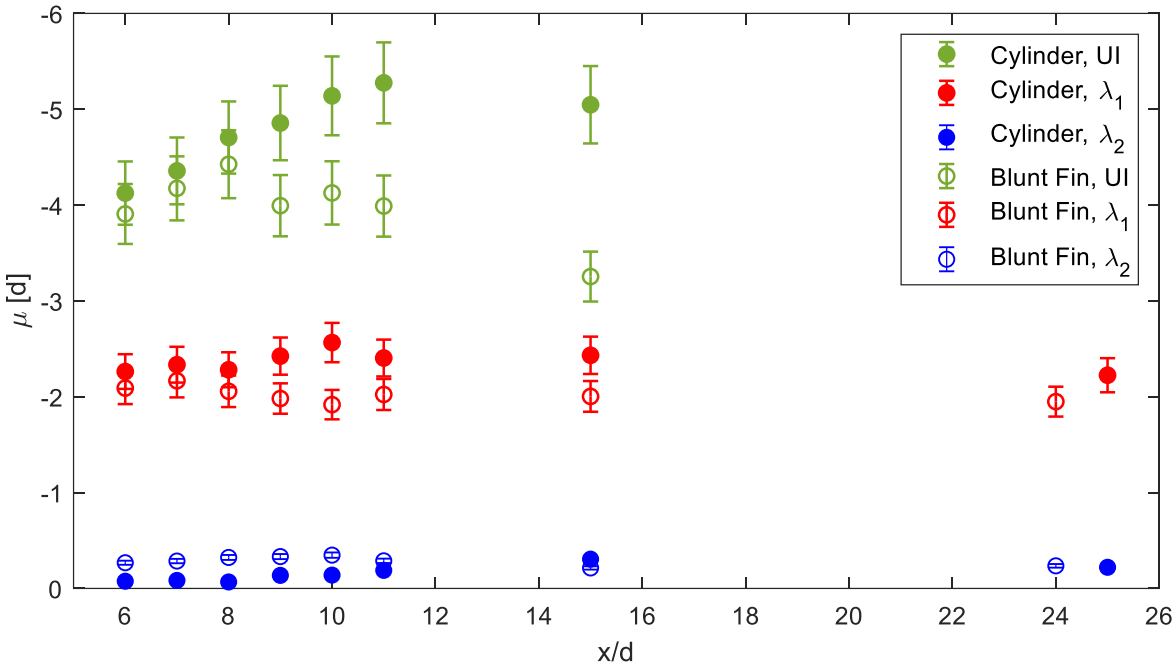

Figure 3.14. Comparison of the mean shock locations for the blunt fin and vertical cylinder shock generators.

The *UI* shock intermittency, γ_{UI}, for both shock generators is presented in Figure 3.15 with the filled in circles for the cylinder and the open circles for the blunt fin. Despite the deviation of mean *UI* shock locations between the two shock generators shown in the previous figure, the *UI* intermittency values are similar to each other with the greatest deviation at *x/d* = 7 with the cylinder at 0.83 and the blunt fin at 0.72. The other values are within the uncertainty levels with clusters around 0.8, 0.5, to near zero for the fully turbulent interactions at *x/d* = 24 and 25. The gradual decrease in the *UI* shock intermittency is consistent with previously observed trends for transitional boundary layer interactions, and there is a negligible difference in the intermittency of this feature between the two shock generators.

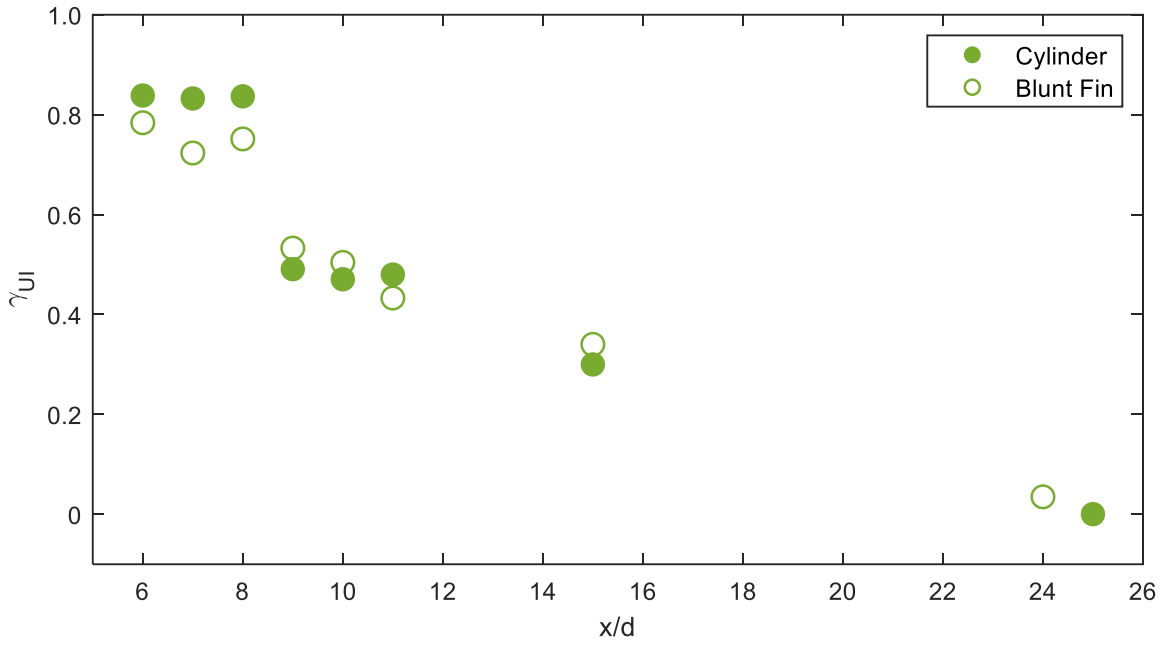

Figure 3.15. Comparison of the *UI* shock intermittency for the vertical cylinder and blunt fin shock generators at various locations on the flat plate model.

It was previously observed that the frequency of oscillation and corresponding Strouhal number for the blunt fin separation shock was slightly higher than the vertical cylinder. Because the blunt fin schlieren images were acquired at 200 kHz and the cylinder images at 100 kHz, care needs to be taken prior to comparing the normalized PSDs between the two shock generators. Initially, the PSDs for a transitional interaction (x/d = 7) for the blunt fin shock generator are compared with the original data and by down sampling data with no other changes to the data processing method are evaluated. In the figure below, the FFT-size is still 1,024 with a Hann window with 50% overlap. The only difference for this initial comparison is that the PSDs are not normalized by dividing by the variance, only multiplied by the respective frequency resolution of each data set. Figure 3.16 presents this comparison for the total frequency range. The high-intensity resonance match at St = 0.03 and the slight offset in the PSD magnitude is an expected result of the differing frequency resolutions between the two functions.

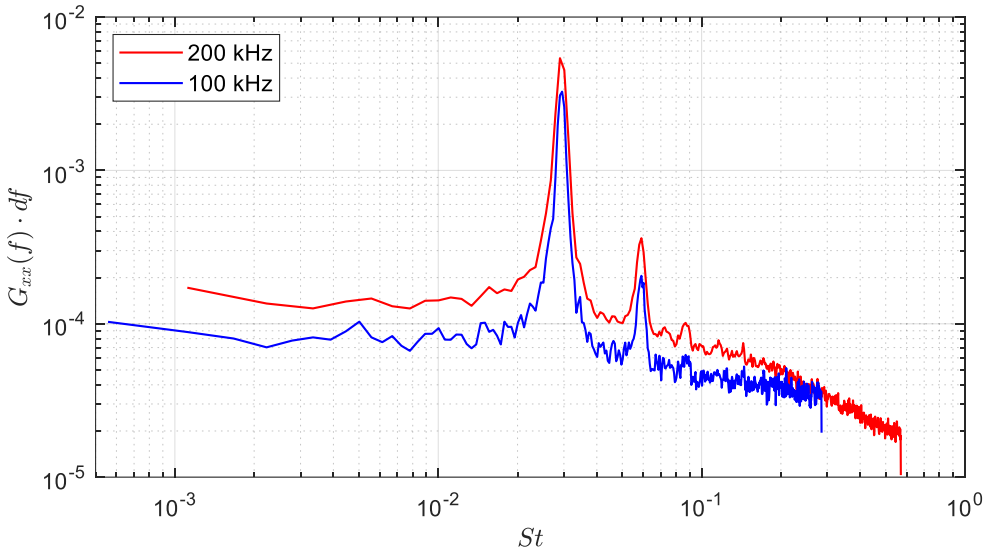

Figure 3.16. Separation shock PSD for the blunt fin shock generator located at *x/d* = 7 comparing the original 200 kHz acquisition data and the down sampled 100 kHz.

The PSDs for the blunt fin shock generator at different frame rates demonstrated good agreement with one another, so all subsequent blunt fin spectra are down sampled to 100 kHz to better compare to the vertical cylinder data. Comparison of PSDs for shock generator locations at increasing distances downstream of the plate leading edge clearly exhibit a shift in the resonance frequency oscillation as the incoming boundary layer evolves. Spectra of this behavior comparing the vertical cylinder model to the blunt fin model is presented in Figure 3.17 for three transitional interaction locations. Figure 3.17b is a magnification of the high-intensity resonance. For each shock generator, there is a decrease in resonance frequency as the incoming boundary layer grows with the cylinder resonance ranging from *f* = 4.3 kHz – 5 kHz and the blunt fin between *St* = 4.9 kHz - 5.5 kHz. All six PSDs also show a secondary resonance at approximately 10 kHz; it is currently hypothesized that this is a harmonic and not a real feature of the shock motion and future tests using focused laser differential interferometry (FLDI) will potentially verify this assumption [27]. Figure 3.17 also shows a shift between shock generators in the PSD resonance with cylinder interactions having slightly lower frequency content than the blunt

fin interactions. This is considered to be a negligible difference between the two models as the resonances occur in the same frequency range and exhibit the same pattern.

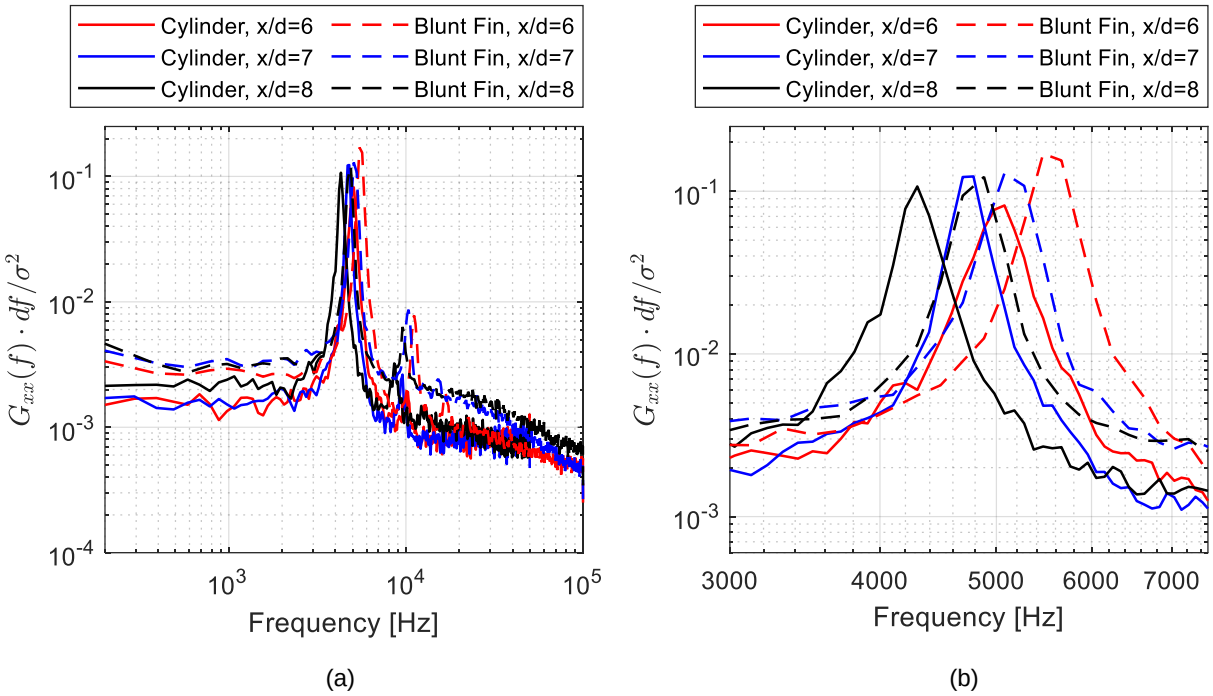

Figure 3.17. Normalized PSD comparing three positions of the vertical cylinder and blunt fin shock generators with matching data acquisition rates. (a) full spectral range and (b) high-intensity resonance magnification.

In addition to the three transitional interaction spectra, the PSD for the fully turbulent interaction cases are shown in Figure 3.18 at *x/d* = 25 for the cylinder and *x/d* = 24 for the blunt fin. The broad-band signal content generally agrees between the two cases, with a slightly increased roll off of the higher-frequency content for the blunt fin interaction. Neither spectrum reveals an high-intensity resonance with local maxima in the mid-frequency range of *St* = 0.01-0.1, which is consistent with power spectra based on dynamic pressure measurements reported in the literature [85].

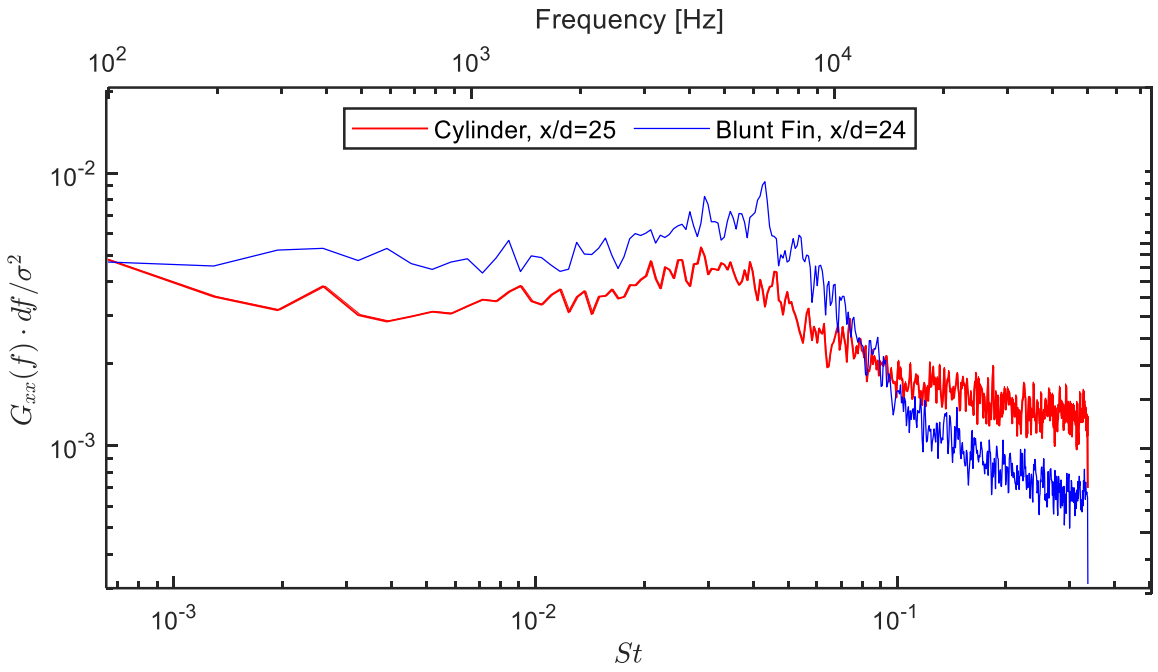

Figure 3.18. Normalized PSD comparing the vertical cylinder and blunt fin shock generators with a fully turbulent incoming boundary layer.

Based on the statistical and spectral content presented herein, it appears that the wake generated from the vertical cylinder model does not have an impact on the interaction dynamics, because similar unsteady behavior for both incoming transitional and turbulent boundary layers was observed. When performing this analysis, the trends with the evolving boundary layer need to be the focus as opposed to the precision of the high-intensity spectral resonance values; for instance, the difference between the cylinder and blunt fin spectral resonance at *x/d* = 6 is only approximately 0.004. Considering that the same trends are observed for both shock generators, this is indicative that there is no impact from the wake of the models.

3.3 Boundary Layer Separation Precursor Correlation

One of the other interesting features observed in the time-resolved schlieren images of Figure 2.10 for the blunt fin model was an abrupt thickening of the boundary

layer in the region between the *UI* shock and separation shocks. Because the same interaction dynamics were observed for both the cylinder and blunt fin shock generators, only the blunt fin-generated results are the focus of this section. This boundary layer thickening feature appears highly correlated to the *UI* shock position in transitional interactions, and cannot be distinguished in turbulent interactions due to its proximity to the separation bubble upstream of the closure shock. As discussed in Section 2.1.4, the optical configuration for the blunt fin shock generator experiments was improved from those conducted with the vertical cylinder. Improved visualization over that of the previous configuration was achieved. For clarity, an instantaneous schlieren image from a transitional interaction generated by a blunt fin at *x/d* = 7 is provided in Figure 3.19 with the boundary layer separation precursor feature identified.

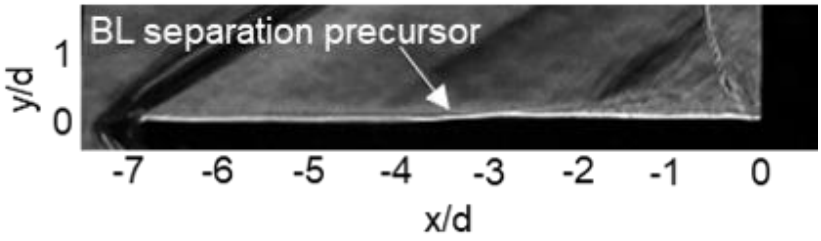

Figure 3.19. Instantaneous schlieren image of a transitional interaction generated by a blunt fin at *x/d* = 7 taken from Figure 2.10 with the boundary layer (BL) separation precursor feature identified just downstream of the *UI* shock. Flow is from left to right.

A thickening of the boundary layer is not necessarily indicative of boundary layer separation, however. This could be an indicator that the boundary layer is about to separate. Recent computational simulations by Tester *et al.* [86] of prior vertical cylinder transitional interactions performed at UTSI [75] identified a similar relationship between the boundary layer thickening and the *UI* shock to that observed in the blunt fin experiments. They used OVERFLOW 2.2, a NASA three-dimensional time-marching implicit RANS compressible gas dynamics solver to model a vertical cylinder at *x/d* = 7 with two different turbulence models: the first was the Spalart-Allmaras (SA) eddy-

viscosity turbulence model to generate a turbulent interaction, and the second used the amplification factor transport (AFT) transition model coupled with the SA turbulence model to simulate a transitional interaction [86]. They were able to show that near the wall region, reverse flow in the boundary layer extended farther in transitional interactions compared to turbulent interactions. The SA-AFT transition/turbulence model captured the corresponding weakening of the separation shock when the *UI* shock is present, which was qualitatively observed in the schlieren image sequences of Figure 2.9 and Figure 2.10. Tester *et al*. attributed this to both the more gradual separation process and the more gradual deceleration of the supersonic flow in transitional interactions compared to turbulent interactions [86]. In addition, the surface skin-friction distribution showed an inflection towards separation that coincides with the *UI* shock [87]. From integral boundary layer relations, the combination of decreasing skin-friction and increasing pressure is indicative of an increased boundary layer growth rate. Tester *et al.* [86] attributed the formation of the *UI* shock and the gradual increase in boundary layer thickness upstream of the separation shock to a viscous-inviscid interaction that is elliptical in character. They did not conclude what the origin of the *UI* shock was, but observed that it strengthens as the boundary layer thickness increases and weakens the separation shock [86].

More recent simulations using OVERFLOW 2.3 with the same SA-AFT transition/turbulence model were also able to capture this upstream behavior in transitional interactions. The unpublished results from these simulations were provided courtesy of Dr. James Coder from The University of Tennessee, Knoxville. The density gradient at the centerline for a transitional and turbulent interaction are provided in Figure 3.20. In the transitional interaction (left) both the *UI* shock and the boundary layer separation precursor are evident upstream of the separation shock, λ_1. The mean separation shock location for the transitional interaction is -2.9*d* and for the turbulent interaction, -2.6*d*. The boundary layer separation precursor is approximately -3.6*d* upstream of the vertical cylinder face and appears to initiate at the *UI* shock.

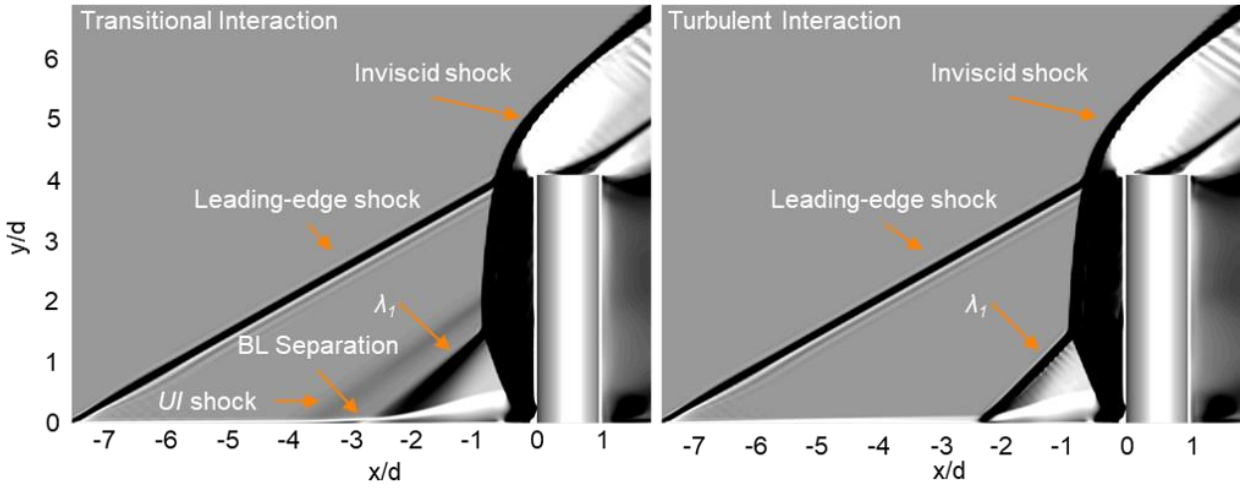

Figure 3.20. Density gradient magnitude contour along the centerline for a transitional interaction (left) and a turbulent interaction (right). The cylinder is located at *x/d* = 7. [Unpublished simulations courtesy of J. Coder, UTK]

The primary reason for calling this boundary layer feature upstream of the separation shock a “separation precursor” is based on these simulated results. In Figure 3.21a, the normalized wall pressure for a transitional interaction shows a gradual increase upstream of the boundary layer separation point for a turbulent interaction, although the magnitude of the pressure in the separation bubble is almost the same magnitude between the two interactions. The skin friction in Figure 3.21b shows that the boundary layer separates in the transitional interaction -3.4*d* upstream, just a little farther downstream from the initial pressure rise at -4*d*. This value approximately matches that of the observed onset of the boundary layer separation precursor from the density gradient in Figure 3.20. The fully turbulent interaction does not separate until approximately -2.3*d*, again just a little farther downstream from the initial pressure rise at -2.5*d*.

For completeness, the velocity profiles for three locations along the centerline upstream of the cylinder for a transitional interaction are provided in Figure 3.22. These profiles show that the boundary layer separates between -3.5*d* and -3*d*, as also shown in Figure 3.21, which is still upstream of the mean position of the separation shock (-2.9*d*).

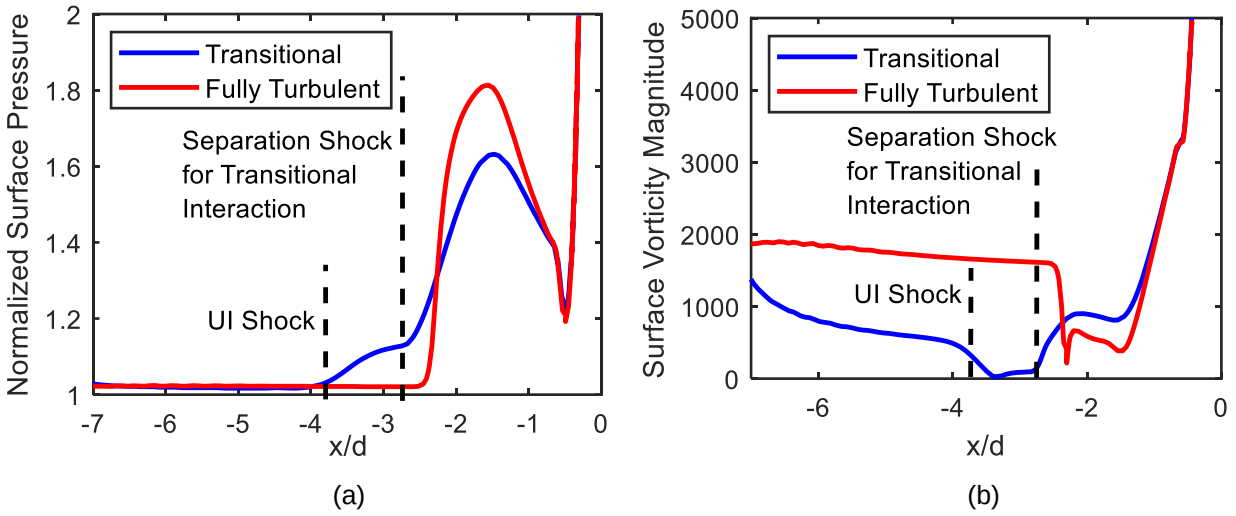

Figure 3.21. Centerline characteristics of transitional and turbulent interactions upstream of the shock generator from RANS simulations. (a) normalized wall pressure. (b) skin friction. [Unpublished simulations courtesy of J. Coder, UTK]

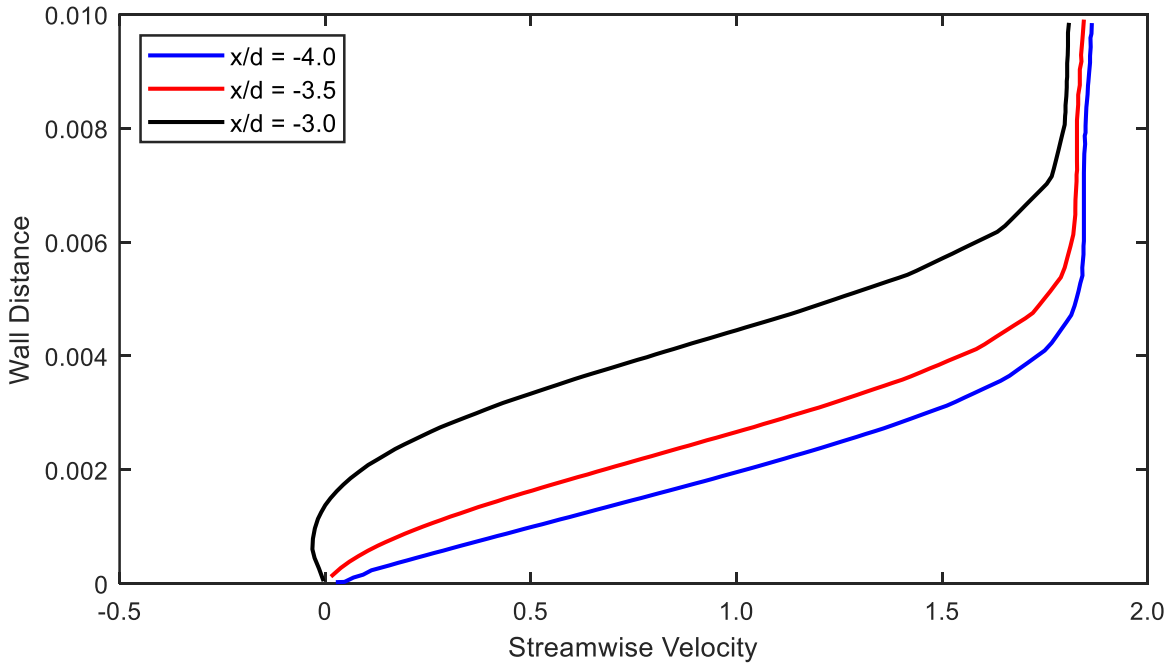

Figure 3.22. Velocity profiles for three locations on the centerline upstream of the vertical cylinder for a transitional interaction. [Unpublished simulations courtesy of J. Coder, UTK]

The combination of these computational results provide evidence that the boundary layer is separating upstream of the separation shock for transitional interactions under these flow conditions. This conclusion is then applied to the experimental results discussed subsequently as the unsteady motion of the boundary layer separation precursor is evaluated and compared to the unsteady motion of the shock waves.

In order to determine if the thickening of the boundary layer in the schlieren images are, in fact, correlated with any of the shock wave features of the interaction, a transitional interaction generated by a blunt fin at x/d = 7 was examined. A sample temporal response of how this boundary layer feature compares to the unsteady positions of the shock waves is provided in Figure 3.23. The position of the *UI* shock, separation shock, λ_1, and boundary layer (BL) separation all appear to have a sinusoidal shape with the *UI* shock disappearing during the deflationary stage of the interaction dynamics. However, even when the *UI* shock is not present, the position of the BL separation remains upstream of the separation shock position. Also, the motion of the *UI* shock emanating from the separation shock is evident. This sample temporal response appears to show a strong relation in the relative positions of these features. The closure shock, λ_2, shows very little unsteadiness with little correlation to any other flow features.

The probability density functions (PDF) for the *UI* shock, separation shock, and boundary layer (BL) separation precursor are shown in Figure 3.24. The mean position for the boundary layer separation precursor location is -3.24*d* with the unsteady position spanning both the separation shock and the *UI* shock positions. The standard deviation of the boundary layer separation is 0.58*d*. This mean location is almost precisely halfway between the mean positions of the *UI* shock at -4.2*d* and the separation shock at -2.2*d*. Overall, the trend of the boundary layer separation motion matches that of the *UI* shock with a long right tail. There is an increase in probability just before -4*d*, which is most likely a result of the peak in the PDF of the *UI* shock at -4.4*d*. The boundary layer separation right tail positions that overlap with the separation shock positions results from the intermittency of the *UI* shock; when the *UI* shock is not present, the boundary layer separation precursor tracks closer to the separation shock.

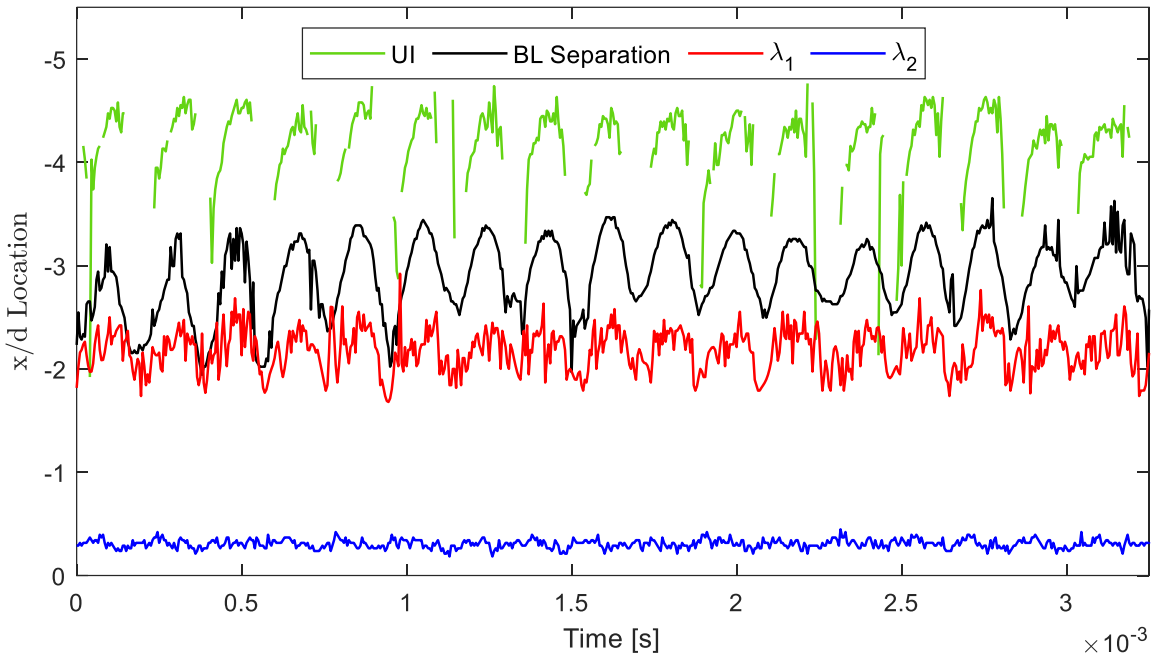

Figure 3.23. Temporal plot of the unsteady motion of the *UI* shock, boundary layer (BL) separation feature, separation shock, and closure shock for a blunt fin interaction at *x/d* = 7.

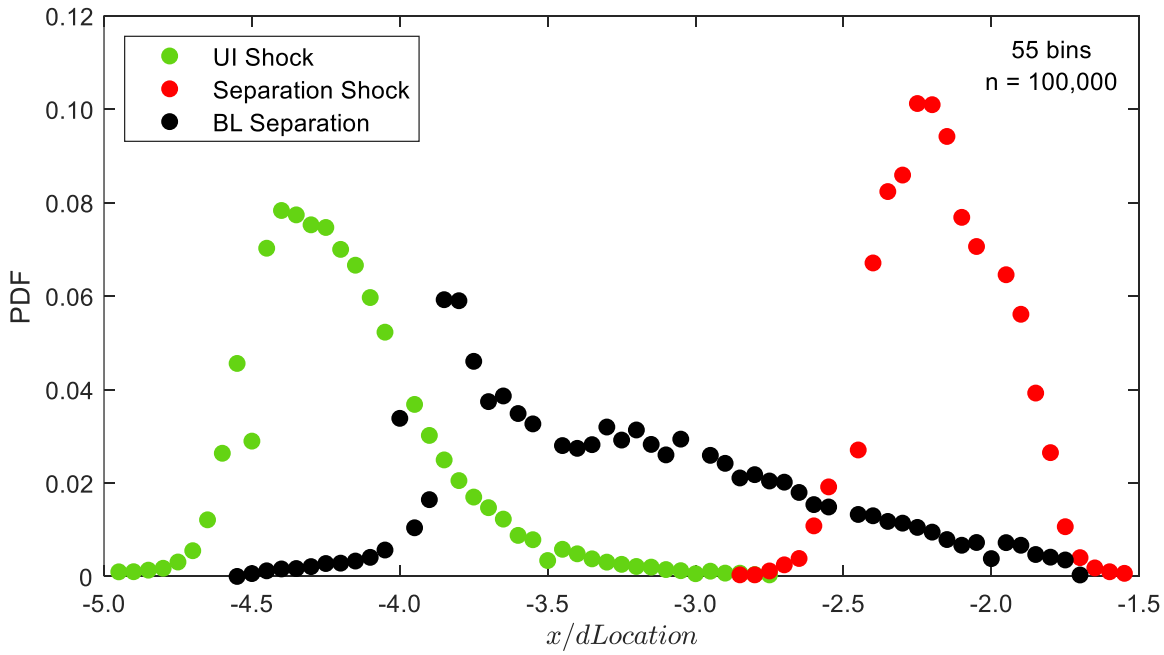

Figure 3.24. PDF for the *UI* shock, separation shock, and boundary layer separation location upstream of the blunt fin shock generator on the flat plate model at *x/d* = 7.

The PSD for this unsteady boundary layer separation location is shown in Figure 3.25. Just as with the separation shock spectra for transitional interactions, a high-intensity resonance exists in the mid-frequency range at f = 5.1 kHz (St = 0.029). This value matches that of the corresponding separation shock, also shown in Figure 3.25. However, even as the boundary layer separation location oscillates with the same characteristic frequency as the separation shock, that doesn't mean that the positions are correlated with each other. Qualitatively, from the schlieren image sequence shown in Figure 2.10, the boundary layer separation location appears to more closely track the *UI* shock position, not the separation shock position for a transitional interaction.

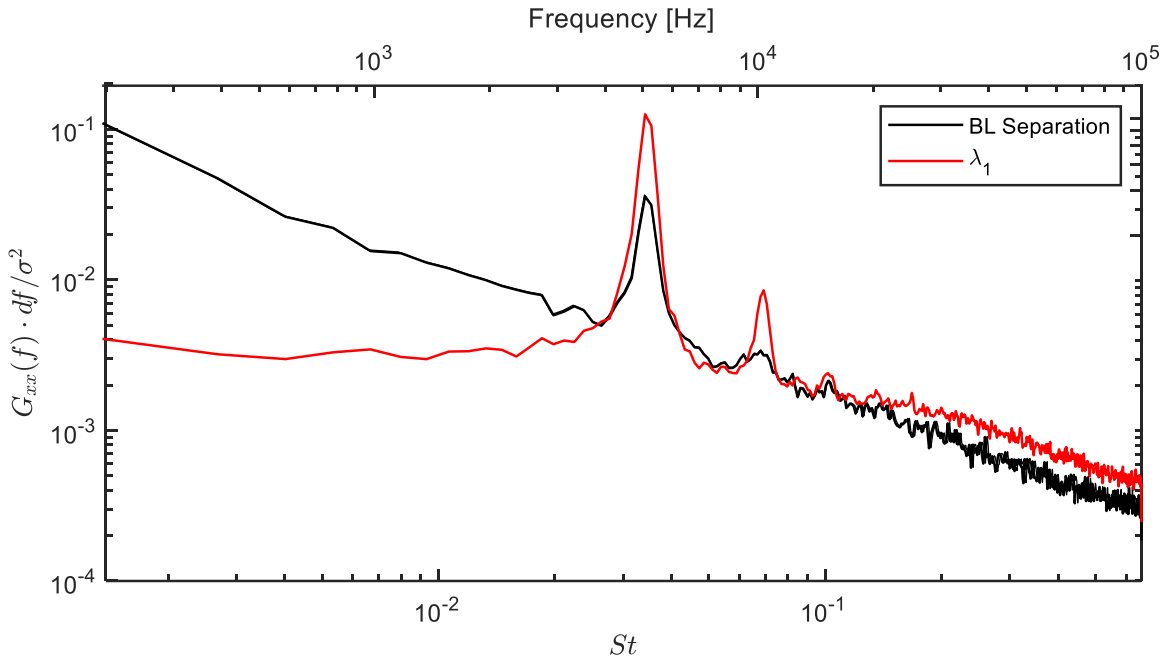

Figure 3.25. Normalized PSD of the boundary layer separation precursor location and separation shock from the flat plate and blunt fin model at x/d = 7.

In order to determine the legitimacy of this qualitative observation, cross-correlation functions between the shock waves and boundary layer separation position are provided in Figure 3.26. Five correlations are presented to better understand how the

boundary layer separation location correlates with the *UI* shock or separation shock for a transitional interaction generated by a blunt fin at *x/d* = 7. Because the *UI* shock is inherently an intermittent feature of the flowfield, the occasional absence of the *UI* shock needs to be resolved. The applied solution was to segment the *UI* shock data into records where the *UI* shock is present. Correlations for these records and the corresponding records in the separation shock, closure shock, and boundary layer separation data are then averaged together to form a mean correlation as plotted in Figure 3.26. This severely limits the number of data points that may be used within a correlation. Figure 3.26 represents an ensemble of 1,813 records of a minimum of 20 consecutive data points. The correlation functions were normalized by the product of the standard deviations between the two corresponding data sets. Dashed vertical and horizontal lines at zero lag and zero correlation are provided for reference.

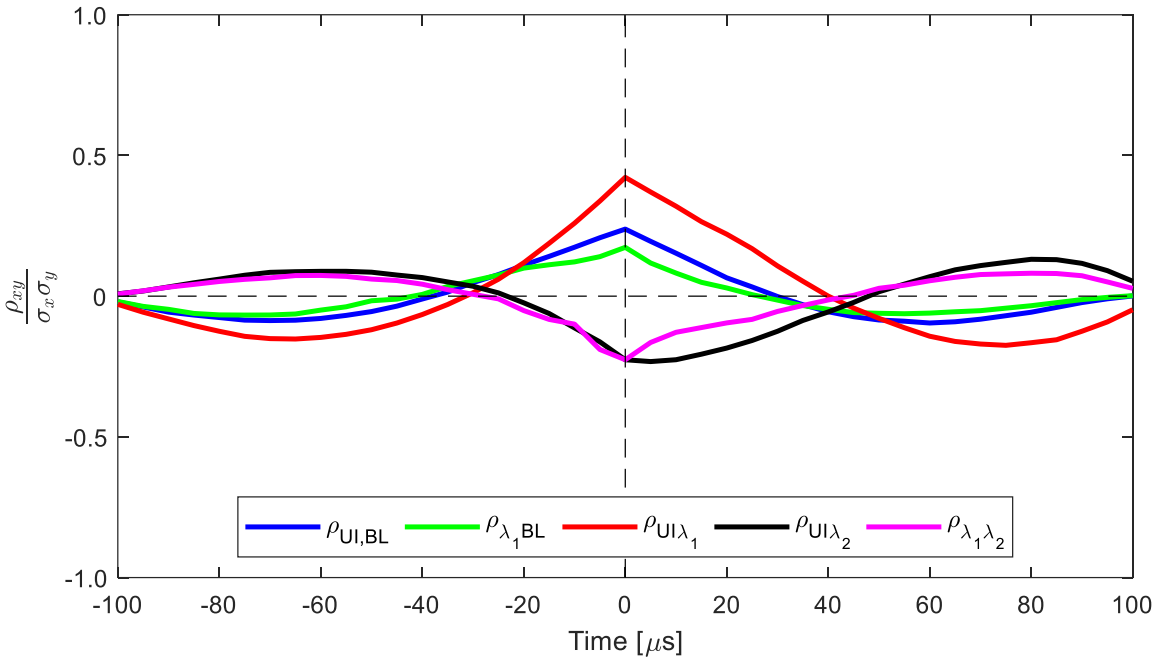

Figure 3.26. Cross-correlation functions of the shock structures and boundary layer separation location (BL) for the blunt fin and flat plate model for a transitional interaction at *x/d* = 7.

For this ensemble averaged data, none of the cross-correlations have a lag associated with it at the maximum correlation point. *UI*-λ_1 have the strongest correlation with a peak of 0.44. However, there are also two local minima of -0.1523 with a -65 μs lag and -0.1748 with a 75 μs, which means there could be a counter-motion relationship between the two features. The next strongest positively correlated relationship was between *UI*-BL with a peak of 0.2448. The λ_1-BL correlation is the least correlated with a positive peak of 0.1734 and no lag. Not only do the PSDs of the separation shock and boundary layer separation match, but the boundary layer separation position is correlated with both the *UI* shock position and the separation shock position, albeit slightly in this case. The features least correlated with each other are *UI*-λ_2 and λ_1-λ_2. The *UI* shock and closure shock have a correlation of -0.2325 at 5 μs and the separation and closure shocks have a correlation of -0.2423 with no lag. The 5 μs time lag represents the temporal resolution of the 200 kHz acquisition for this test case. It would be expected that the two correlations with the closure shock would have the largest time lags and least correlation owing to the region of subsonic flow upstream of the closure shock.

The convection velocities, ΔU, may be calculated from the correlations using the distance between the mean positions of the shock waves and boundary layer separation feature and the period. For the λ_1-BL correlation, the convective velocity is 130 m/s and for the *UI*-BL correlation, 190 m/s. This is to be expected as some of the highest convective velocities should exist between the *UI* shock and separation shock. Previous work has shown that convective velocities in this region are between 100-200 m/s and between 50-100 m/s for the separation and closure shocks with varying shock generator positions [88]. Based on the acquisition rate for this case, the fastest convective velocity the schlieren system can resolve is approximately 680 m/s.

Some of the individual correlations between the *UI*-BL phenomena showed higher levels of correlation, whereas others showed no correlation. To explore the impact of the more highly-correlated samples, a proper orthogonal decomposition (POD) of the *UI*-BL records for this test case was applied. The modal energy distribution for this interaction condition is shown in Figure 3.27a. The first three modes have the following energy levels: 67.3%, 17.7%, and 3.5% and are plotted in Figure 3.27b. The first mode has the

correlated shape, meaning that a majority (67.3%) of the records are correlated. Using the first two modes to reconstruct the correlation average across all records for the *UI*-BL correlation are then compared to the data average from Figure 3.26 and shown in Figure 3.27c. There is excellent agreement, meaning that the first two modes capture the dominant correlation relationship.

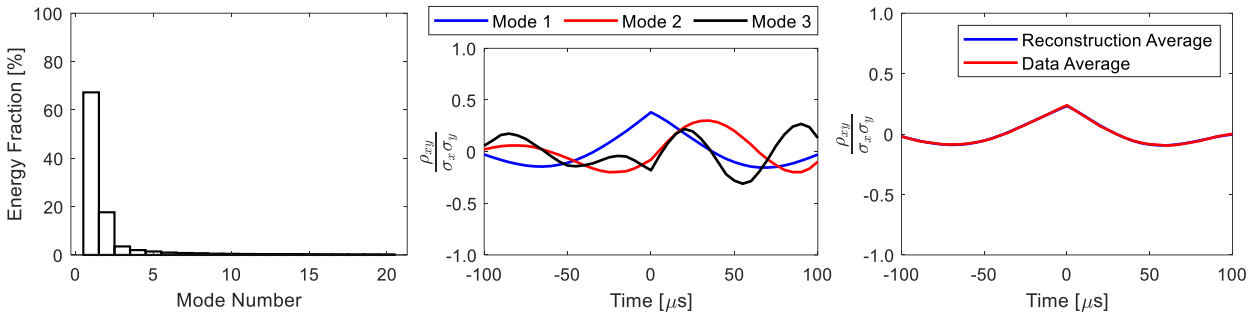

Figure 3.27. (a) *UI*-BL correlation modal energy from POD. (b) First three modes. (c) Reconstructed *UI*-BL correlation average for all records using the first two modes compared to the original data average from Figure 3.26. All data for the blunt fin and flat plate model for a transitional interaction at *x/d* = 7.

The first two modes were then used to look at individual records of the *UI*-BL correlation. Figure 3.28 shows three individual record samples comparing the raw correlation to the reconstructed correlation using the first two modes. Figure 3.28a is an in-phase record, (b) is an out of phase record, and (c) is an uncorrelated record. In each case, the reconstructed correlation approximately captures the raw correlated signal, except for where no correlation exists in (c). In-phase means that both features are moving in the same direction relative to their respective means. For the purposes of this analysis, only those records where an in-phase correlation exists between the *UI* shock and boundary layer separation feature will be considered. This additional threshold will allow for a better understanding of the influence the *UI* shock and boundary layer separation relationship have on the other flow features. As shown in Figure 3.28, applying an additional threshold to records with correlations greater than 0.35 produces this threshold constraint.

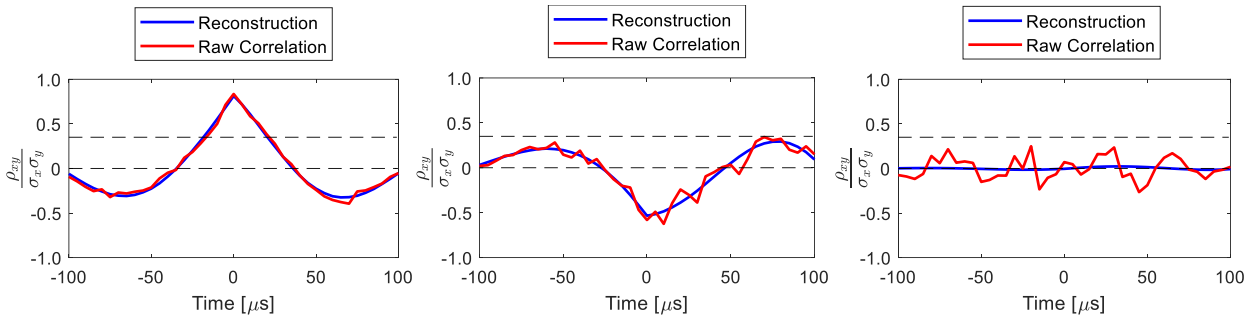

Figure 3.28. Individual record comparisons of the raw *UI*-BL correlation to the corresponding reconstruction using the first two modes from the POD analysis. (a) In-phase sample, (b) out of phase sample, (c) no correlation sample. Dashed lines at correlations of zero and 0.35 for reference.

The corresponding records for the cross-correlations of the other interaction features when taking the average across only those highly correlated *UI*-BL records are provided in Figure 3.29. As expected, the *UI*-BL correlation increases to 0.34, and the λ_1-BL correlation increases to 0.23 from the previous values in Figure 3.26. There is little change in the other correlation values. This means that even for specific records when the *UI*-BL correlation is high and in-phase, the correlated position between *UI*-λ_1 is still dominant at 0.44. Despite the similarity between the averaged correlations in Figure 3.26 and Figure 3.29, it is valuable to focus on the filtered data when the *UI*-BL correlations are high and in-phase to determine how this relationship impacts the dynamics of the other flow features. In addition, the fact that there is only a slight change between the two averaged results indicates that there are few records that do not have instances of highly correlated, in-phase, *UI*-BL correlations. By confirming that the *UI*-λ_1 correlation for this sample transitional interaction is the largest, even with filtered high rates of *UI*-BL, indicates that something happening downstream of λ_1 is most likely influencing the unsteady dynamics of the interaction upstream.

The combination of the normalized PSD in Figure 3.25 and the cross-correlations in Figure 3.29 show that the primary flow features have zero lag in their correlated positions and are oscillating at the same characteristic frequency. Extracting a frequency of oscillation for the *UI* shock by using the correlations gives a frequency that matches

that shown in Figure 3.25; this means that the *UI* shock has a repeating frequency and correlation with the other flow features so that the same frequency may be assumed in the case of the *UI* shock. The *UI* shock spectral content cannot be effectively shown by using the same ensemble computations used to calculate the cross-correlations. However, a look at the coherence of the separation shock, closure shock, and boundary layer separation precursor gives further confidence to the conclusion that not only are the *UI* shock, separation shock, closure shock, and boundary layer separation precursor moving at the same frequency, but also in time with one another.

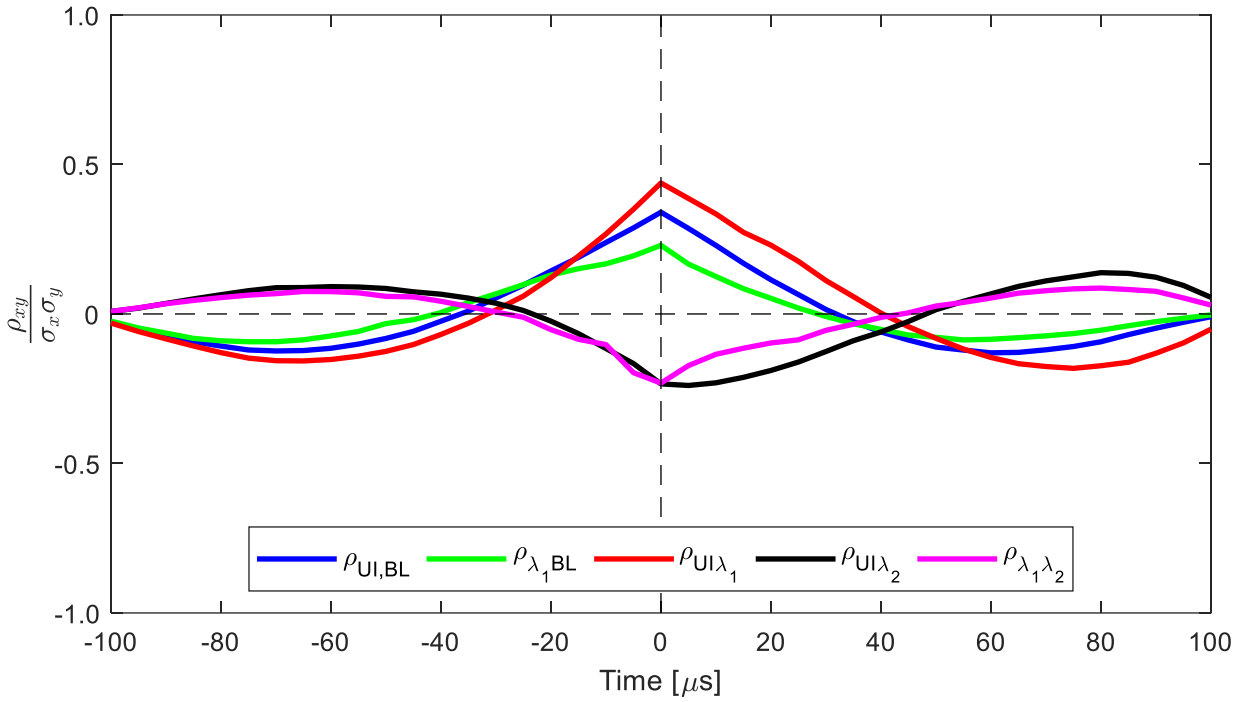

Figure 3.29. Cross-correlation functions of the shock structures and boundary layer thickening location for the blunt fin and flat plate model for a transitional interaction at *x/d* = 7 with records of *UI*-BL > 0.35.

The coherence functions for these flow features are provided in Figure 3.30 for the following relationships: λ_1-λ_2, λ_1-BL, and λ_2-BL. Because the high levels of coherence occur at the dominant oscillation frequency, and there is zero lag between these features

and the *UI* shock, it can be assumed that the *UI* shock would also have a high level of coherence at the same frequencies shown in Figure 3.30.

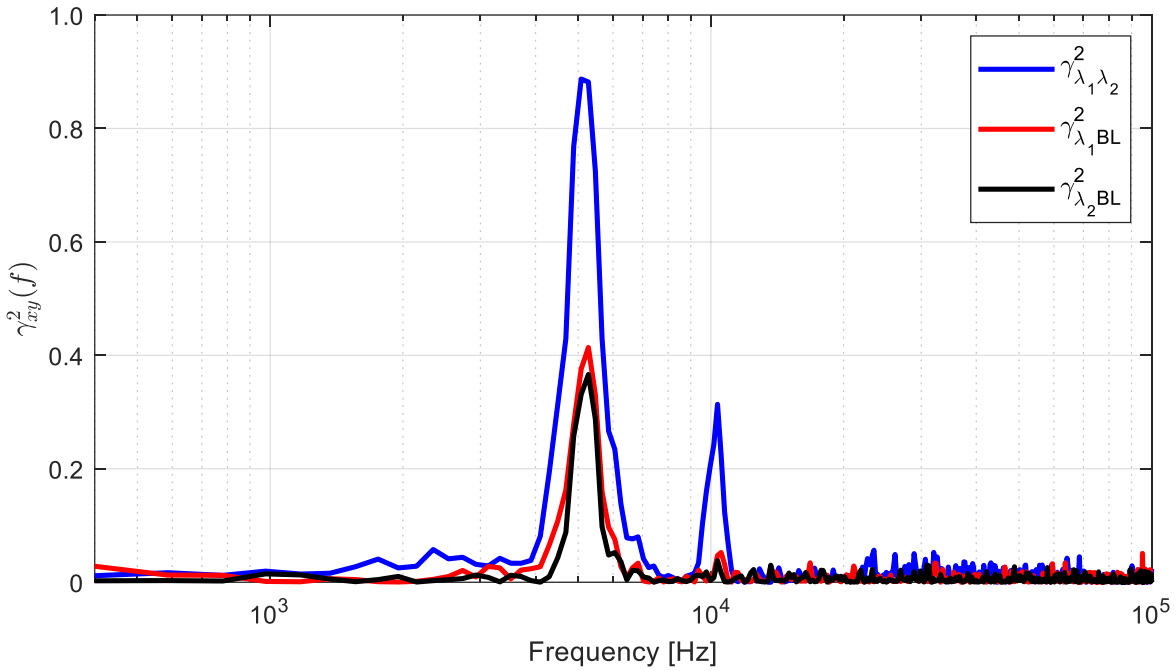

Figure 3.30. Coherence functions of the shock structures and boundary layer separation precursor location for the blunt fin and flat plate model for a transitional interaction at *x/d* = 7.

Now that the boundary layer separation precursor position has been closely evaluated for one sample transitional interaction, how this feature and its relationship to the shock waves evolves as the incoming boundary layer transitions to a fully turbulent state will be examined. The mean positions of the three shock waves and the boundary layer separation precursor for a variety of blunt fin shock generator positions is provided in Figure 3.31. As indicated in the temporal trace at *x/d* = 7 in Figure 3.23, the mean position of the boundary layer separation falls between the *UI* shock and separation shock until it overlaps with the *UI* shock position at *x/d* = 15. Recall from Figure 3.15 that the *UI* shock intermittency at this location was only 0.34.

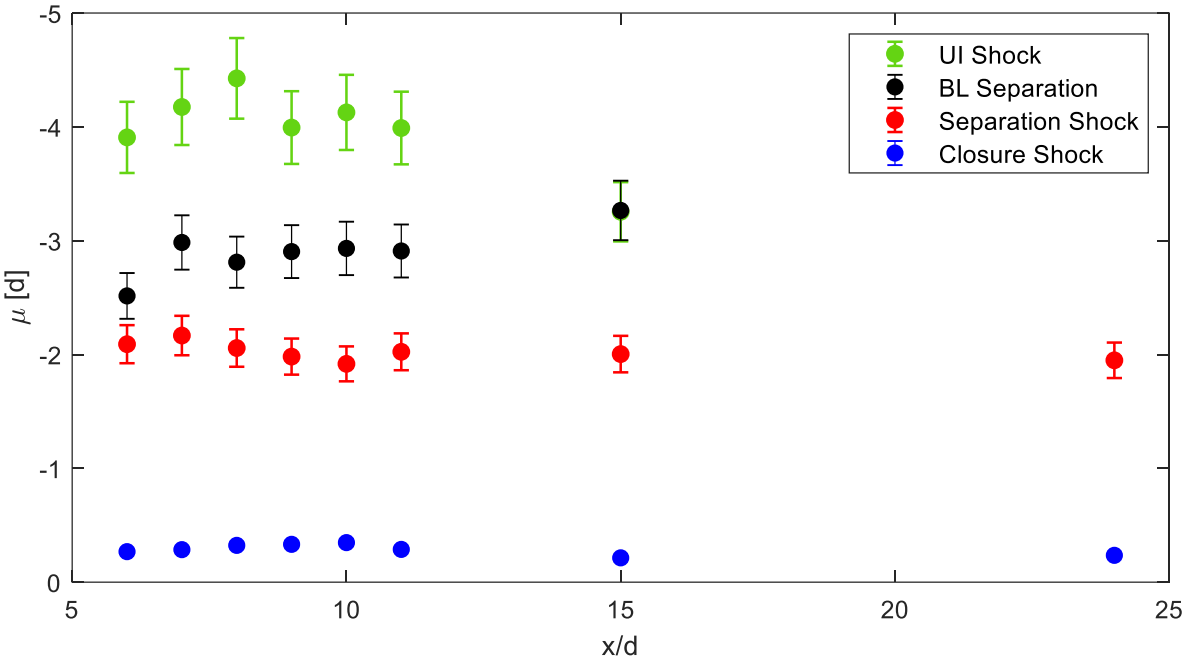

Figure 3.31. Mean position of the three shock waves and the boundary layer separation precursor point for a variety of blunt fin locations on the flat plate model.

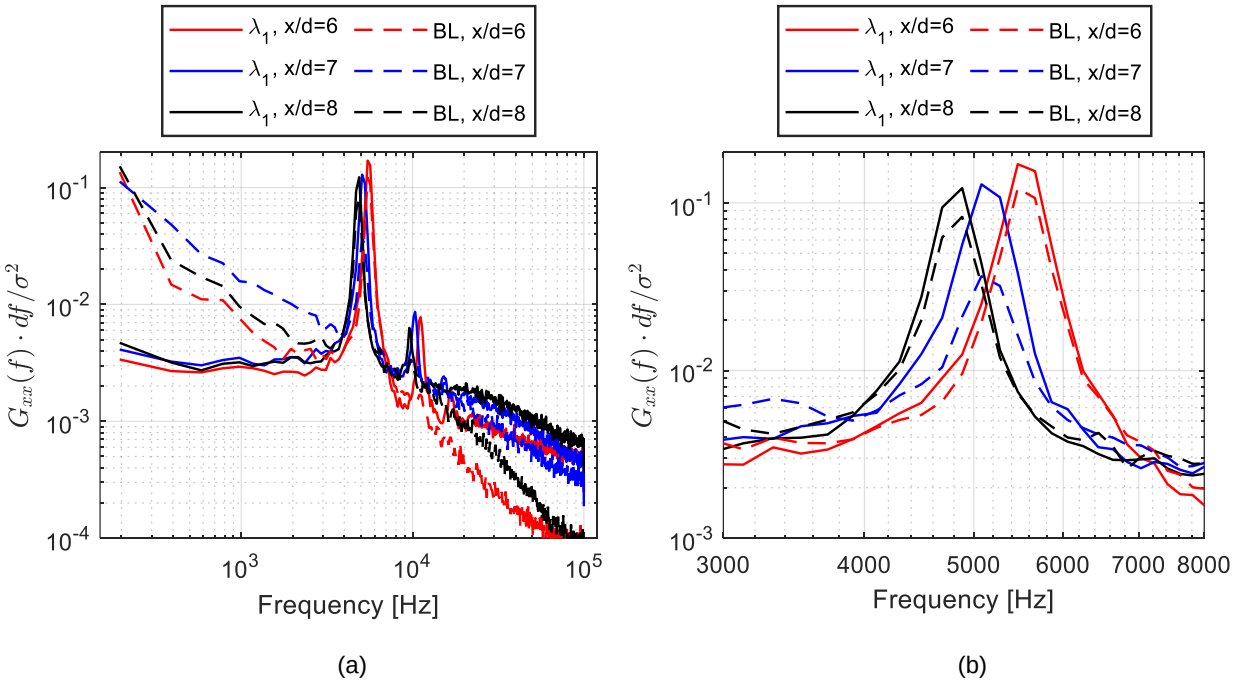

Figure 3.32. PSDs comparing the separation shock and boundary layer separation precursor (BL) for three transitional interactions generated by a blunt fin on a flat plate with (a) the full spectral range and (b) a magnification of the high-intensity resonance.

The PSD of the separation shock and the boundary layer separation precursor (BL) for the first three transitional interactions are shown in Figure 3.32. As previously shown in Figure 3.25 for x/d = 7, the frequency of unsteady oscillation is the same for both the separation shock and the boundary layer separation precursor. This trend continues for blunt fin positions x/d = 9-15. Since the high-intensity resonance in the PSDs are the same for the separation shock and boundary layer separation precursor location, the correlations between these two features are examined to determine how they move in conjunction with one another.

These correlations are shown in Figure 3.33 for various blunt fin locations on the flat plate model. The same 0.35 threshold to filter the *UI*-BL correlation as discussed with Figure 3.29 remains applied to the subsequent correlations. There is a slight negative lag of -15 μs with a peak of 0.3 at x/d = 6, whereas the other correlations all have zero lag. The fact that all these correlations are positive indicates that when the boundary layer separation precursor moves upstream, the separation shock also moves upstream relative to their respective means, and vice versa. When there is no lag between the two features, then they are moving together in time. These positive correlations reinforce the observed behavior in the temporal response as shown in Figure 3.23. There doesn't appear to be any trend in the magnitude of the correlations with maximum positive values ranging from 0.23 to 0.31. Even with the limiting factor of *UI*-BL correlations > 0.35, consistent correlations between λ_1-BL exist with similar magnitudes when averaged across records. The correlation for blunt fin position x/d = 15 is not shown as there were not enough sequential tracked *UI* shock appearances (γ_{UI} = 0.34).

In addition to the evolving cross-correlations of the separation shock and boundary layer separation as the blunt fin moves downstream, the cross-correlations between the *UI* shock and boundary layer separation location are also compared in Figure 3.34. All six correlations show a strong resonance that matches the 5.1 kHz in the normalized PSD of Figure 3.25 and Figure 3.32. There is a slight trend in the magnitude of the correlations, with blunt fin positions farther from the flat plate leading edge possessing higher correlations than those closer to the flat plate leading edge.

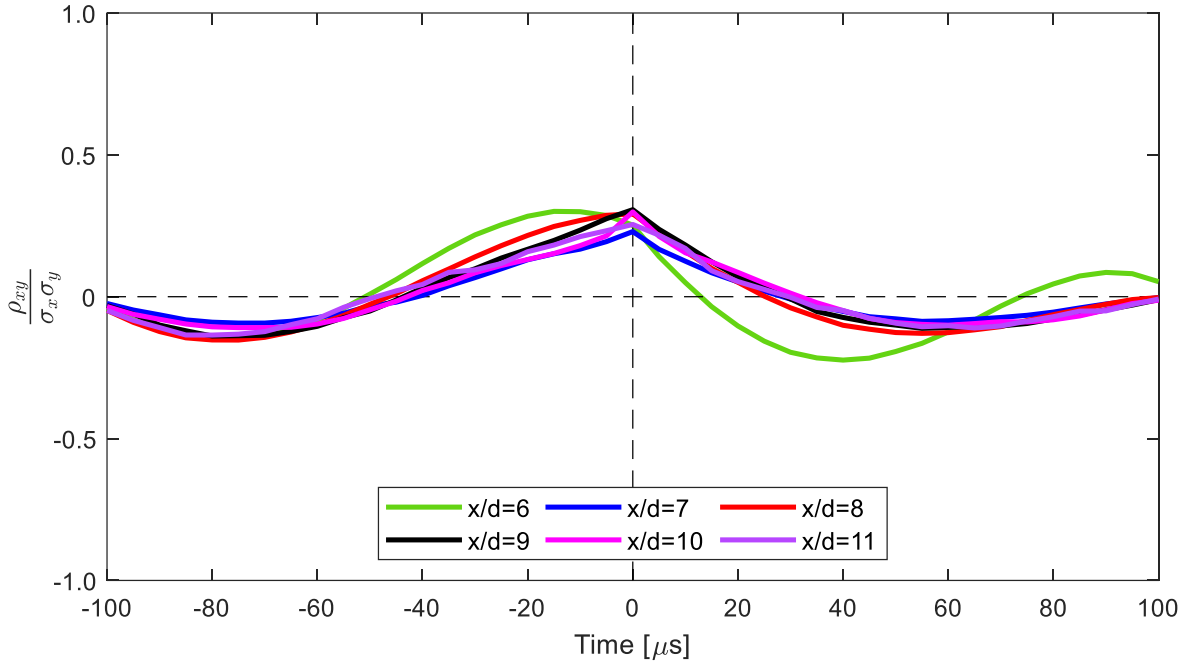

Figure 3.33. Cross-correlation functions between the separation shock and boundary layer separation precursor location for varying blunt fin locations.

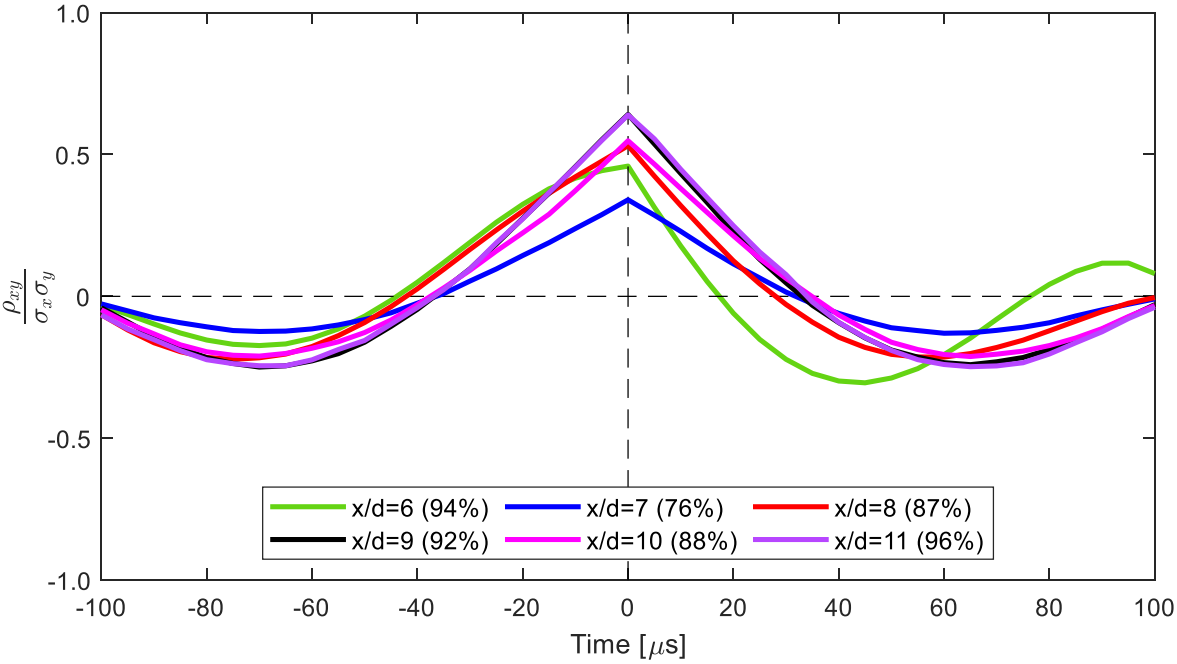

Figure 3.34. Cross-correlation functions between the *UI* shock and boundary layer separation precursor location for varying blunt fin locations.

This means that as the intermittency of the *UI* shock decreases, the correlation in position between *UI*-BL increases. Furthermore, the *UI*-BL correlations are consistently higher than the λ_1-BL correlations for those records when *UI*-BL > 0.35 as defined using the POD analysis, meaning the correlation in position between *UI*-BL dominates that of λ_1-BL. In the legend of Figure 3.34, the percentage of records that met the > 0.35 threshold are provided, showing that it was a significant number and very few were eliminated because there was no correlation or they were out of phase.

Finally, the probability that the *UI* shock is present as a function of the position of the boundary layer separation position as it moves upstream is shown in Figure 3.35a for various blunt fin locations. The PDF of the boundary layer separation position is also provided in Figure 3.35b for the same blunt fin positions (see Figure 3.24). This gives an indication of how the boundary layer separation position impacts to the presence of the *UI* shock. When the boundary layer separation precursor is closer to the separation shock, there is a low probability that the *UI* shock is present in those images. As the boundary layer separation precursor moves upstream, the probability that the *UI* shock is present increases. For almost all blunt fin positions, the peak *UI* probability occurs when the boundary layer separation precursor is located at approximately -3.5*d*. The mean for the boundary layer separation position across the blunt fin locations is -3*d* (Figure 3.31). The fact that the *UI* probability increases past this mean BL separation point indicates that the *UI* shock gets stronger with increasing distance from the separation shock. There is then a slight decrease in the *UI* probability past this maximum probability of the boundary layer separation, meaning the *UI* shock appears less frequently, where it then dissipates. A similar grouping of behavior as observed in Figure 3.6 and Figure 3.34 also seems to exist here; with blunt fin positions *x/d* = 6, 7, and 8 forming one group and *x/d* = 9, 10, and 11 forming another. Each group can be represented by *x/d* = 8 and 10, respectively, for simplicity. The first group has a steeper probability growth rate compared to the second group, which is consistent with the greater intermittency values from Figure 3.6. There is almost a constant probability of the *UI* shock being present for the *x/d* = 15 case that matches the *UI* shock intermittency value of 0.34, again emphasizing little to no correlation between the *UI* shock and the boundary layer feature for this case.

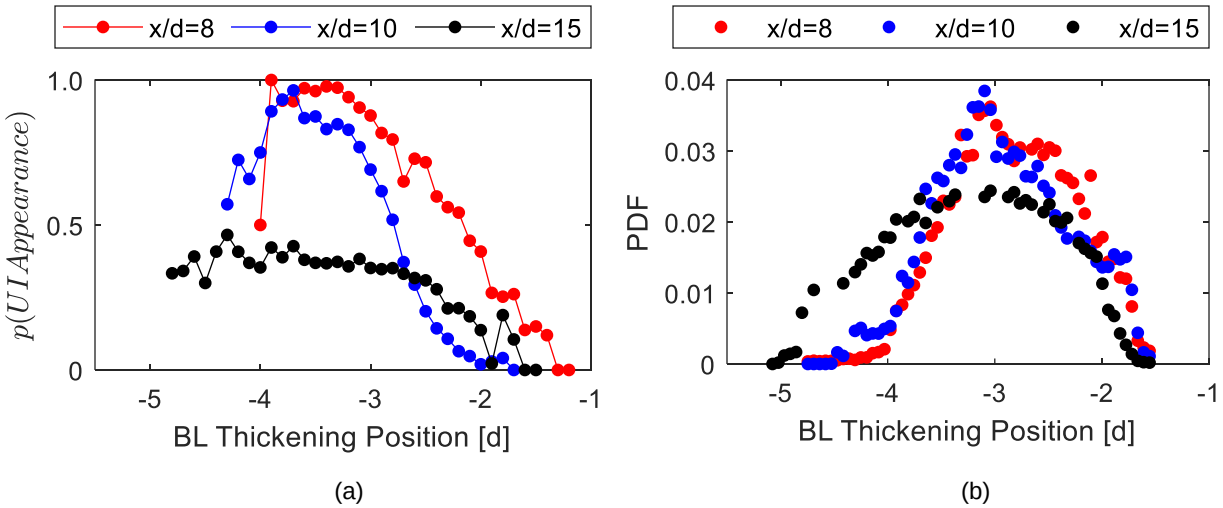

Figure 3.35. The probability that (a) a *UI* shock is generated for a given position of the boundary layer separation precursor for varying blunt fin locations compared to (b) the normalized probability density function of the boundary layer thickening position for three sample blunt fin positions.

This analysis implies that the intermittent spots of turbulent flow that characterize the incoming transitional boundary layer may be what generates the boundary layer separation precursor, which then generates the *UI* shock. This conclusion is based on the increased correlation values between *UI*-BL compared to λ_1-BL when a dominate mode filter is applied as a threshold. For those portions in the unsteady dynamics when the *UI* shock exists and the *UI*-BL correlated positions are in-phase, that motion dominates over the motion of λ_1-BL.

3.4 Cone Model Interaction Dynamics & Discussion

The boundary layer generated on the cone model has different characteristics than that on the flat plate in which the cylinder and blunt fin were examined. Qualitatively, based on images presented in the previous chapter, the interaction for all three cylinder positions on the cone model were transitional interactions. The normalized power spectral density (PSD) for the separation shocks were analyzed from the results of the shock tracking algorithm and are shown in Figure 3.36 below. As before, the frequency content

has been normalized by the Strouhal number. In Figure 3.36a, the entire Strouhal range is shown, whereas Figure 3.36b magnifies the resonance for f = 2 kHz – 20 kHz. Consistent with the previous model results, the high-intensity resonance are in the mid-frequency range. Compared to the flat plate model results, the Strouhal numbers are higher with x/d = 6.25 and 9.5 close to each other at f = 8.7 kHz and 8.4 kHz, respectively. The resonance for x/d = 12.5 is at f = 5.9 kHz. The same trend with decreasing resonance frequency as the shock generator moves farther away from the model leading edge is observed in these results. As previously mentioned, Dussauge *et al*. [82] theorized that the separation shock waves act as low-pass filters for the high frequencies present in the boundary layer. As the shock generator moves farther away from the model leading edge, the high frequency content within the turbulent eddies of the boundary layer increases, which competes with the unsteady oscillations of the separation shock, decreasing the frequency of oscillation of the shock.

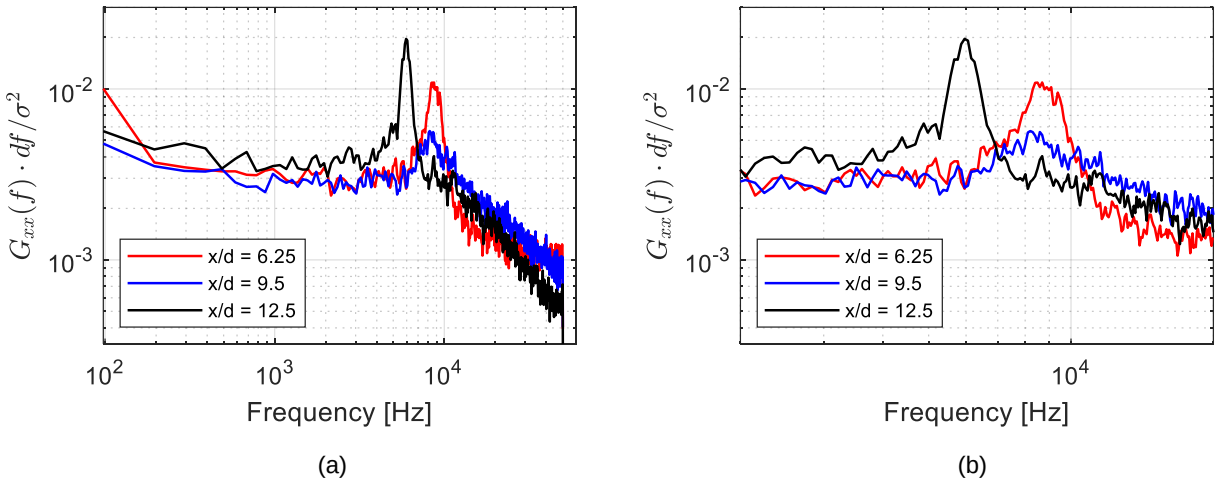

Figure 3.36. Normalized PSDs of the separation shock unsteady motion generated by a vertical cylinder at three locations on a 10° half-angle cone. (a) Presents the full Strouhal number range and (b) magnifies the high-intensity resonance for f = 2 kHz – 20 kHz.

Although not a comprehensive analysis of the interaction region on a cone, these observations are sufficient to corroborate the unique behavior of the separation shock

motion for a transitional interaction with an edge Mach number of 1.8 that was observed with both vertical cylinder and blunt fin shock generators on a flat plate model.

3.5 Unsteady Pressure-Sensitive Paint Data Collection & Analysis

Another diagnostic that was used to characterize the vertical cylinder and flat plate interaction in this flowfield was unsteady pressure-sensitive paint (uPSP). A complete analysis of uPSP results is not provided in this work; however, a preliminary attempt to use this relatively new diagnostic was made and relevant results will be presented as a part of the discussion of interaction unsteadiness. The Innovative Scientific Solutions, Inc. (ISSI) fast-response PSP system [89] was used as a quantitative flow diagnostic technique to compare to high-speed schlieren imaging. Such systems have been shown to achieve temporal resolution greater than 10 kHz [90],[91]. The porous fast-response PSP used in these experiments consisted of an undercoat scattering layer that sits directly on top of the model surface, and then a permeable binder with luminescent molecules on top of the base coat. The absorption of the light energy by the luminophore excites the molecules so they return to the ground state through quenching. Given that quenching due to oxygen competes with relaxation via emission of a photon, the resulting light intensity measurements collected by the camera are directly related to the partial pressure of oxygen in the flow and can be converted into quantitative pressure values given a proper calibration curve [92]. The calibration for the porous fast-response PSP was provided by ISSI [90].

In these experiments, the flat plate model surface was illuminated continuously with two ISSI LM2x-DM 2-inch, water-cooled, ultraviolet LED arrays with 400 nm emission for optimum excitation of the PtTFPP-porous polymer formulation. A Photron FASTCAM Mini AX200 high-speed camera with a 60 mm lens was used to capture the luminescence on the model at a selected frame rate of 20 kHz (640 × 480 pixel resolution), the maximum rated response time of the uPSP. The maximum resolution for this camera is 1024 × 1024 pixels at 6.4 kHz. A 610 nm optical long-pass filter and a 400-450 nm anti-reflective band-

pass filter were placed in front of the camera lens allowing only the paint emission to be captured. A schematic of the uPSP setup is provided in Figure 3.37.

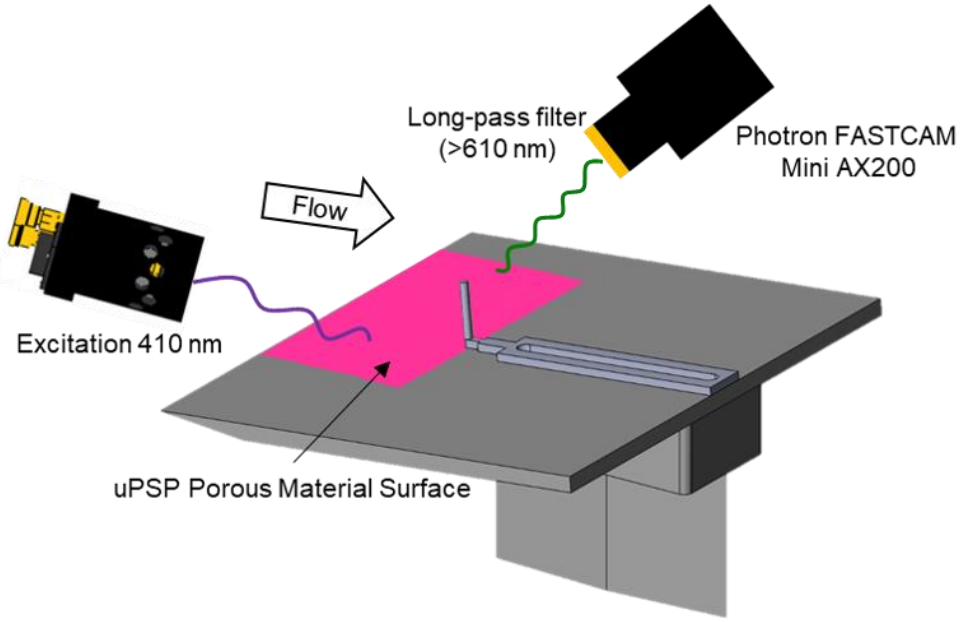

Figure 3.37. Schematic of uPSP setup on the flat plate model.

Both the LED arrays and the AX200 camera were synchronized with the Photron FASTCAM Mini UX100 schlieren camera using two Stanford Research Systems DG535 delay generators. The uPSP luminescence on the model was observed through the BK7 glass of the test section ceiling. This time-resolved, global surface pressure measurement of the unsteady pressure distribution on the flat plate surface upstream of the vertical cylinder was compared to the shock locations derived from the schlieren imaging.

For the purposes of this discussion, a sample transitional interaction case with the vertical cylinder at x/d = 7 and a fully turbulent case at x/d = 25 are considered. It is important to note that unlike with the previous analysis derived from schlieren imaging, uPSP does not show the location of the shock waves, but rather shows unsteady surface pressure. The onset of a pressure increase from freestream values is an indicator of the

approximate point where the boundary layer begins to separate. In order to illustrate these differences for transitional and turbulent interactions, Figure 3.38 shows instantaneous schlieren images and a sample uPSP contour that are scaled for a qualitative comparison of how the shock positions from the schlieren align with pressure on the surface in Pascals (note: the two interactions are not scaled to each other). In addition, the PDF of the *UI* shock and separation shock positions for the transitional interaction in (a) and the separation shock in (b) derived from the schlieren images provide a comparison of the relative scales of unsteadiness.

As previously stated, a pressure increase for the transitional interaction in the uPSP image occurs around the position of the *UI* shock, with the mean location of the separation shock (as indicated by the dashed black line) just upstream of a maximum pressure location. For these experiments, it is expected that the largest pressure loads will be within the separation bubble, as demonstrated by Figure 3.38 for both interactions. There is another surface pressure increase at the base of the vertical cylinder that corresponds well to the closure shock. The similar magnitude in pressure between the separated region and near the closure shock is a result of the contaminated paint near the base of the vertical cylinder model that obscures the results where theory expects the largest pressure loads to be at the closure shock. In the uPSP image for the turbulent interaction of Figure 3.38b, discontinuities in the pressure are visible as spots resulting from rust developing on the plate surface from the interaction of the water-based base coat and the steel flat plate model. However, no rust developed along the centerline of the model. The mean location of the separation shock for the turbulent interaction in (b), as indicated by the PDF, aligns with the sudden pressure rise of the boundary layer separation in the uPSP image. The turbulent interaction has a more finite boundary layer separation process compared to the gradual increase in pressure observed in the transitional interaction.

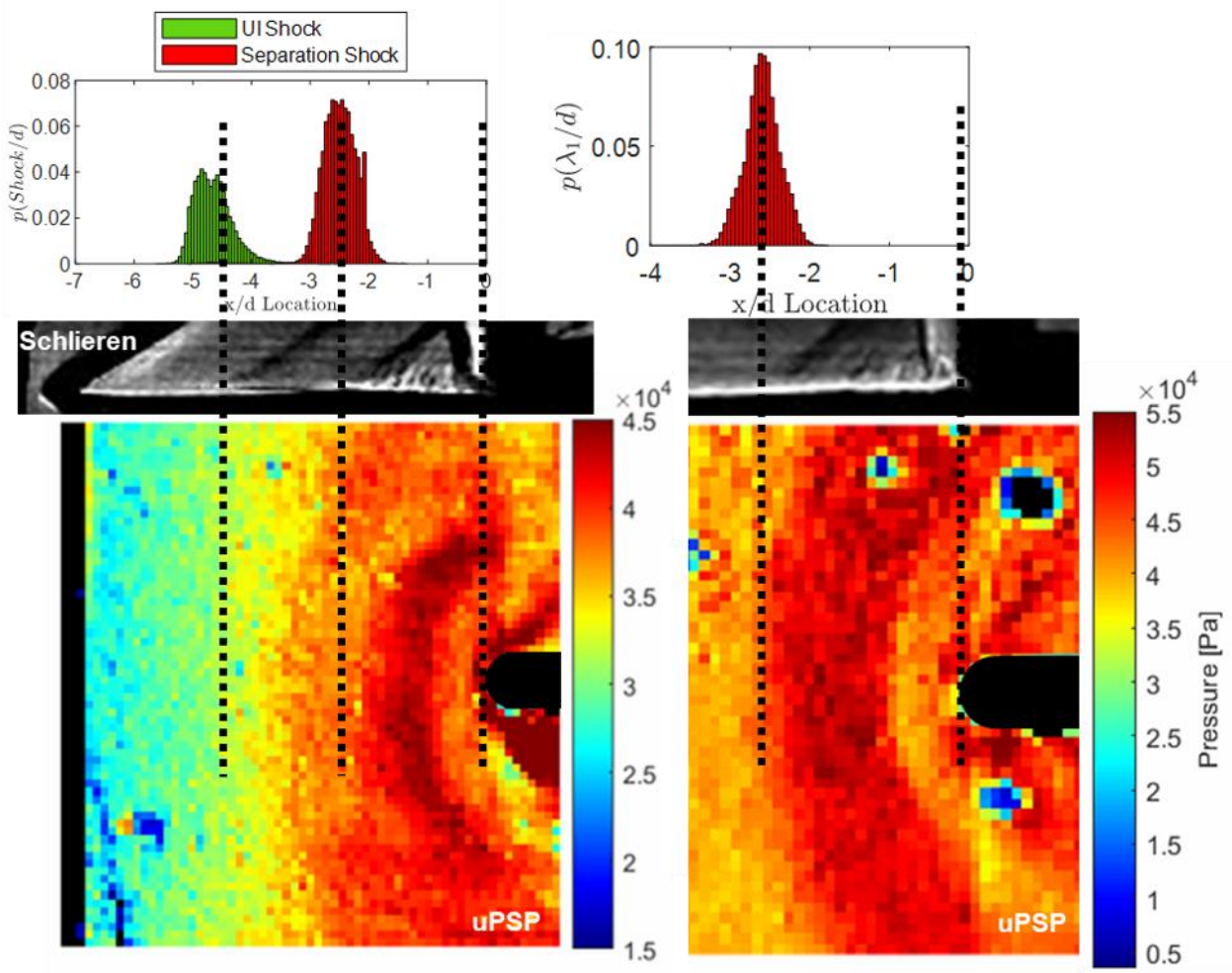

(a) (b)

Figure 3.38. Interaction scaling and dynamics between instantaneous schlieren images and instantaneous uPSP contours for the vertical cylinder and flat plate model for (a) transitional interaction at *x/d* = 7 and (b) turbulent interaction at *x/d* = 25. Flow is from left to right with the cylinder leading edge, separation shock foot mean, and *UI* shock mean identified with dashed black lines. PDF of the shocks taken from the schlieren analysis.

Some of these characteristics are more easily observed through the normalized pressure distribution along the centerline of the interaction. Three distributions are presented in Figure 3.39: (1) the transitional interaction from Figure 3.38a using uPSP, (2) a transitional interaction taken from Murphree *et al.* [14] using pressure transducers, and (3) a turbulent interaction taken from Lindorfer *et al.* [93] using a RANS simulation. All three distributions show the widely-observed plateau in pressure at approximately -2*d*

upstream of the shock-generator face at P/P_∞ = 1.65, which aligns with the separation bubble. The effects of the *UI* shock on the pressure distribution in the two transitional interaction cases is also evident with pressure increases beginning almost -8*d* upstream compared to the -3*d* upstream for the turbulent case. Although the data from Murphree *et al.* [14] did not get closer to the shock generator than -1.3*d*, both the uPSP and RANS pressure distributions show a maximum in pressure at approximately -0.2*d*, which corresponds to the location of the closure shock.

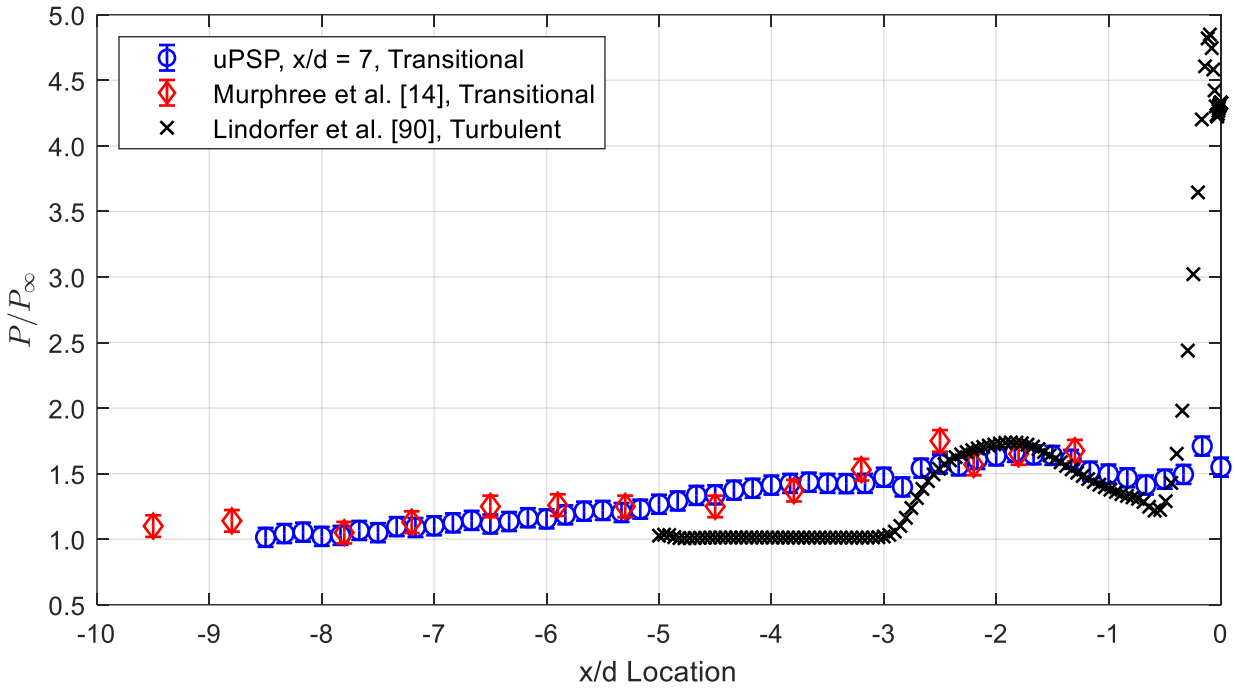

Figure 3.39. Normalized pressure distribution along the centerline of the interaction comparing uPSP data for a transitional interaction at *x/d* = 7 to a transitional interaction from Murphree *et al.* [14] derived from pressure transducers, and a turbulent interaction from Lindorfer *et al.* [93] who used steady state RANS simulations.

In addition to qualitative scaling comparisons between the diagnostic techniques, temporal and spectral information may be derived from the uPSP data to facilitate comparison with the previous schlieren analysis. In Figure 3.40 below, each pixel was processed in a manner similar to the output of a pressure transducer and the evolution of

the pressure characteristics along the centerline of the interaction were evaluated in order to determine if similar unsteady content is observed.

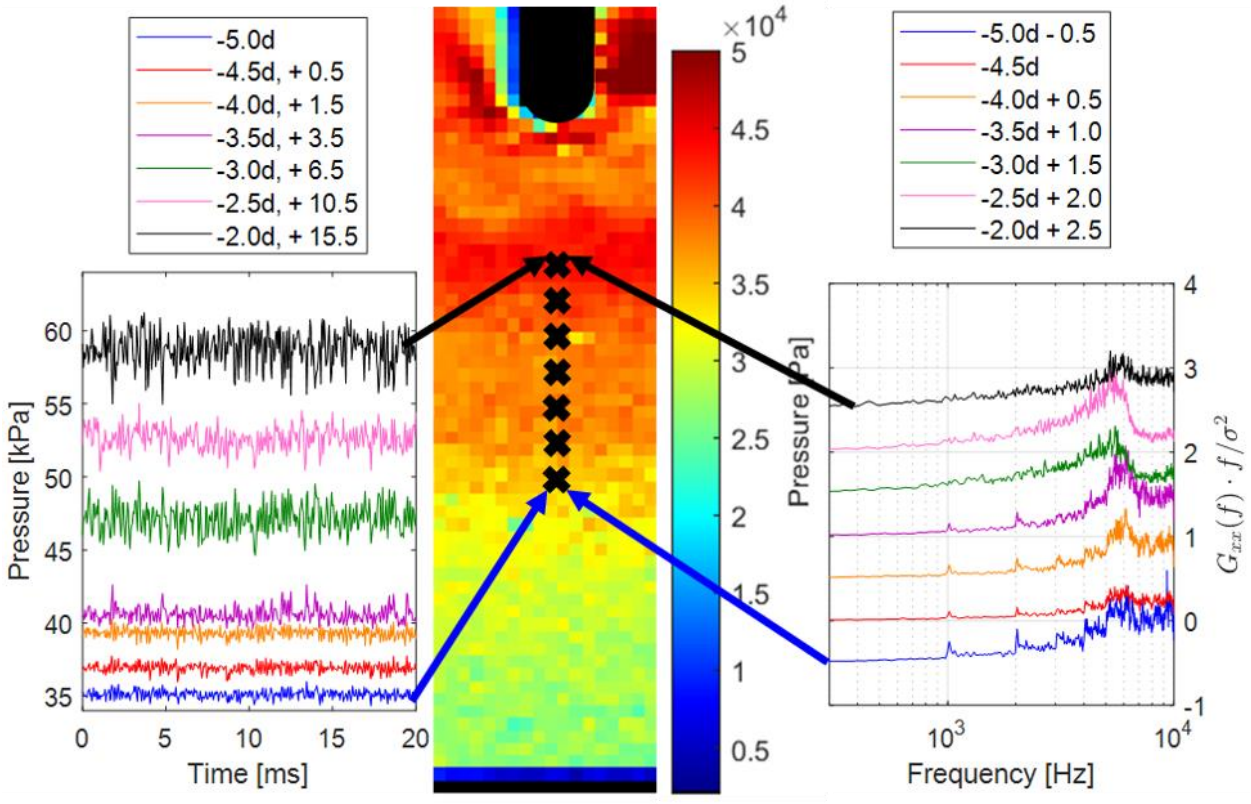

Figure 3.40. Sample pressure time histories and normalized PSD at various *x/d* locations upstream of a transitional interaction with the vertical cylinder at *x/d* = 7. Locations of each temporal or spectral trace are indicated by a black "x" in the corresponding uPSP image. Flow direction is from bottom to top.

As previously discussed in Figure 1.5 and Figure 1.6, the pressure fluctuations and magnitude closest to the freestream are the smallest with a considerable increase in the fluctuations and magnitude under the separation shock and in the separated boundary layer region. For this transitional interaction configuration, the mean separation shock location is -2.4*d*, but the pressure shows a gradual increase in pressure between -3.5*d* and -3*d*. This is consistent with mean *UI* shock position of -3.7*d* as observed in the schlieren images from Section 3.1.1. The corresponding PSDs show the relative level of

unsteadiness between the *UI* shock and the separation shock. In the *UI* shock region, there are local resonances between 5-6 kHz. The strongest intensity resonance occurs at 4.6 kHz and is located at the mean separation shock location -2.5*d* upstream of the vertical cylinder. The PSD closest to the cylinder in the separated boundary layer has the smallest relative resonance and the most broadband noise.

The same temporal and spectral data for the turbulent interaction with the vertical cylinder at *x/d* = 25 is provided in Figure 3.41.

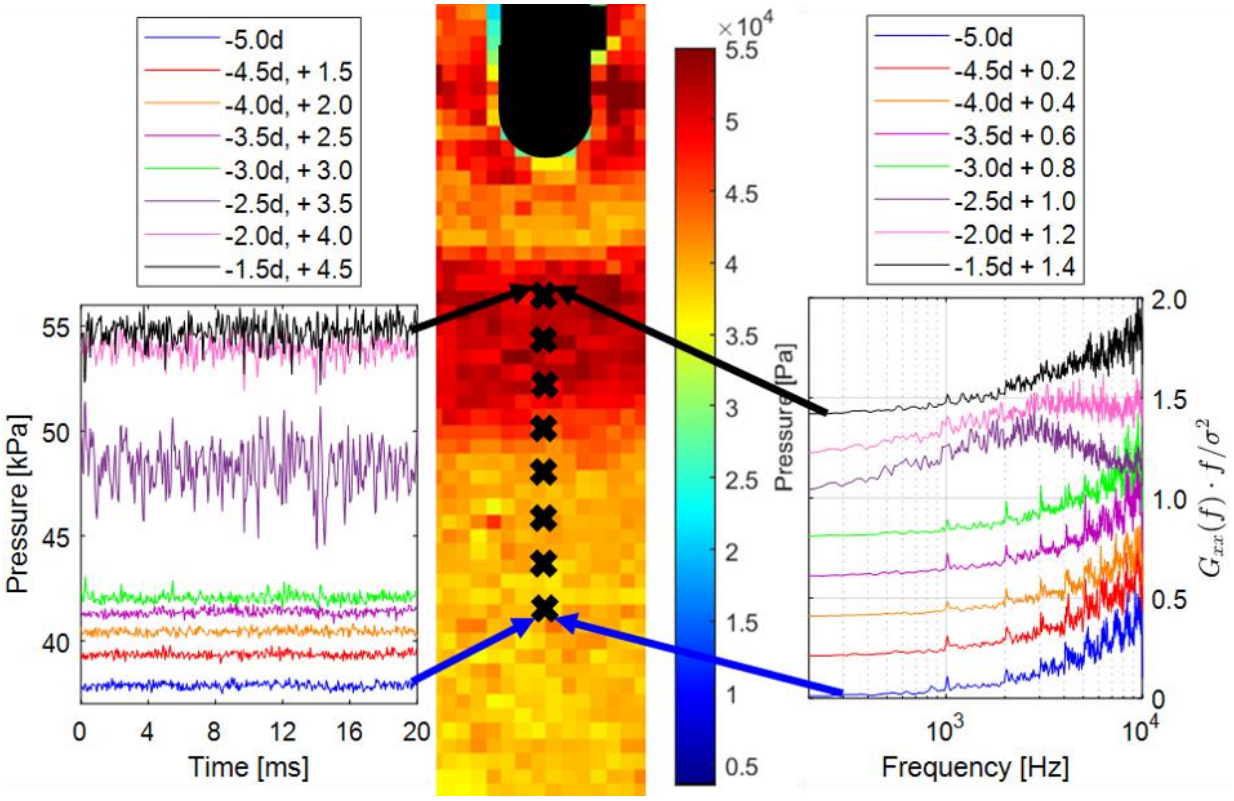

Figure 3.41. Sample pressure time histories and normalized PSD at various *x/d* locations upstream of a turbulent interaction with the vertical cylinder at *x/d* = 25. Locations of each temporal or spectral trace are indicated by a black "x" in the corresponding uPSP image. Flow direction is from bottom to top.

Just as with the transitional interaction in Figure 3.40, the smallest fluctuations in the pressure occur upstream of the separation locations, with the increased fluctuations

occurring -2.5*d* upstream, which corresponds to the mean separation shock position for this configuration. The pressure magnitudes do not show the gradual increase that the transitional interaction demonstrated, owing to the absence of the *UI* shock. This makes the boundary layer separation region smaller; hence, the large increase in fluctuations and pressure between -3*d* and -2.5*d*. The normalized PSDs compare well with Erengil and Dolling [83] who observed high-frequency content in the incoming boundary layer, then low frequencies immediately upstream of the separation shock, then higher frequencies again in the separated boundary layer.

Despite these encouraging results about the usefulness of uPSP, characteristic analysis of SBLI on this model was not continued because of the negative effects the presence of the uPSP had on boundary layer transition. Because the boundary layer on the flat plate model was so thin (~0.5 mm), the presence of the uPSP introduced a surface roughness that accelerated the boundary layer transition process, thus impacting the unsteady dynamics of the shock waves. This is most easily observed by evaluating the PSDs of the separation shock wave from the schlieren images with and without the uPSP on the plate. Recall that the schlieren and uPSP diagnostics were synchronized. For comparison, the PSD from the pressure data at the separation shock mean location is also shown. These PSD comparisons are presented in Figure 3.42 for the transitional interaction (a) at *x/d* = 7 and turbulent interaction (b) at *x/d* = 25. From the schlieren images with a clean flat plate model and a transitional interaction, there is a high-intensity resonance at 4.8 kHz, as previously observed in Figure 3.8b. It is difficult to discern if a resonance exists from the uPSP data, but a small-intensity resonance exists at 6.1 kHz from the schlieren images with the uPSP present. The PSDs for the turbulent interaction in Figure 3.42b are more similar to each other and match previously reported turbulent interaction unsteadiness behaviors [83]. However, both the uPSP and schlieren with uPSP trends show slightly more lower-frequency content than the schlieren with a clean plate. All this is indicative that the induced surface roughness from the uPSP on the flat plate model changes the interaction dynamics of the shock waves and thus was not continued for the purposes of this work.

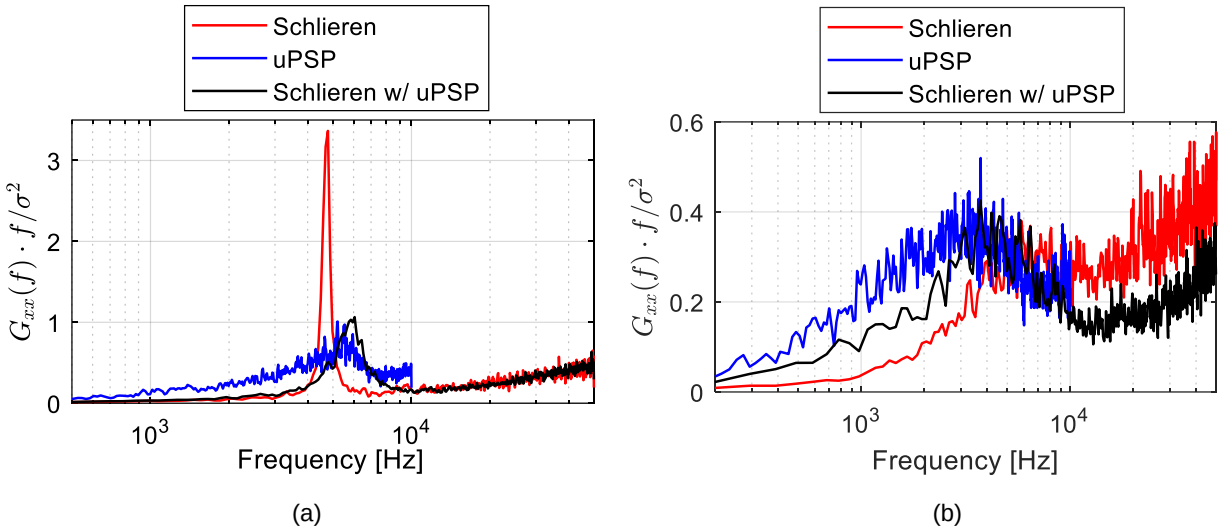

Figure 3.42. PSDs comparing the separation shock unsteadiness from the flat plate and vertical cylinder model for (a) transitional interaction at *x/d* = 7 and (b) turbulent interaction at *x/d* = 25 from different diagnostic combinations: schlieren with a clean plate, uPSP, and schlieren with uPSP on the plate.

However, that doesn't preclude comparison to more recent investigations. Recently, Vanstone *et al.* [94] used unsteady pressure-sensitive paint to characterize the unsteady motion of the shock line (separation shock) and high-speed PIV to characterize the boundary layer separation line in a fully turbulent interaction of a swept compression ramp in a Mach 2 flow. In the uPSP data, Vanstone *et al.* [94] note a maximum PSD value at a Strouhal number of approximately 0.032 for the shock line, compared to 0.029 for the turbulent interaction presented in Figure 3.10 at *x/d* = 25 and around 0.03 for transitional interactions. A maximum PSD value at a higher Strouhal number of 0.067 was reported for the separation line in the PIV [94]. What is interesting is that a PSD peak was observed at all for a fully turbulent interaction for both the shock line and the separation line, considering the more broad-band noise of the turbulent interaction at *x/d* = 25 shown in Figure 3.7. To date, any spectral resonance of the separation shock motion has only been reported based on the configuration described in this work when the incoming boundary layer was in transition. Based on the observed behavior, Vanstone *et al.* [94] classified the spectral content into three regimes: low frequency (*St* < 0.01), mid frequency (0.01 < *St* < 0.10), and high frequency (*St* > 0.1). Just as with the spectral content for the vertical

cylinder interaction in Figure 3.8, Vanstone *et al.* [94] observed the majority of the high-intensity spectral content in the mid frequency range. They concluded that the unsteady motion of the shock and separation were not characteristically similar, and that the shock line spectral content was at significantly lower frequencies than the separation line motion. This finding implies the previously mentioned hypothesis [82] of the separation shock acting as a low-pass filter, but with the addition that it's attenuating the movements of the boundary layer separation line [94]. Finally, Vanstone *et al.* [94] postulated that the separation shock motion was associated with structures in the shear layer of the boundary layer. The cause and effect relationships between these two features are still unclear. This result also appears to contradict the observed spectral analysis correlating the boundary layer separation location in the schlieren images to the shock positions described in Section 3.3; there, the boundary layer separation and separation shock oscillated with the same resonant frequency.

Chapter Four

CONCLUSIONS & FUTURE WORK

4.1 Summary

The purpose of this work was to provide a more in-depth characterization of the unsteady shock wave motion than currently exists in the literature through the use of non-intrusive optical diagnostics. Transitional interaction dynamics are an important source of unsteadiness as characteristics of both laminar and turbulent interactions are present. Furthermore, these interactions are more likely to occur as increased hypersonic efficiency extends regions of laminar flow. Shock wave/transitional boundary layer interactions generated by a vertical cylinder on a flat plate were evaluated at freestream Mach numbers of 2 and 4 with Reynolds numbers of 30×10^6 m^{-1} and $1.13—2.02 \times 10^6$ m^{-1}, respectively. Transitional interactions refer to the state of the incoming boundary layer to the interaction region.

Optical diagnostics centered around high-speed schlieren images that were focused on the centerline of the interaction region. A MATLAB algorithm was developed to track the position of the projected location of the *UI* shock, separation shock (λ_1), and closure shock (λ_2) on the flat plate surface [78]. A separate algorithm was developed to track a boundary layer thickening feature observed in transitional interactions between the *UI* and separation shocks in the Mach 2 freestream experiments. In an effort to obtain a global surface pressure flowfield characterization, unsteady pressure-sensitive paint (uPSP) was applied to the flat plate surface in the Mach 2 facility as an additional optical diagnostic technique.

4.2 Conclusions

Experiments in the Mach 2 freestream facility centered around a vertical cylinder shock generator on a flat plate model. A laminar boundary layer was not observed, so the results focused on comparing the interaction dynamics between incoming transitional and turbulent interactions. A slight compression effect near the plate leading edge decreased the scaling of the *UI* shock and separation shock, before larger scales typically associated with transitional interactions were achieved. The majority of these changes in scales impacted the *UI* shock, which varied from -5*d* to -4*d* upstream of the vertical cylinder face. Eventually, the intermittency of the *UI* shock, γ_{UI}, defined as the percentage of images the feature was present in a given test run, decreased to zero when the incoming boundary layer evolved to fully turbulent. The scaling of the separation shock had no noticeable change, remaining between -2*d* and -2.5*d* across all incoming boundary layer states. However, this constant scaling based on shock generator diameter would continue to decrease based on boundary layer thickness as boundary layers continue to thicken.

When applying a spectral analysis of the unsteady motion of the *UI* and separation shocks by taking the normalized power spectral density (PSD) of the shock motion signal, high-intensity resonance frequencies of the *UI* and separation shocks were observed. This specific behavior had not previously been reported in the literature; however, similar spectral content were reported using particle image velocimetry (PIV) and uPSP for the position of the separation shock and boundary layer separation for a swept-ramp shock generator in a turbulent boundary layer [94]. The magnitude of these resonant frequencies evolved as the incoming boundary layer evolved. The closer to the leading edge of the flat plate the cylinder was located, the higher the resonance frequency and the stronger the signal. As the cylinder moved downstream, the resonance frequency decreased along with the magnitude of the signal until the broadband noise typical of a turbulent interaction was reached. All these resonance frequencies remained within the mid-frequency range, varying from St = 0.023—0.034 (3—6 kHz).

In order to determine whether this behavior could be an effect from the cylinder wake, a blunt fin was tested on the flat plate model. To eliminate the two-dimensional flat plate

model as a source of the resonance, a cylinder on a 10° half-angle cone model was tested. The angle of the cone model was chosen so that the same edge Mach conditions as the flat plate would be produced. In both model configuration changes, the same high-intensity resonance was observed for the motion of the *UI* and separation shocks, and there was little difference in the statistical characterization of the shock wave motion. The presence of this resonance means that for an edge Mach condition of 1.8 and a Reynolds number of 30×10^6 m^{-1}, the shock waves behave as oscillators instead of the low-pass filters traditionally described in the literature [40],[82].

The blunt fin shock generator schlieren system had some improvements to it from the original vertical cylinder, which revealed a boundary layer separation precursor in the form of a boundary layer thickening between the *UI* and separation shocks in transitional interactions. This boundary layer thickening appeared highly correlated to the motion and presence of the *UI* shock, so another MATLAB algorithm was developed to track its position. The normalized PSD confirmed that this boundary layer thickening had the same resonant frequency as the separation shock. The statistical data showed that the feature remained centered with similar unsteady dynamics until the intermittency of the *UI* shock decreased below 0.4, at which point it converged with the statistics of the *UI* shock. When the incoming boundary layer was fully turbulent, there was no boundary layer feature upstream of the separation shock. Proper orthogonal decomposition (POD) showed that for a majority of records when the *UI* shock was present, the *UI* shock and boundary layer thickening feature were correlated with each other. In fact, based on *UI*-BL correlations and λ_1-BL correlations, the motion of the boundary layer thickening preempts that of the *UI* shock. Both the boundary layer thickening feature and its effect on the *UI* shock motion have been captured using computational fluid dynamics (CFD) simulations [86],[87], but never so clearly using experimental means. This feature is currently labeled a boundary layer separation precursor, as this is the initial point where an adverse pressure gradient leads to the boundary layer separation at the separation shock [15]. CFD simulations did confirm upstream flow in the boundary layer upstream of the separation shock [86] that would account for the thickening visual in the schlieren images. The farther away from the separation shock the boundary layer thickening traversed, the stronger the *UI* shock

became. In addition to observing this feature in comparable simulations, this boundary layer separation precursor was also observed in experiments conducted in the same Mach 2 facility on an axisymmetric cone model with a vertical cylinder shock generator. It is for this reason that the feature is currently assumed to be a real phenomenon of transitional interactions.

In addition to the schlieren images, uPSP as an optical diagnostic was used on the flat plate model in the Mach 2 facility to try and obtain both streamwise and spanwise surface pressure information with high temporal and spatial resolution. Unfortunately, the inherently porous nature of the uPSP that allows it to capture unsteady motion induced a surface roughness that accelerated the boundary layer transition process. Therefore, direct comparisons to interactions observed with a clean plate using schlieren could not be made. Notwithstanding this distortion, normalized pressure distributions along the centerline for transitional and turbulent interactions were typical of those previously reported in the literature [14],[93]. Both uPSP and pressure transducers captured a gradual rise in pressure starting at -5*d*, indicating the presence of the *UI* shock and the onset of boundary layer separation until a peak pressure point when the boundary layer separates. This maximum pressure in the transitional interactions at approximately *-2d* matches the peak pressure in separation for a turbulent interaction. The finer spatial resolution of the CFD results captured a second increase in pressure (by an order of magnitude) after a minimum near -0.5*d* at the cylinder base. This minimum is the location of the closure shock when the boundary layer reattaches. Despite the complications induced by uPSP for this particular flowfield, centerline pressure profiles confirmed that transitional interactions are a composite of laminar and turbulent interactions through the gradual, upstream increase in pressure and the pressure magnitude in the separation region. All the characteristic behavior from experiments in the Mach 2 facility suggests that the unsteadiness of the shock wave motion was driven by instabilities in the separation boundary layer, downstream of the *UI* shock.

4.3 Future Work

The main contribution of this work is that it provides a more comprehensive analysis of transitional boundary layer interactions using flow visualization to characterize the unsteady dynamics of the shock waves. A specific flowfield condition with a Reynolds number of 30×10^6 m^{-1} and an edge Mach number of 1.8 produced shock wave characteristics where the oscillations were at a resonant frequency. Furthermore, a boundary layer separation precursor upstream of the separation shock in transitional interactions was observed that seems to drive the motion of the *UI* shock. The *UI* shock as an interaction feature has also been characterized, something not comprehensively done until now. Future work could focus on characterizing the boundary layer of these same flowfields to correlate the incoming boundary layer transition process and separation fluctuations to the shock wave motion. Specific suggestions include increasing the boundary layer thickness in the Mach 2 facility in order for uPSP to be used more effectively. Furthermore, PIV or focused laser differential interferometry (FLDI) would assist in understanding the boundary layer velocity profile and could also be used to track shock wave position. This technique could also be used to determine more details about the boundary layer separation precursor. FLDI in particular could be instrumental in characterizing the boundary layer in the Mach 4 facility at UTSI.

Since initial characterizations of transitional interactions in the new Tennessee Aerothermodynamics Laboratory Mach 4 Ludwieg Tube provided information on the evolving dynamics with varying Reynolds number and edge Mach number (see Appendix), continuing this line of inquiry would provide more information on potential connections between boundary layer transition and the observed high-intensity resonance at low-Mach conditions. Additional angles of attack of a flat plate model in combination with varying Reynolds numbers and shock generator positions would help quantify this relationship. In addition, since an axisymmetric model in the Mach 2 facility produced the same inherent characteristic behavior of the shock waves, an axisymmetric model in the Mach 4 facility would help eliminate flat plate edge effects. In this way, the

contributions of the Reynolds number and edge Mach number would be better understood and how they evolve with the incoming boundary layer on the shock wave dynamics.

LIST OF REFERENCES

[1] Knight, D.D. and Degrez, G., “Shock Wave Boundary Layer Interactions in High Mach Number Flows: A Critical Survey of Current Numerical Prediction Capabilities,” Advisory Report 319, AGARD, Vol. 2, Dec. 1998, pp. 1.1-1.35.

[2] Holden, M.S., “A Review of Aerothermal Problems Associated with Hypersonic Flight,” AIAA Paper 86-0267, 24th AIAA Aerospace Sciences Meeting and Exhibit, Reno, NV January 1986.

[3] Gaitonde, D.V., “Progress in Shock Wave/Boundary Layer Interactions,” Progress in Aerospace Sciences, Vol. 72. January 2015, pp. 80-99.

[4] Hadjadj, A. and Dussauge, J.P, “Shock Wave Boundary Layer Interaction,” Shock Waves, Vol. 19, No. 6, November 2009, pp. 449-452.

[5] Delery, J. and Panaras, A., “Shock-Wave Boundary-Layer Interactions in High Mach Number Flows,” Advisory Group for Aerospace Research and Development Report No. 319, May 1996.

[6] Zheltovodov, A., “Shock Waves/Turbulent Boundary Layer Interactions—Fundamental Studies and Applications,” AIAA Paper 96-1977, 27th AIAA Fluid Dynamics Conference, New Orleans, LA, June 1996.

[7] Dolling, D.S., “Fluctuating Loads in Shock Wave/Turbulent Boundary Layer Interaction: Tutorial and Update,” AIAA Paper 93-0284, 31st AIAA Aerospace Sciences Meeting and Exhibit, Reno, NV, January 1993.

[8] Delery, J. and Panaras, A., “Shock-Wave Boundary-Layer Interactions in High Mach Number Flows,” Advisory Group for Aerospace Research and Development Report No. 208, February 1986.

[9] Hankey, W.L., Jr. and Holden, M.S., “Two-Dimensional Shock-Wave Boundary Layer Interactions in High Speed Flows,” Advisory Group for Aerospace Research and Development Report No. 203, June 1975.

[10] Green, J.E., “Interactions Between Shock Waves and Turbulent Boundary Layers,” Progress in Aerospace Sciences, Vol. 11, 1970, pp. 235-340.

[11] Korkegi, R.H., “Effect of Transition on Three-Dimensional Shock-Wave/Boundary-Layer Interactions,” AIAA Journal, Vol. 10, No. 3, March 1972, pp. 361-363.

[12] Dolling, D.S., Clemens, N.C, and Hood, E., “Exploratory Experimental Study of Transitional Shock Wave Boundary Layer Interactions,” Rept. AFRL-SR-AR-TR-03-0046, January 2003.

[13] Murphree, Z.R., Jagodzinski, J., Hood, E.S., Clemens, N.T., and Dolling, D.S., “Experimental Studies of Transitional Boundary Layer Shock Wave Interactions,” AIAA Paper 2006-326, 44th AIAA Aerospace Sciences Meeting and Exhibit, Reno, NV, January 2006.

[14] Murphree, Z.R., Yuceil, K.B., Clemens, N.T., and Dolling, D.S., “Experimental Studies of Transitional Boundary Layer Shock Wave Interactions,” AIAA Paper 2007-1139, 45th AIAA Aerospace Sciences Meeting and Exhibit, Reno, NV, January 2007.

[15] Murphree, Z.R., “Physics of Unsteady Cylinder-Induced Transitional Shock Wave Boundary Layer Interactions,” 2009, Dissertation, The University of Texas, Austin.

[16] Giepman, R.H.M., Schrijer, F.F.J., and van Oudheusden, B.W., “High-Resolution PIV Measurements of a Transitional Shock Wave-Boundary Layer Interaction,” Experiments in Fluids, Vol. 56, No. 6, June 2015, pp. 1-20.

[17] Reshotko, E., Bushness, D.M., and Cassidy, M.D., “Report of the Task Force for Boundary Layer Transition,” NASP Technical Memorandum 1007, April 1987.

[18] Jenkins, D.R., Dana, W.H., “X-15: Extending the Frontiers of Flight,” NASA SP, Vol. 562, 2007, https://www.nasa.gov/pdf/470842main_X_15_Frontier_of_Flight.pdf.

[19] Gibbs, Y. “NASA Armstrong Fact Sheet: X-15 Hypersonic Research Program,” NASA, 2014, https://www.nasa.gov/centers/armstrong/news/FactSheets/FS-052-DFRC.html.

[20] Heffner, K.S., Chpoun, A., and Lengrand, J.C., “Experimental Study of Transitional Axisymmetric Shock-Boundary Layer Interactions at Mach 5,” AIAA Paper 93-3131, 24th AIAA Fluid Dynamics Conference, Orlando, FL, July 1993

[21] Özcan, O., and Holt, M., “Supersonic Separated Flow Past a Cylindrical Obstacle on a Flat Plate,” AIAA Journal, Vol. 22, No. 5, May 1984, pp. 611-617.

[22] Dolling, D.S., and Bogdonoff, S.M., “Scaling of Interactions of Cylinders with Supersonic Turbulent Boundary Layers,” AIAA Journal, Vol. 19, No. 5, May 1981, pp. 655-657.

[23] Davidson, T.D.C., and Babinsky, H., “Influence of Boundary-Layer State on Development Downstream of Normal Shock Interactions,” AIAA Journal, Vol. 56, No. 6, June 2018, pp. 2298-2307.

[24] Dolling, D.S., and Brusniak, L., “Correlation of Separation Shock Motion in a Cylinder-Induced Interaction with Pressure Fluctuations Under the Separated Region,” 29th Aerospace Sciences Meeting, Reno, NV, January 1991.

[25] Voitenko, D.M., Zubkov, A.I., and Panov, Y.A., “Existence of Supersonic Zones in Three-Dimensional Separated Flows,” Mekhanika Zhidkosti I Gaza, Vol. 2, No. 1, 1967, pp. 20-24.

[26] Edney, B.E., Bramlette, T.T., Ives, J., Hains, F.D., and Keyes, J.W., “Theoretical and Experimental Studies of the Shock Interference Heating,” Report 9500-920-195, Bell Aerospace Company, October 1970.

[27] Wheaton, B.M., Bartkowicz, M.D., Subbareddy, P.K., Schneider, S.P, and Candler, G.V., “Roughness-Induced Instabilities at Mach 6: A Combined Numerical and Experimental Study,” AIAA Paper 2011-3248, 41st AIAA Fluid Dynamics Conference, Honolulu, HI, June 2011.

[28] Young, F.L., Kaufman, L.G., and Korkegi, R.H., “Experimental Investigation of the Interactions Between Blunt Fin Shock Waves and Adjacent Boundary Layers at Mach Numbers 3 and 5,” ARL Report 68-0214, December 1968.

[29] Blasius, H., “Grenzschichten in Flüssigkeiten mit Kleiner Reibung,” Math Physics, Vol. 56, 1908, pp. 1-37.

[30] Schetz, J.A., “Boundary Layer Analysis,” Prentice-Hall: Upper Saddle River, NJ, 1993.

[31] Dolling, D.S., and Brusniak, L., “Separation Shock Motion in Fin, Cylinder, and Compression Ramp-Induced Turbulent Interactions,” AIAA Journal, Vol. 27, No. 6, June 1989, pp. 734-742.

[32] Thomas, A.S.W., “The Unsteady Characteristics of Laminar Juncture Flows,” Physics of Fluids, Vol. 30, No. 2, February 1987, pp. 283-285.

[33] Hill, W.G., “Analysis of Experiments of Hypersonic Flow Separation Ahead of Flaps Using a Simple Flow Model,” Grumann Research Memo RM-393, Grumann, 1967.

[34] Holden, M.S., Wadhams, T.P., and MacLean, M., “A Review of Experimental Studies with the Double Cone and Hollow Cylinder/Flare Configurations in the LENS Hypervelocity Tunnels and Comparisons with Navier-Stokes and DSMC Computations,” AIAA Paper 2010-1281, 48th AIAA Aerospace Sciences Meeting, Orlando, FL, January 2010.

[35] Mortazavi, M., and Knight, D., “Shock Wave Boundary Layer Interaction in a Hypersonic Laminar Flow on a Hollow Cylinder Flare,” AIAA Paper 2016-0351, 54th AIAA Aerospace Sciences Meeting, San Diego, CA, January 2016.

[36] Mortazavi, M., and Knight, D., “Simulation of Hypersonic Shock Wave Laminar Boundary Layer Interaction over Blunt Fin,” AIAA Journal, Vol. 57, No. 8, August 2019, pp. 3506-3523.

[37] Lee, S., and Gross, A., “Numerical Investigation of Super- and Hypersonic Laminar Shock Wave Boundary Layer Interactions,” AIAA Paper 2019-3441, AIAA Aviation 2019 Forum, Dallas, TX, June 2019.

[38] Cary, Jr., A.M., “Summary of Available Information on Reynolds Analogy for Zero-Pressure-Gradient, Compressible, Turbulent Boundary Layer Flow,” NASA Technical Note D-5560, January 1970.

[39] Chi, S.W., and Spalding, D.B., “Influence of Temperature Ratio on Heat Transfer to a Flat Plate Through Turbulent Boundary Layer in Air,” Proceedings of the Third International Heat Transfer Conference – Vol. 2, American Institute of Chemical Engineering, 1966, pp. 41-49.

[40] Clemens, N.T., and Narayanaswamy, V., “Low-Frequency Unsteadiness of Shock Wave/Turbulent Boundary Layer Interactions,” Annual Review of Fluid Mechanics, Vol. 46, 2014, pp. 469-492.

[41] Pope, S.B., “Turbulent Flows,” Cambridge University Press: Cambridge, United Kingdom, 2000.

[42] Babinksy, H., and Harvey, J.K., “Shock Wave-Boundary Layer Interactions,” Cambridge University Press, United Kingdom, 2011.

[43] Westkaemper, J.C., “Turbulent Boundary-Layer Separation ahead of Cylinder,” AIAA Journal, Vol. 6, No. 7, 1968, pp. 1352-1355.

[44] Plotkin, K.J., “Shock Wave Oscillation Driven by Turbulent Boundary Layer Fluctuations,” AIAA Journal, Vol. 13, No. 8, August 1975, pp. 1036-1040.

[45] Gonsalez, J.C., and Dolling, D.S., “Correlation of Interaction Sweepback Effects on the Dynamics of Shock-Induced Turbulent Separation,” AIAA Paper 93-0776, 31st AIAA Aerospace Sciences Meeting, Reno, NV, January 1993.

[46] Beresh, S.J., Clemens, N.T., and Dollilng, D.S., “Relationship Between Upstream Turbulent Boundary Layer Velocity Fluctuations and Separation Shock Unsteadiness,” AIAA Journal, Vol. 40, No. 12, December 2002, pp. 2412-2422.

[47] Piponniau, S., Dussauge, J.P, Debieve, J.F., and Dupont, P., “A Simple Model for Low-Frequency Unsteadiness in Shock-Induced Separation,” Journal of Fluid Mechanics, Vol. 629, 2009, pp. 87-108.

[48] Brusniak, L., and Dolling, D.S., “Physics of Unsteady Blunt-Fin-Induced Shock Wave/Turbulent Boundary Layer Interactions,” Journal of Fluid Mechanics, Vol. 273, 1994, pp. 375-409.

[49] Poggie, J., Bisek, N.J., Kimmel, R.L., and Stanfield, S.A., “Spectral Characteristics of Separation Shock Unsteadiness,” AIAA Journal, Vol. 53, No. 1, January 2015, pp. 200-214.

[50] Bonne, N., Brion, V., Garnier, E., Bur, R., Molton, P., Sipp, D., and Jacquin, L., “Analysis of the Two-Dimensional Dynamics of a Mach 1.6 Shock Wave/Transitional Boundary Layer Interaction using a RANS based Resolvent Approach,” Journal of Fluid Mechanics, Vol. 862, 2019, pp. 1166-1202.

[51] Reshotko, E., “Boundary-Layer Stability and Transition,” Annual Review of Fluid Mechanics, Vol. 8, 1976, pp. 311-349.

[52] Tennekes, H. and Lumley, J.L., “A First Course in Turbulence,” The MIT Press: Cambridge, MA, 1972.

[53] Schneider, S.P., “Effects of High-Speed Tunnel Noise on Laminar-Turbulent Transition,” Journal of Spacecraft and Rockets, Vol. 38, No. 3, 2001, pp. 323-333.

[54] Reshotko, E., “Transient Growth: A Factor in Bypass Transition,” Physics of Fluids, Vol. 13, No. 5, May 2001, pp. 1067-1075.

[55] Anderson Jr., J.D., “Hypersonic and High-Temperature Gas Dynamics, Second Edition,” AIAA: Reston, VA, 2006.

[56] Floryan, J.M and Saric, W.S., “Stability of Görtler Vortices in Boundary Layers,” AIAA Journal, Vol. 20, No. 3, 1979, pp. 316-324.

[57] El-Hady, N.M. and Verma, A.K., “Görtler Instability of Compressible Boundary Layers,” AIAA Journal, Vol. 22, No. 10, 1983, pp. 1354-1355.

[58] Von Deyn, L.H., Forooghi, P., Frohnapfel, B., Schlatter, P., Hanifi, A., and Henningson, D.S., “Direct Numerical Simulations of Bypass Transition over Distributed Roughness,” AIAA Journal, Vol. 58, No. 2, February 2020, pp. 702-711.

[59] Zhou, L., Zhao, R., and Yuan, W., “Application of Improved k-ω-γ Transition Model to Hypersonic Complex Configurations,” AIAA Journal, Vol. 57, No. 5, May 2019, pp. 2214-2221.

[60] Reed, H.L., Saric, W.S., and Arnal, D., “Linear Stability Theory Applied to Boundary Layers,” Annual Review of Fluid Mechanics, Vol. 28, 1996, pp. 389-428.

[61] van Driest, E.R., and Blumer, C.B., “Boundary Layer Transition: Freestream Turbulent and Pressure Gradient Effects,” AIAA Journal, Vol. 1, No. 6, 1963, pp. 1303-1306.

[62] Wang, T., Simon, T.W., and Buddhavarapu, J., “Heat Transfer and Fluid Mechanics Measurements in Transitional Boundary Layer Flows,” ASME Journal of Engineering for Gas Turbines and Power, 1985, pp. 69-79.

[63] Franko, K.J., and Lele, S.K., “Breakdown Mechanisms and Heat Transfer Overshoot in Hypersonic Zero Pressure Gradient Boundary Layers,” Journal of Fluid Mechanics, Vol. 730, 2013, pp. 491-532.

[64] Chapman, D.R., Kuehn, D.M., and Larson, H.K., “Investigation of Separated Flows in Supersonic and Subsonic Streams with Emphasis on the Effect of Transition,” NACA Report 1356, 1958.

[65] Kaufman, II, L.G., Korkegi, R.H., and Morton, L.C., “Shock Impingement Caused by Boundary Layer Separation Ahead of Blunt Fins,” AIAA Paper 73-236, 11th AIAA Aerospace Sciences Meeting, Washington, D.C., January 1973.

[66] Korkegi, R.H., “Effect of Transition on Three-Dimensional Shock Wave/Boundary Layer Interaction,” AIAA Journal, Vol. 10, No. 3, 1972, pp. 361-363.

[67] Benay, R., Chanetz, B., Mangin, B., and Vandomme, L., “Shock Wave/Transitional Boundary-Layer Interactions in Hypersonic Flow,” AIAA Journal, Vol. 44, No. 6, June 2006, pp. 1243-1254.

[68] Sandham, N.D., Schulein, E., Wagner, A., Willems, S., and Steelant, J., “Transitional Shock-Wave/Boundary-Layer Interactions in Hypersonic Flow,” Journal of Fluid Mechancis, Vol. 752, August 2014, pp. 349-382.

[69] Rice, B.E., McKenzie, J.A., Peltier, S.J., Combs, C.S., Clifford, C., and Thurow, B., “Comparison of 4-Camera Tomographic PIV and Single-Camera Plenoptic PIV,”

AIAA Paper 2018-2036, 2018 AIAA Aerospace Sciences Meeting, Kissimmee, FL, January 2018.

[70] Peltier, S.J., Rice, B.E., Bisek, N.J., McKenna, C.K., and Hofferth, J.W., "Structure of Secondary Motion in a Mach 2 Boundary Layer," AIAA Paper 2018-0583, 2018 AIAA Aerospace Sciences Meeting, Kissimmee, FL, January 2018.

[71] Kocher, B.D, Combs, C.S., Kreth, P.A, Schmisseur, J.D., and Peltier, S.J., "Investigation of the Effects of Distributed Surface Roughness on Supersonic Flows," AIAA Paper 2017-4313, 47th AIAA Fluid Dynamics Conference, Denver, CO, June 2017.

[72] Dolling, D.S., and Bogdonoff, S.M., "Blunt Fin-Induced Shock Wave/Turbulent Boundary-Layer Interaction," AIAA Journal, Vol. 20, No. 12, 1982, pp. 1674-1680.

[73] Combs, C.S., Lindorfer, S.A., Kreth, P.A., and Schmisseur, J.D., "The Role of Boundary-Layer Thickness on Cylinder-Generated Shock Wave/Turbulent Boundary Layer Interactions, Part II: Experiments," AIAA Paper 2018-0824, 2018 AIAA Aerospace Sciences Meeting, Kissimmee, FL, January 2018.

[74] Dolling, D.S., "Comparison of Sharp and Blunt Fin-Induced Shock Wave/Turbulent Boundary-Layer Interaction," AIAA Journal, Vol. 20, No. 10, 1982, pp. 1385-1391.

[75] Lash, E.L., Combs, C.S., Schmisseur, J.D., Kreth, P.A., and Beckman, E.A., "Developing an Image-Based Analysis of the Dynamics of Transitional Shock-Wave/Boundary Layer Interactions," AIAA Paper 2016-4320, 32nd AIAA Aerodynamic Measurement Technology and Ground Testing Conference, Washington, D.C., June 2016.

[76] Willert, C.E., Mitchell, D.M., and Soria, J., "An Assessment of High-Power Light-Emitting Diodes for High Frame Rate Schlieren Imaging," Experiments in Fluids, Vol. 53, No. 2, 2012, pp. 413-421.

[77] Combs, C.S., Lash, E.L., and Schmisseur, J.D., "Investigation of a Cylinder-Induced Transitional Shock Wave/Boundary Layer Interaction Using Laser Diagnostics," AIAA

Paper 2016-4321, 32nd AIAA Aerodynamic Measurement Technology and Ground Testing Conference, Washington, D.C., June 2016.

[78] Combs, C.S., Kreth, P.A., Schmisseur, J.D., and Lash, E.L., “Image-Based Analysis of Shock Wave/Boundary Layer Interaction Unsteadiness,” AIAA Journal, Vol. 56, No. 3, March 2018, pp. 1288-1293.

[79] Wang, G., Garcia, D., Liu, Y., de Jeu, R., and Dolman, A.J., “A Three-Dimensional Gap Filling Method for Large Geophysical Datasets: Application to Global Satellite Soil Moisture Observations,” Environmental Modelling and Software, Vol. 30, 2012, pp. 139-142.

[80] Brusniak, L., and Dolling, D.S., “Flowfield Dynamics in Blunt Fin-Induced Shock Wave/Turbulent Boundary-Layer Interaction,” AIAA Paper 93-3133, 24th AIAA Fluid Dynamics Conference, Orlando, FL, July 1993.

[81] Polivanov, P.A., Sidorenko, A.A., and Maslov, A.A., “Transition Effect on Shock Wave/Boundary Layer Interaction at M=1.47,” AIAA Paper 2015-1974, AIAA SciTech Conference, Kissimmee, FL, January 2015.

[82] Dussauge, J., Dupont, P., and Debieve, J., “Unsteadiness in Shock Wave Boundary Layer Interactions with Separation,” 40th Applied Aerodynamics AAAF Conference, Toulouse, France, March 2005.

[83] Erengil, M.E., and Dolling, D.S., “Unsteady Wave Structure near Separation in a Mach 5 Compression Ramp Interaction,” AIAA Journal, Vol. 29, No. 5, May 1991, pp. 728-735.

[84] Clemens, N.T., and Narayanaswamy, V., “Shock/Turbulent Boundary Layer Interactions: Review of Recent Work on Sources of Unsteadiness,” AIAA Paper 2009-3710, 39th AIAA Fluid Dynamics Conference, San Antonio, TX, June 2009.

[85] Dolling, D.S., and Bogdonoff, S.M, “An Experimental Investigation of the Unsteady Behavior of Blunt Fin-Induced Shock Wave Turbulent Boundary Layer Interactions,” AIAA Paper 81-1287, 14th AIAA Fluid and Plasma Dynamics Conference, Palo Alto, CA, June 1981.

[86] Tester, B.W., Coder, J.G., Combs, C.S., and Schmisseur, J.D., “Hybrid RANS/LES Simulation of Transitional Shock Wave/Boundary Layer Interactions,” AIAA Paper 2018-3224, 2018 Fluid Dynamics Conference, Atlanta, GA, June 2018.

[87] Tester, B.W., “Analysis of Transitional Shock Wave/Boundary Layer Interactions Using Advanced RANS-Based Modeling,” 2018, Master thesis, The University of Tennessee, Knoxville.

[88] Combs, C.S., Lash, E.L., Kreth, P.A., and Schmisseur, J.D., “Investigating Unsteady Dynamics of Cylinder-Induced Shock-Wave/Transitional Boundary Layer Interactions,” AIAA Journal, Vol. 56, No. 4, 2018, pp. 1588-1599.

[89] Crafton, J., Gergory, J., Sellers, M., and Ruyten, W., “Data Processing Tools for Dynamic Pressure-Sensitive Paint,” AIAA Paper 2017-0701, 55th AIAA Aerospace Sciences Meeting, Grapevine, TX, January 2017.

[90] Crafton, J., Forlines, A., Palluconi, S., Hsu, K-Y., Carter, C., and Gruber, M., “Investigation of Transverse Jet Injections in a Supersonic Crossflow Using Fast Responding Pressure-Sensitive Paint,” Experiments in Fluids, Vol. 56, 2015.

[91] Sakaue, H., Morita, K., Iijima, Y., and Sakamura, Y., “Response Time Scales of Anodized-Aluminum Pressure-Sensitive Paints,” Sensors and Actuators A: Physical, Vol. 199, 2013, pp. 74-79.

[92] Bencic, T., “Experimental Techniques: Optical Surface Pressure Measurements using Luminescent Coatings,” Optical Instrumentation Technology and NDE Branch Presentation, NASA Glenn Research Center.

[93] Lindorfer, S.A., Combs, C.S., Kreth, P.A., Bond, R.B., and Schmisseur, J.D., “Limiting Case for Cylinder-Induced Shock Wave/Boundary Layer Interactions,” AIAA Paper 2017-4311, 47th AIAA Fluid Dynamics Conference, Denver, CO, June 2017.

[94] Vanstone, L., Goller, T., Clemens, N.T., and Mears, L.J., “Separated Flow Unsteadiness in a Mach 2 Swept Compression-Ramp Interaction using High-Speed PSP,” AIAA Aviation 2019 Forum, Dallas, TX, June 2019.

[95] Bathel, B.F., Jones, S.B., Watkins, A.N., Berry, S.A., Goodman, K.Z., Lipford, W.E., Combs, C.S., Schmisseur, J.D., Kreth, P.A., and Lash, E.L., “Shock Wave/Boundary-Layer Interaction Studies Performed in the NASA Langley 20-Inch Mach 6 Air Tunnel,” AIAA Paper 2019-2904, AIAA Advanced Measurement Techniques in Wind Tunnel Testing II Conference, Dallas, TX, June 2019.

[96] Micol, J.R., “Langley Aerothermodynamic Facilities Complex: Enhancements and Testing Capabilities,” AIAA Paper 1998-147, 36th AIAA Aerospace Sciences Meeting, Reno, NV, January 1998.

[97] Berger, K., Rufer, S., Hollingsowrth, K., and Wright, S., “NASA Langley Aerothermodynamics Laboratory: Hypersonic Testing Capabilities,” AIAA Paper 2015-1337, 53rd AIAA Aerospace Sciences Meeting, Kissimmee, FL, January 2015.

[98] Berry, S.A., Auslender, A.H., Dilley, A.D., and Calleja, J.F., “Hypersonic Boundary-Layer Trip Development for Hyper-X,” Journal of Spacecraft and Rockets, Vol. 36, No. 6, November-December 2001, pp. 853-864.

[99] Carros, R.J., “Effect of Mach Number on Boundary Layer Transition in the Presence of Pressure Rise and Surface Roughness on an Ogive-Cylinder Body with Cold Wall Conditions,” NACA RM A56B15, April 1956.

APPENDIX

VARYING EDGE MACH NUMBER CONDITIONS

As described in the main body of this work, high-intensity resonance in the spectra for the unsteady motion of the separation shock and boundary layer separation precursor was observed for multiple shock generators on two different model geometries. However, both the edge Mach number and the Reynolds number were approximately the same for these configurations. The question then arises: can this same resonance be duplicated using different freestream conditions in order to investigate the source of the resonance? In this appendix, vertical cylinder generated interactions on a flat plate model in a Mach 4 freestream are considered for multiple plate angles of attack. One angle of attack is meant to duplicate the boundary layer edge conditions of the Mach 2 freestream facility. This provides additional, useful characterization of the unsteady shock wave motion for incoming transitional boundary layer interactions compared to turbulent interactions.

Mach 4 Ludwieg Tube Experimental Setup

UTSI has recently established the Tennessee Aerothermodynamics Laboratory (TALon) that has a Mach 4 Ludwieg tube. This low-enthalpy facility has a constant cross-sectional test section of 610 mm × 610 mm (24 in × 24 in) with a driver tube 610 mm (24 in) in diameter and 32 m (105 ft) long. Stagnation pressure and operation Reynolds numbers are controlled by the number of mylar plastic diaphragms used to create the pressure differential in the facility. The diaphragms are installed directly upstream of a “fat pipe” (914 mm diameter) next to a 508 mm (20 in) long expansion joint before the two-dimensional planar nozzle and test section. A schematic of the Ludwieg tube is provided in Figure A.1. Each piece of mylar is 0.254 mm (0.01 in) thick. The diaphragms are burst by bringing the nozzle, test section, and vacuum chamber side of the system down to near vacuum (~0.07 kPa) and pressurizing the upstream driver tube. The driver tube pressure prior to the diaphragm burst is considered the stagnation pressure and may range from 0 – 1,135 kPa (0 – 150 psig), but is fairly well-controlled by the number of

burst disks used for the run. The stagnation temperature is equal to the ambient room temperature, approximately 300 K. The 8,200 gallon vacuum receiver tank downstream of the nozzle and test section is pressure rated for -2 kPa to 377 kPa (-15 psig to 40 psig). A summary of approximate operational conditions of this facility is provided in Table A.1 for three diaphragm configurations. Steady flow operational time is approximately 130 ms. Optical access for these experiments was provided by BK7 glass windows in the test section sidewalls. Due to the factor of safety for the BK-7 glass windows of this facility, higher operational stagnation pressures (and hence higher Reynolds numbers) could not be achieved.

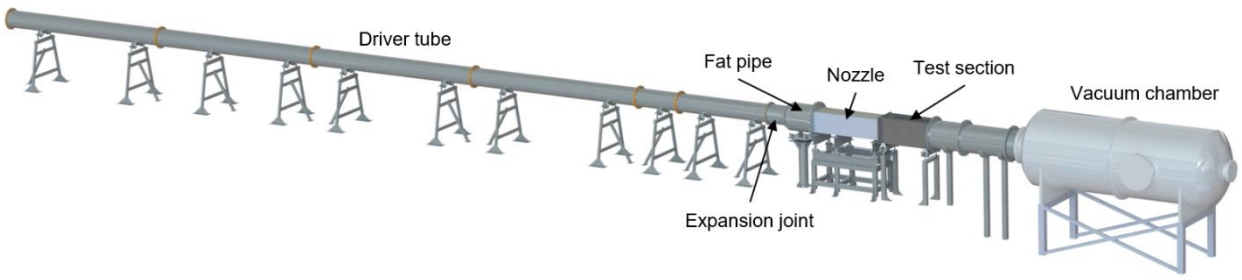

Figure A.1. Schematic of the Mach 4 Ludwieg Tube at the UTSI TALon facility.

Table A.1. UTSI Mach 4 Ludwieg tube approximate operational conditions.

Number of Diaphragms (0.254 mm thick mylar)	**Stagnation Pressure** (kPa)	**Reynolds Number** ($\times 10^6$ m^{-1})
1	138 ± 14	0.62 ± 0.062
2	272 ± 30	1.23 ± 0.135
3	424 ± 45	1.91 ± 0.2

Mach 4 Model Geometry

A stainless steel flat plate model was designed and fabricated for experiments similar to those conducted with the Mach 2 freestream flat plate model, but at three different angles of attack. The focus of this work was still on the centerline of the

interaction immediately upstream of the shock generator. The flat plate was strut-mounted to the test section floor and was 330 mm (13 in) long and 254 mm (10 in) wide. It had a 10° sharp leading edge to provide an attached, oblique leading-edge shock. A vertical aluminum cylinder was mounted to the top surface of the hollow-cylinder and was 12.7 mm (0.5 in) in diameter and 50.8 mm (2 in) tall. A sketch of the flat plate is shown in Figure A.2. Just as with the Mach 2 flat plate configuration, the cylinder attachment was held in place through top-mounted screws in a downstream slot, with mounting holes at least 222 mm (8.75 in) downstream of the leading edge. Three different angles of attack were achieved by using an angled bracket to connect the flat plate to the strut. The three angles of attack were: α = -5°, -15°, and -30°. Similar to the Mach 2 freestream experiments, the α = -5° case was to mitigate potential flow separation at the leading edge of the flat plate. The corresponding edge Mach numbers for the three angles of attack based on oblique shock relations are: 3.6, 2.9, and 1.8, respectively.

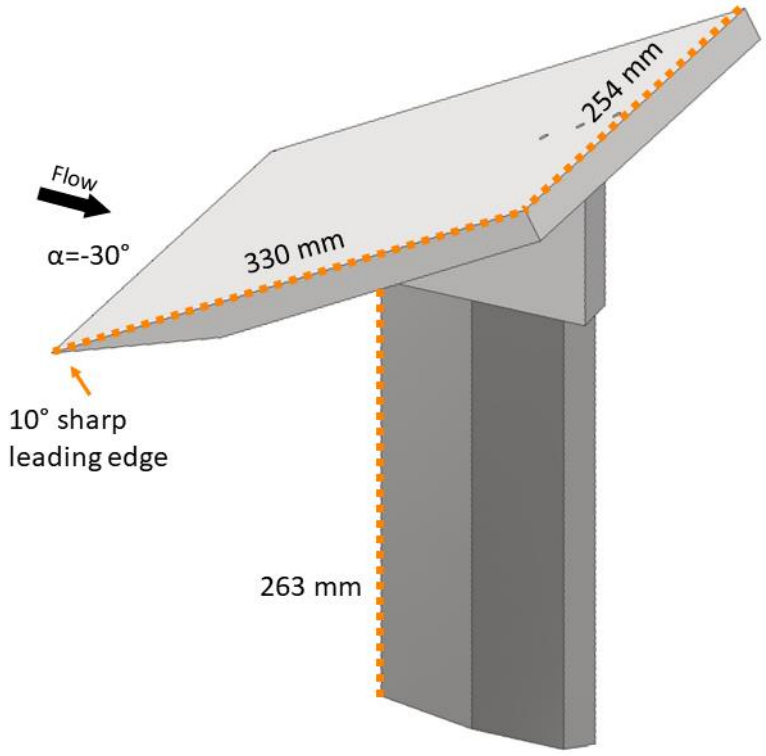

Figure A.2. Schematic of the flat plate model used to vary the edge Mach conditions at the maximum angle of attack (α = -30°) tested in the UTSI Mach 4 Ludwieg Tube.

Mach 4 Schlieren Flow Visualization

The schlieren setup for these experiments also employed a traditional Z-type system with two, 2.54 m focal length mirrors. A Photron FASTCAM SA-Z 2100K monochromatic high-speed camera was employed with a 300 mm camera lens with a selected frame rate of 200 kHz (512 × 136 pixel resolution). The maximum pixel resolution for this camera is 1024 × 1024 pixels at 20 kHz. The selected frame rate seeks to maximize temporal resolution while maintaining the necessary spatial resolution to visualize the flow features of interest. A pulsed light-emitting diode (Luminus Devices CBT-140) provided the high-intensity pulsed light with a 700 ns pulse duration, also developed by Dr. Phillip Kreth at UTSI, and based on Willert *et al.* [76]. A schematic of this setup is shown in Figure A.3.

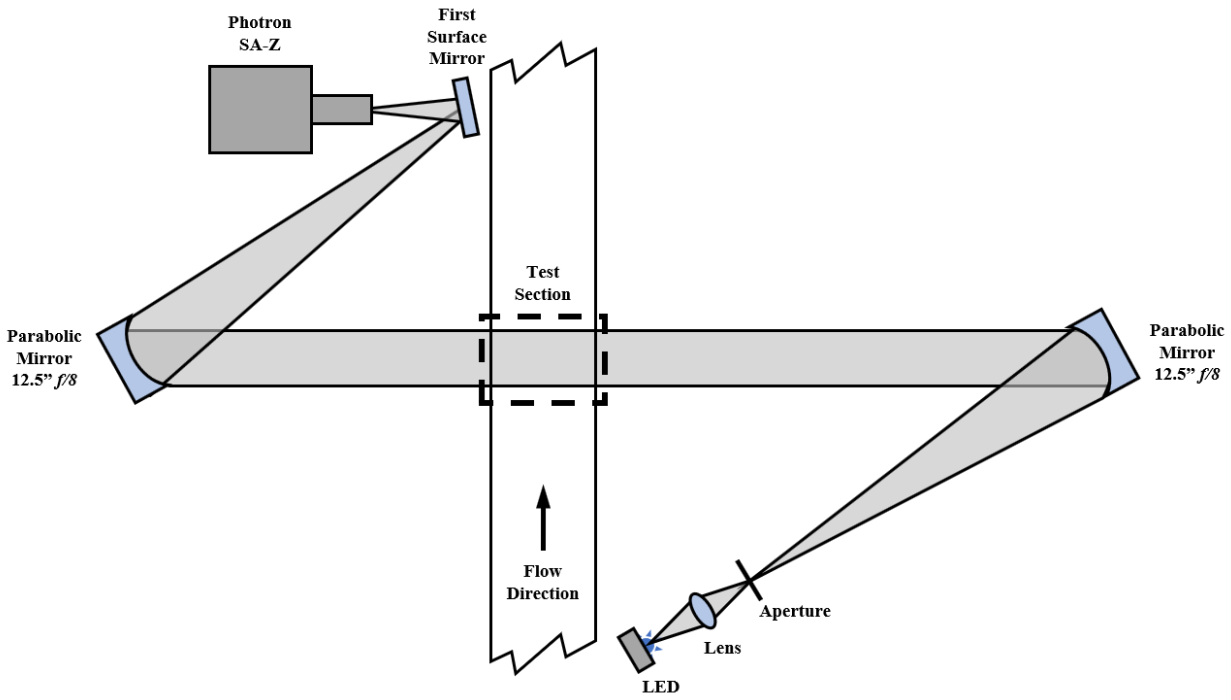

Figure A.3. Schematic of the schlieren setup for the Mach 4 Ludwieg tube at the UTSI TALon Facility.

Varying Edge Mach Conditions Data Results & Discussion

A sample schlieren image sequence showing the interaction from each of the three angles of attack is provided in Figure A.4. In the last image of each sequence, the shock structures are highlighted with the *UI* shock (green), separation shock, λ_1 (red), and closure shock, λ_2 (blue). The images are sequential from top to bottom and the flat plate model surface is visible for both interactions. In Figure A.4a, the flat plate is angled at α = -5° with the vertical cylinder x/d = 19 from the leading edge. The leading edge of the cylinder is on the far right side. As the sequence progresses, the *UI* shock becomes more distinct from the separation shock and increases in scale from -4*d*. The image sequence in (b) has the flat plate at α = -15° and x/d = 15. Similar scales to the test case in (a) are observed with the *UI* shock emanating from the separation shock at -4*d*, while the separation shock remains at approximately -3*d*. Both of these test cases represent transitional interactions where the *UI* shock is visible and separates from the λ_1 shock during the course of the sequence. As a result of the large test scales of this facility with large test section boundary layers and a wide flat plate model, there are some distortions in the appearance of the boundary layer on the flat plate model. This makes tracking any boundary layer features too difficult to do in these schlieren images.

The image sequence in Figure A.4c has the flat plate at α = -30° and x/d = 19. This was the test configuration designed to match the edge conditions of the flat plate model in the UTSI Mach 2 wind tunnel. As a result of the decreased velocity downstream of the flat plate leading edge shock at this severe angle of attack, the lambda-shock interaction scaling is larger than the other two configurations. This interaction is a fully turbulent interaction. This means that no *UI* shock was observed and the position of λ_1 remains around -2*d*. Also, the triple point height, where λ_1 and λ_2 intersect, is clearly above 1*d*. Upstream of the interaction, waves from the turbulent eddies in the boundary layer are observed, another indicator of a turbulent interaction. For all cases, the closure shock, λ_2, is relatively stable -0.25*d* upstream of the vertical cylinder.

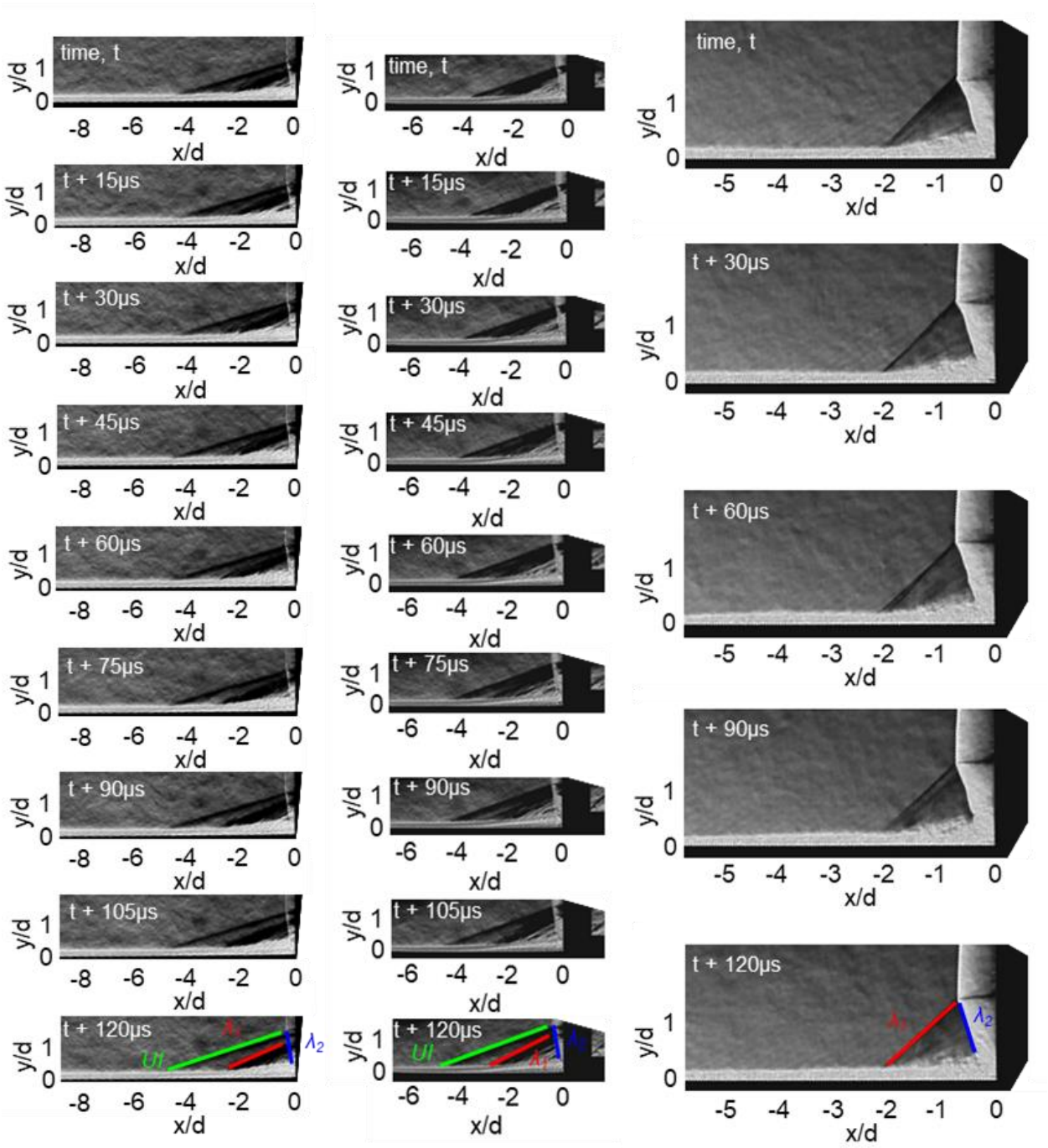

(a) (b) (c)

Figure A.4. Representative schlieren image sequence demonstrating unsteady shock position for an (a) α = -5° for cylinder position *x/d* = 19, (b) α = -15° for cylinder position *x/d* = 15, and (c) α = -30° for cylinder position *x/d* = 19. In the last image of each sequence, the shock structures are identified. The images have been rotated for clarity with flow from left to right.

Recall that the Reynolds number for this facility is controlled by the pressure differential across the diaphragms. This means that each test case may have small variations in the operational Reynolds number. For clarity, a summary of the test cases conducted in this facility is provided in Table A.2 with the corresponding Reynolds number. Note that these reported Reynolds numbers are an order of magnitude lower than the 30×10^6 $m^{-1} \pm 1.5$ for the Mach 2 blowdown facility as discussed in Section 2.2. The different cylinder positions on the flat plate model represent the farthest downstream and most upstream locations, with one intermediate position.

Table A.2. Summary of test configurations of the flat plate model in the Mach 4 Ludwieg Tube.

Angle of Attack (deg)	M_{edge}	x/d	**Number of Diaphragms** (0.254 mm thick mylar)	**Reynolds Number** ($\times 10^6$ m^{-1})
-5	3.6	19	3	2.49 ± 0.2
-5	3.6	10	3	2.47 ± 0.2
-5	3.6	8	3	2.46 ± 0.2
-15	2.9	19	3	2.88 ± 0.2
-15	2.9	15	3	2.86 ± 0.2
-15	2.9	11	3	2.81 ± 0.2
-30	1.8	19	2	1.26 ± 0.135
-30	1.8	15.5	2	1.26 ± 0.135
-30	1.8	12	2	1.26 ± 0.135

The test cases when the flat plate was at α = -30° presented a unique challenge that ultimately did not result in duplicating the edge conditions from the Mach 2 blowdown facility. For this model configuration, a higher Reynolds number transitioned the boundary layer too quickly, resulting in a turbulent interaction; whereas a lower Reynolds number resulted in a weak interaction where the shock waves were difficult to resolve.

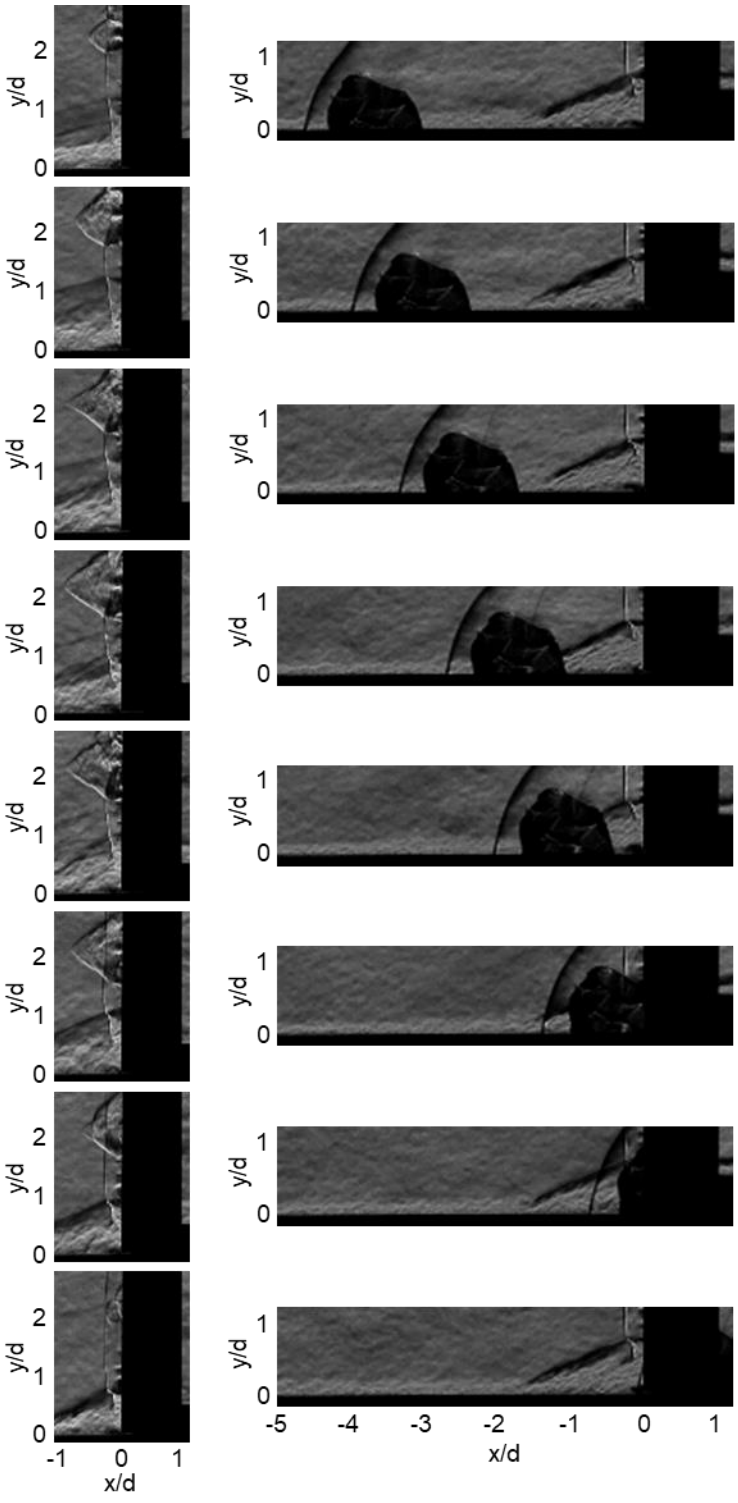

Figure A.5. Schlieren image sequence demonstrating two complications to evaluating the interaction: (a) a small mylar diaphragm piece striking the front face of the vertical cylinder and (b) a large piece of mylar moving off-body, but in the field of view, obscuring the interactions. Flow is from left to right.

An additional complication when using this facility are the small pieces of mylar plastic that would break away from the rest of the material, resulting in impacts on the vertical cylinder face that would disrupt the interaction. Larger pieces of mylar would cause shock waves in the freestream that would obscure the interaction. A sample of these two effects is provided in Figure A.5 for an impact of a small mylar piece on the vertical cylinder in (a) and an off-body mylar piece in (b). The small mylar piece hitting the vertical cylinder alters the inviscid shock and the waves emanating from the piece then interfere with the lambda-shock. The piece moves so quickly that when it strikes the vertical cylinder it moves upstream, before losing enough momentum that it then gets carried back downstream. The larger mylar pieces frequently do not affect the interaction directly, but they do hinder analysis by obstructing the view of the interaction.

Boundary layers at higher Mach numbers are more resistant to transition than at lower Mach numbers [99]. This allowed for some interesting shock behavior when the plate was angled at α = -5°. For example, at x/d = 8, an *UI* shock is present over 97% of the time and has a smaller standard deviation, 0.19d, than the separation shock, 0.33d. The separation shock in particular for this test case was more difficult to resolve, as it was not as distinct a feature, but was more the occasional merging of the expansion waves that emanate from the separated boundary layer downstream of the *UI* shock. This configuration will be discussed in greater detail later. The case where the cylinder was located at x/d = 10 was more similar to the transitional interactions of the previous chapters with a more distinct separation shock and *UI* shock. A fully turbulent interaction was not achieved at this angle of attack with a γ_{UI} = 0.41 at x/d = 19. Further decreases in the edge Mach number made the boundary layer more susceptible to transition, so that only one transitional interaction for α = -15° at x/d = 11 was achieved with a γ_{UI} = 0.28.

The mean positions of the different shock waves across the test cases described in Table A.2 are provided in Figure A.6 with the uncertainty expressed as ± σ. Each angle of attack of the flat plate is represented by a different symbol, with the *UI* shock in green, separation shock in red, and closure shock in blue. As described in Table A.2, there were three positions of the vertical cylinder (x/d) tested for each angle of attack. The *UI* shock across all cylinder positions and angles of attack remains between -5d and -5.7d, with the

slight decrease in scaling a result of the effects from α = -15° when the cylinder was closest to the leading edge. Note that the *UI* shock was not observed for the other two cylinder positions for α = -15°, nor for any position at α = -30°. In fact, there is good convergence on the separation and closure shock mean positions between the α = -15° and -30° plates, with overlap at *x/d* = 19. This finding and the smaller standard deviation at α = -30° makes sense as the incoming boundary layer transitions to turbulent, resulting in smaller separation scales and relative levels of unsteadiness. The largest standard deviations for α = -15° and *x/d* = 11 is also expected as the test case that exhibited the closest interaction behavior to those transitional interactions observed in the Mach 2 facility, despite the larger edge Mach number. These mean trends also capture some of the behavior shown for the separation shock scaling as discussed in Figure 1.9, where the separation shock asymptotes at -2*d* for fully turbulent interactions for varying Mach numbers and shock diameters.

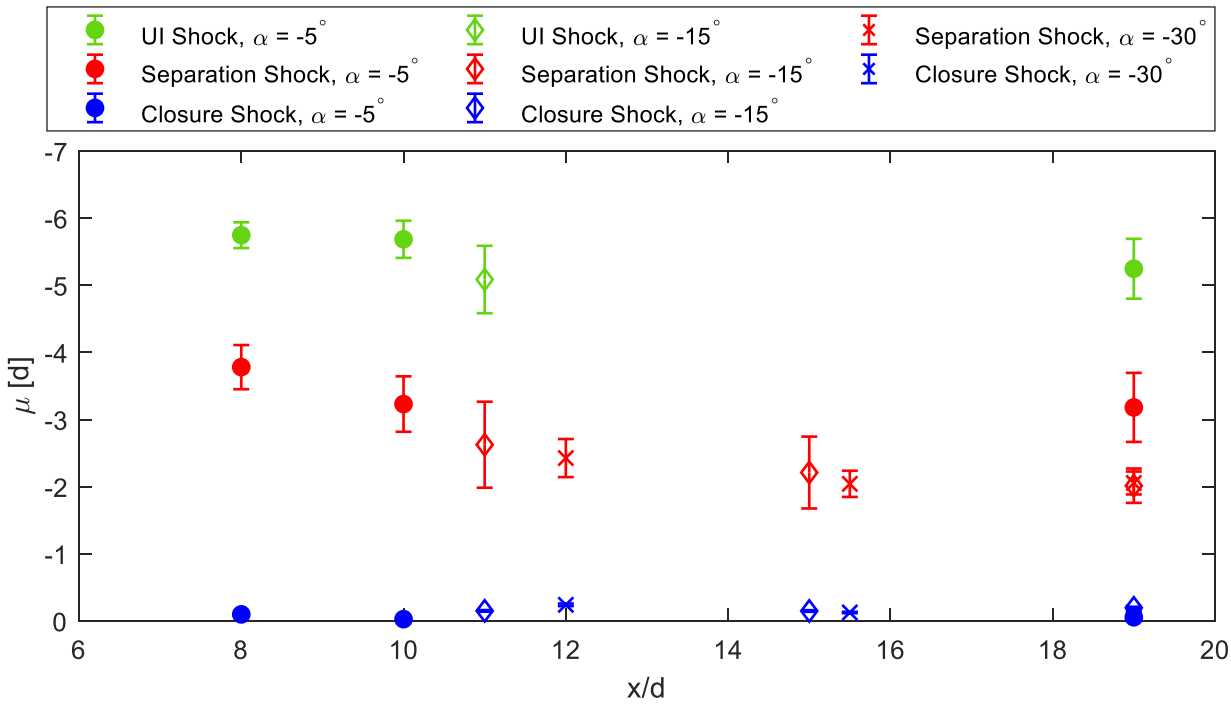

Figure A.6. Mean position of shock waves for all vertical cylinder positions across the three flat plate angles of attack. Uncertainty represent ± σ.

One major difference in these averaged shock positions from the interactions generated in the Mach 2 facility is the larger interaction scale for all the *UI* shock means and for the separation shock for α = -5°. Recall the mean shock positions for the cylinder and blunt fin from Figure 3.14; the separation shock remained around -2*d*, whereas only the fully turbulent interactions for α = -15° and -30° in Figure A***.6*** have those values. The mean separation shock positions for α = -5° vary from -3.2*d* to -3.8*d*. In addition, only the blunt fin shock generator demonstrated upstream positions up to -5*d*, whereas mean positions of -5.7*d* were observed at *x/d* = 8 and 10 for α = -5°. These larger interaction scales indicate preliminarily that the incoming transitional boundary layer was closer to the laminar state than the turbulent state based on results from the literature [13]. Keep in mind that this collapsing of separation scale is based on the constant cylinder diameter; turbulent boundary layers are thicker than laminar and transitional boundary layers. Relative to the boundary layer thickness, the separation shock scale would continue to decrease.

The *UI* shock intermittency, γ_{UI}, for the four interactions where a *UI* shock is present is shown in Figure A**.**7. Recall that the *UI* shock was not observed for any cylinder positions for α = -30°. For the given edge Mach number and Reynolds number for α = -5°, a fully turbulent boundary layer was not achieved on the flat plate model. Either a higher Reynolds number or a longer plate model would be needed to obtain that boundary layer state. The current pressure ratings for the windows in the Mach 4 Ludwieg Tube, however, currently preclude operating at higher stagnation pressures. The decreasing trend in γ_{UI} for α = -5° matches that observed in transitional interactions discussed in the previous chapters as the incoming boundary layer evolves to turbulent.

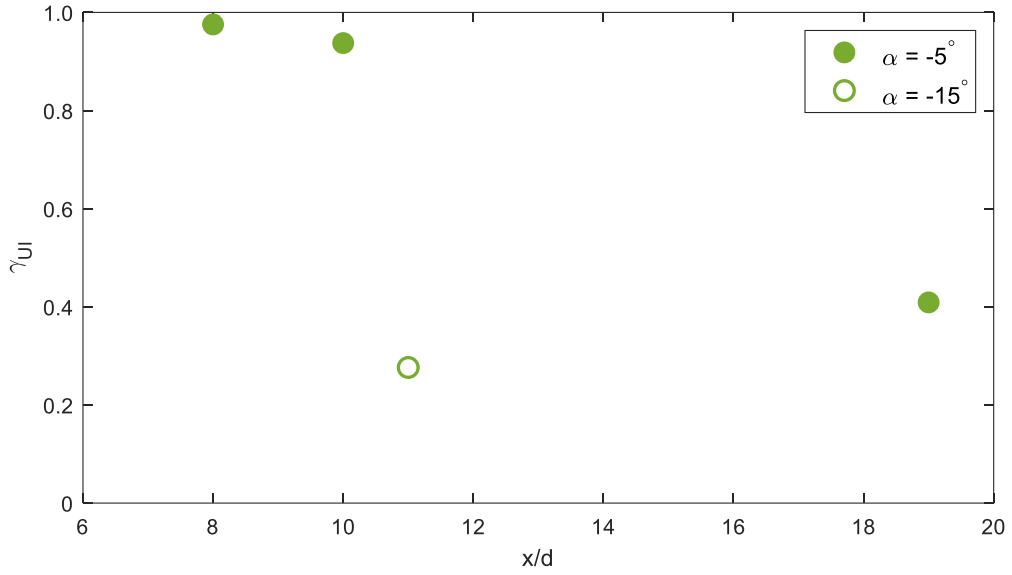

Figure A.7. Comparison of the *UI* shock intermittency between two angles of attack for a vertical cylinder shock generator at various locations on the flat plate model.

Probability density functions (PDF) of the features presented in Figure A.6 are shown below to gain a better understanding of the impact of the combined edge Mach number and Reynolds number on the unsteady motion of the shock waves. The first set of PDFs in Figure A.8 are the separation shock at each cylinder position for plate angles (a) α = -5°, (b) α = -15°, and (c) α = -5°. The expected collapsing of the mean separation shock position as the cylinder moves downstream is observed for all three flat plate angles. One interesting comparison between α = -5° in (a) and α = -15° in (b) at *x/d* = 19 is the difference in the spread of the separation shock position. At *x/d* = 19 in (a), the shock oscillates over 2.4*d*, whereas it only oscillates by 1.1*d* in (b). This is most likely due to the influence of the *UI* shock as the separation shock in (b) at *x/d* = 11 travels 1.9*d* and is the only test case where the *UI* shock was present at that plate angle of attack. That does not explain increased spread in *x/d* = 19 for α = -5° compared to the other, also transitional interactions at this plate angle where each traverse approximately 1.5*d*. The PDFs in (c) for interactions that do not have an *UI* shock exhibit the same decrease in scaling as the other interactions and with the farthest forward position of *x/d* = 12 only varying 0.2*d* more in position than at *x/d* = 15.5 and 19.

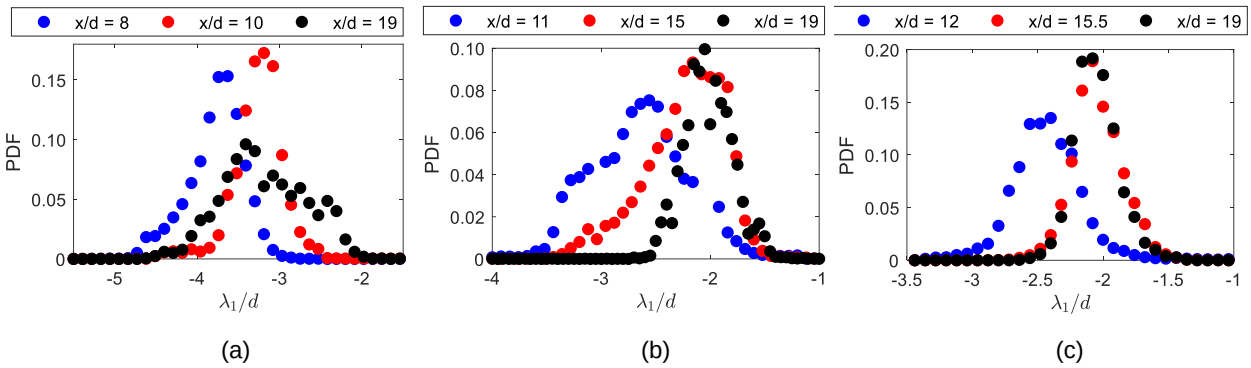

Figure A.8. Probability density functions of the motion of the separation shock, λ_1, at varying vertical cylinder locations for (a) α = -5°, (b) α = -15°, and (c) α = -30°.

Recall that 0.2*d* is within the uncertainty of the shock tracking algorithm. In fact, the overlapping PDF between *x/d* = 15.5 and 19 in (c) indicates that there were negligible differences in the incoming boundary layer between these two cylinder positions.

The PDF of the separation shock for all three plate angles for the same *x/d* = 19 cylinder position is shown in Figure A.9. A vertical cylinder position of *x/d* = 19 represents the farthest extent downstream the model could be placed. Here, the increased interaction scales of separation shock motion are clearly evident as the α = -5° configuration is the only transitional interaction shown in this figure. At the slower edge Mach numbers of the α = -15° and -30° cases, the incoming boundary layer is fully turbulent, accounting for the similar PDF curves and overlapping mean locations as shown in Figure A.6. This provides a good visualization of the effects of the incoming boundary layer state on the separation shock behavior. Higher edge Mach number flowfields have regions of extended laminar flow, which are more susceptible to boundary layer separation due to the increased region of subsonic flow within the boundary layer (recall Figure 1.7), and thus have larger separation scaling and regions of unsteadiness. This particular transitional interaction behaved very similarly to transitional interactions generated by a cylinder and blunt fin in the Mach 2 facility with the same γ_{UI} values.

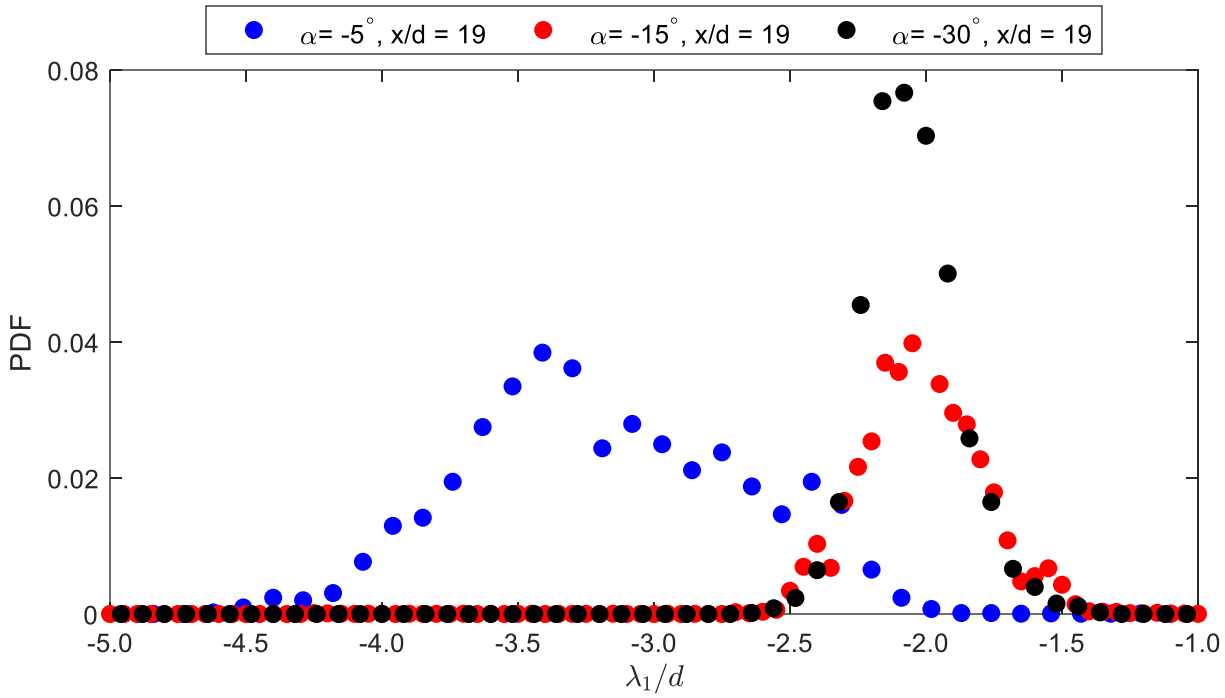

Figure A.9. PDF of the separation shock at the same *x/d* = 19 cylinder position for all three plate angles of attack.

In order to better evaluate the influence of the *UI* shock on the dynamics of the separation shock, the PDFs of the separation shock motion for those cases when the *UI* shock is present are shown in Figure A.10. The effect of the decreased edge Mach number with a similar Reynolds number on the incoming boundary layer becomes evident based on the behavior of the *α* = -15° at *x/d* = 11 case. The probability spreads over 2.1*d*, approximately the same as the separation shock for *α* = -5° at *x/d* = 19. The continued shift towards the cylinder face as the edge Mach number decreases indicates that the incoming boundary layer is evolving towards turbulent. This means that the boundary layer is more resistant to separation, decreasing the separation shock scaling, but not necessarily the region of unsteady motion. The narrow peaks of the *α* = -5° at *x/d* = 8 and 10 spread over 1.7*d* and 1.6*d*, respectively. Both these cases have a constant and relatively steady *UI* shock (γ_{UI} > 0.9), with *α* = -5° at *x/d* = 8 in particular behaving more like a laminar interaction than a turbulent interaction with the largest separation scaling

and smallest standard deviations (σ_{UI} = 0.19, $\sigma_{\lambda 1}$ = 0.3) of the four transitional interaction cases.

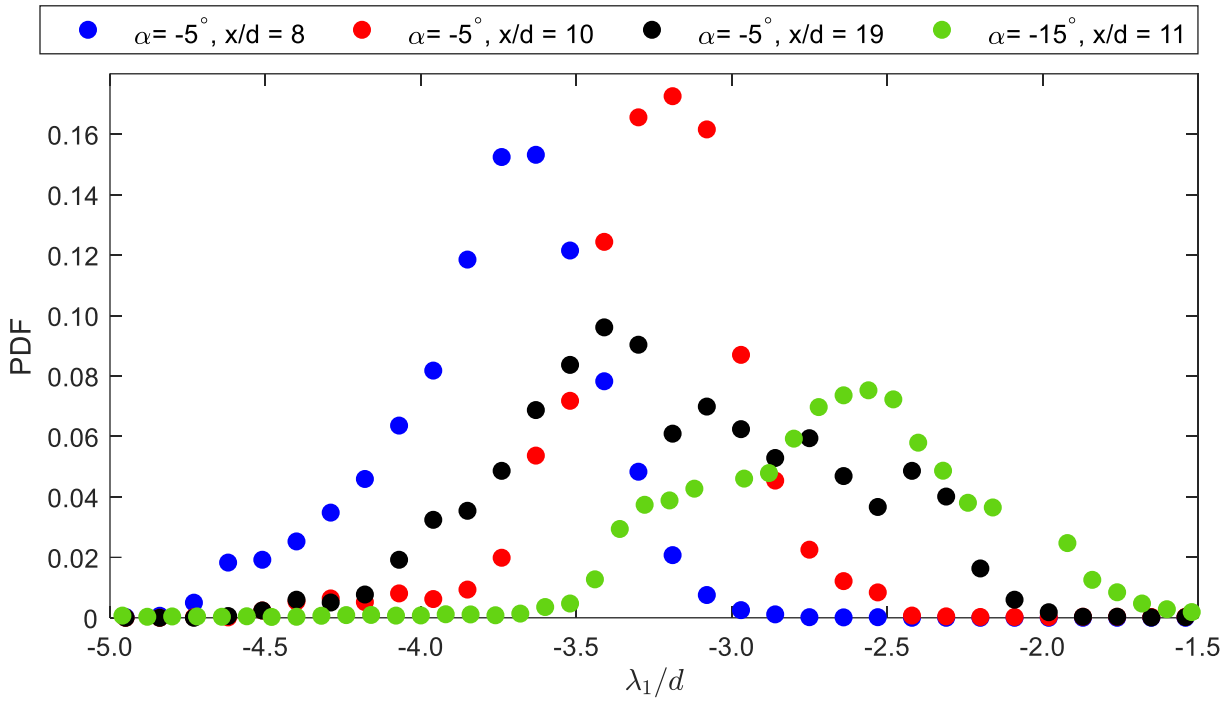

Figure A.10. PDFs of the separation shock motion for those test conditions when the *UI* shock is present.

Finally, the PDFs of the *UI* shock for the same transitional interaction test configurations as described in Figure A.10 are shown in Figure A.11. In this instance, the PDFs form two groups based on both the mean position of the *UI* shock and the spread of the probability. These two groups are α = -5° at *x/d* = 8 and 10, and α = -5° at *x/d* = 19 and α = -15° at *x/d* = 11. The first group has γ_{UI} values greater than 0.9, the second group less than 0.5. Transitional interaction groupings based on γ_{UI} were previously observed in Figure 3.15 for the cylinder and blunt fin shock generators in the Mach 2 facility. The evolution of the boundary layer in the transition region impacts the characteristic unsteady dynamics of the *UI* and separation shocks through the intermittent turbulent spots that develop and interact with the shock waves. This effect was not previously observed in the

Mach 2 facility owing to the high Reynolds number and the boundary layer tripping at the flat plate leading edge. This evolution of characteristic behavior derives from an almost ever-present *UI* shock with a weak separation shock, to an intermittent *UI* shock with a strong separation shock, to eventually, no *UI* shock with a strong separation shock for a fully turbulent interaction.

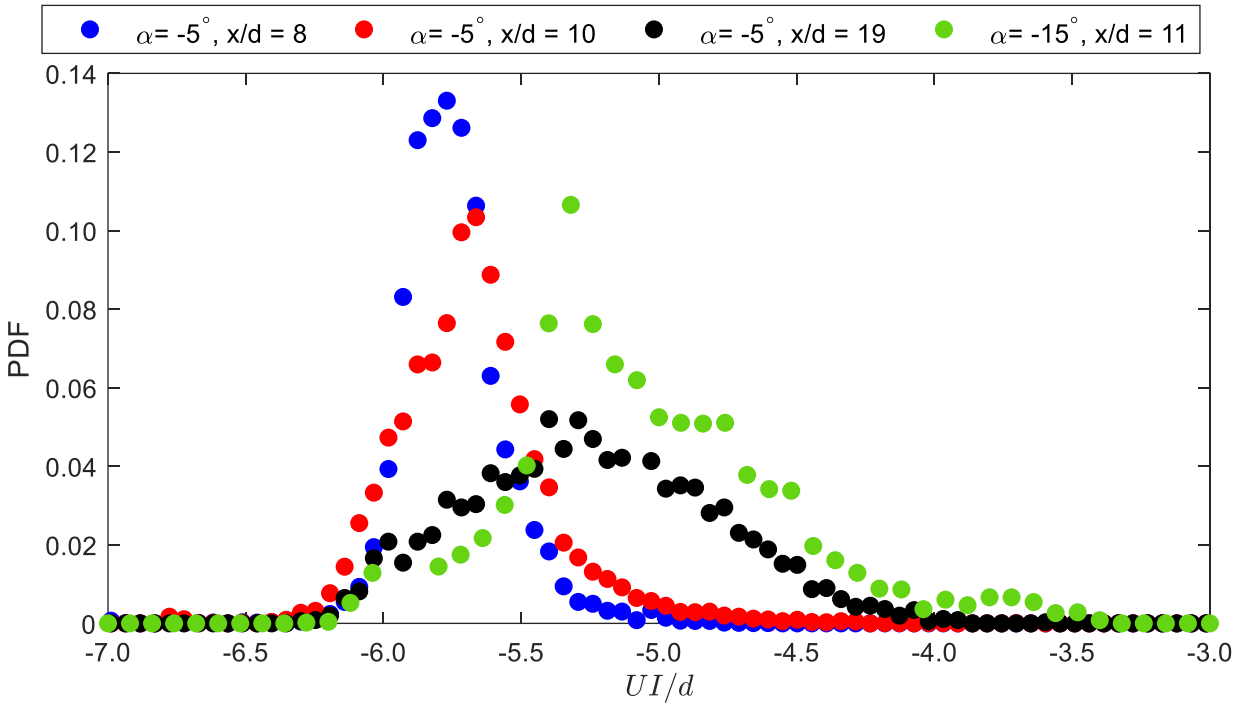

Figure A.11. PDFs of the *UI* shock for Mach 4 freestream configurations.

One of the more interesting results from this test campaign was the almost laminar-like interaction behavior of the *α* = -5°, *x/d* = 8 test case. At this time, a fully laminar interaction was not observed in either the Mach 2 or the Mach 4 freestream facilities. Some of these observations were already discussed as a part of the PDFs for the separation shock and *UI* shock in Figure A.10 and Figure A.11, respectively. One of the departures from the Mach 2 facility experiments was the larger scaling of the separation shock. Whereas even for transitional interaction cases when the *UI* shock was -5*d*

upstream of the cylinder or blunt fin in the Mach 2 facility, the separation shock mean remained around -2*d* to -2.5*d*, a characteristic of turbulent interactions. However, the mean separation shock position for α = -5°, *x/d* = 8 was -3.8*d* and the mean *UI* shock position was -5.7*d*. An additional observation was the separation shock behavior coalescing from the expansion waves to form the shock wave. A sample schlieren image sequence demonstrating this is provided in Figure A.12. In the first three frames, the separation shock appears just as distinct and strong as the *UI* shock; in subsequent frames, it is difficult to discern at all as a separate flow feature. As time progresses, however, waves appear between the *UI* shock and λ_1, until the separation shock dissipates almost entirely and only waves emanating from the separated boundary layer are visible between the *UI* shock and closure shock, λ_2, after 180 μ*s*.

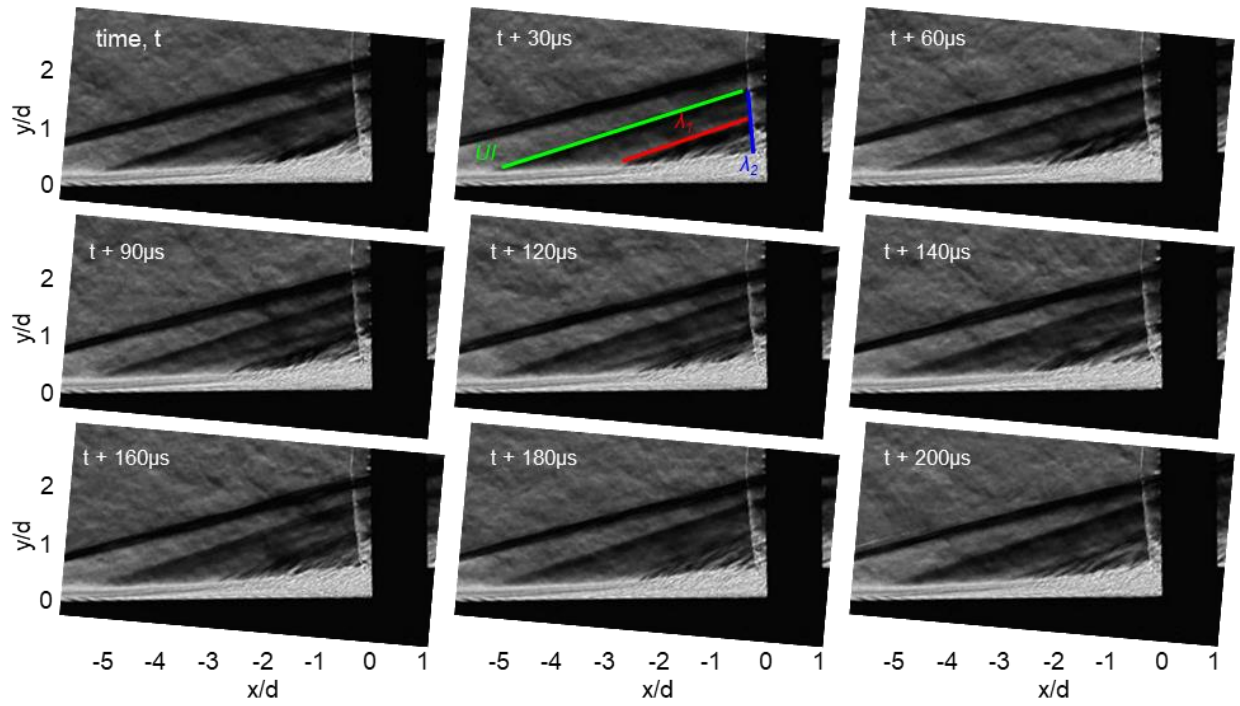

Figure A.12. Schlieren montage of a transitional interaction for α = -5°, *x/d* = 8 showing the different behavior of the separation shock. Flow is from left to right and the images have been rotated.

The boundary layer is difficult to resolve near the top surface of the flat plate model, but an increase in boundary layer thickness is still evident upstream of the separation shock near the foot of the *UI* shock.

Finally, the normalized power spectral densities (PSD) of the separation shock are provided in Figure A.13a for the transitional interaction cases. These spectra do not show the same high-intensity resonance observed in the Mach 2 facility. This is most likely due to the smaller Reynolds number across all flat plate angles, but particularly for the α = -30° case with matching edge Mach numbers (as previously discussed only turbulent interactions were observed at this flat plate angle). This is unusual as lower Reynolds numbers should make the boundary layer more resistant to transition. The spectra for the separation shock in the Mach 4 freestream transitional interaction cases mirror those from the literature for turbulent interactions with the high frequencies rolling off with no signs of resonance in the mid-frequency range. The corresponding spectra for the *UI* shock are provided in Figure A.13b. There is a local maximum of St = 0.03 (1.6 kHz) for the α = -5°, x/d = 8, but its magnitude does not indicate the same resonance observed in the Mach 2 facility.

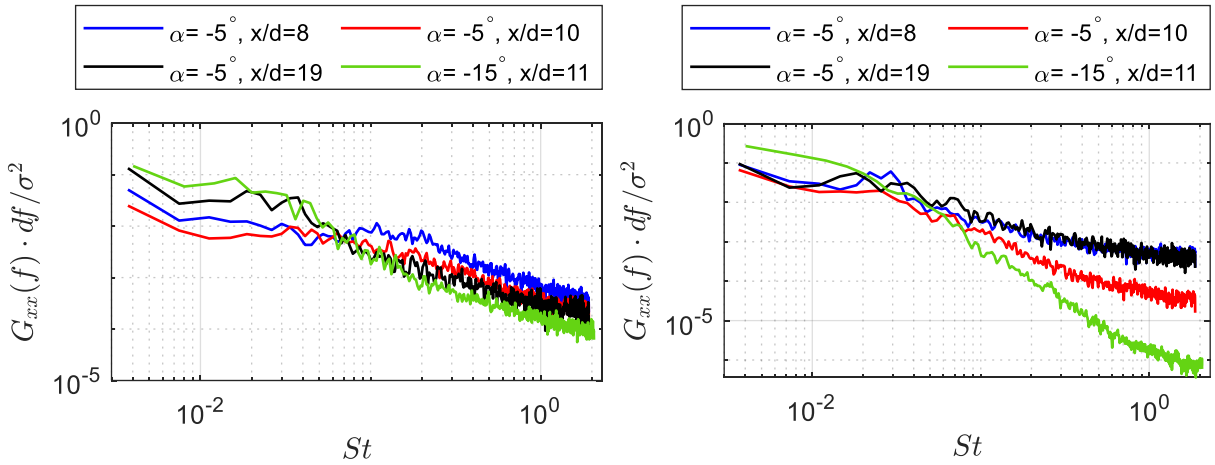

Figure A.13. Normalized PSD of the (a) separation shock motion and (b) the *UI* shock motion for those test conditions where the *UI* shock is present.

Although the flat plate angled at α = -30° did not duplicate the high-intensity resonance in the oscillation of the *UI* and separation shocks observed in the Mach 2 facility due to the significantly lower Reynolds number, some interesting trends in the shock behavior were captured for transitional boundary layers of varying edge Mach numbers and Reynolds numbers. Specifically, transitional interaction behavior closer to the onset of boundary layer transition as well as fully turbulent interactions were captured during the course of these tests. The expected behavior from the different combinations of edge Mach number and Reynolds number were observed in the statistics of the shock motion through their mean positions and probability distribution functions. The normalized power spectral densities of both the separation and *UI* shock motion for the transitional interactions did not show any high-intensity resonance as observed for transitional interactions in the Mach 2 facility. One reason for this is the competing effect of a lower Reynolds number. As previously mentioned, the boundary layer would be more resistant to transition, but it would also increase in thickness.

Mach 4 Facility Experimental Conclusions

Through the use of different wind tunnel models and diagnostic techniques, the presence of the high-intensity resonance of the *UI* shock, boundary layer separation precursor and separation shock were determined to be real phenomena of the flowfield for incoming transitional boundary layer interactions, when the edge Mach number was 1.8 and the Reynolds number was 30×10^6 m^{-1}. In addition, a Mach 4 freestream facility was used for further experiments. In order to determine if the oscillatory effect of the separation shock motion could be duplicated in a different facility with a different Reynolds number, but same edge Mach number, a series of flat plate experiments at varying angles of attack were performed. The highest Reynolds number available in the Mach 4 freestream facility was approximately 2×10^6 m^{-1}. Three flat plate angles of α = -5°, -15°, and -30° produced edge Mach numbers of 3.6, 2.9, and 1.8, respectively. Although transitional interactions that were characteristic of occurring closer to the laminar-side of transition were generated, the Reynolds number for the same edge Mach number of 1.8

was too low to match the flowfield conditions of the Mach 2 freestream and only turbulent interactions were observed. The Reynolds number is controlled in the Mach 4 freestream facility by varying the number and thickness of mylar plastic diaphragms that separate the high-pressure driver tube and the low-pressure test section. No combination of available diaphragms could produce a transitional boundary layer when the flat plate was angled -30°. Clearly, the sonic line within the boundary layer affects the characteristic response of the shock wave dynamics.

The combination of varying Reynolds numbers and edge Mach numbers did reveal some evolving shock wave characteristics, however. These characteristics support the hypothesis of both laminar and turbulent interaction features being present in transitional interactions. The lower Reynolds number and higher edge Mach number of 3.6 generated an almost laminar-like interaction, with the *UI* shock scaling up to -6*d*, compared to -4*d* in the Mach 2 freestream experiments. One interesting result from the Mach 4 freestream experiments is that the separation shock decreasing in scale was captured, until it leveled off at approximately -2.5*d*, matching the separation distances from the Mach 2 freestream studies. The normalized PSDs for all configurations presented broadband fluctuations that matched those from surface pressure transducers in the literature [40].

VITA

E. Lara Lash was born in Springfield, IL in 1991, and was raised in Vienna, VA by her parents, Dr. Terry R. Lash, Ph.D., and Ms. Elizabeth M. Vogt, Esq., with her older brother, Benjamin F. Lash. She attended Westbriar Elementary, Joyce Kilmer Middle School, and completed high school at George C. Marshall in Northern Virginia in June of 2009 with an International Baccalaureate diploma. In August 2009, she enrolled in Lafayette College in Easton, PA, where she graduated with a Bachelor of Science in Mechanical Engineering and a minor in History in May of 2013. During her tenure at Lafayette, she studied abroad at Jacobs University Bremen in Bremen, Germany, for the Spring 2011 semester. In August of 2013, she enrolled at the University of Tennessee Space Institute (UTSI) to begin her graduate work, earning her Masters of Science in Aerospace Engineering, in May 2015. In October 2015, she joined the HORIZON Research Group under Dr. John Schmisseur and began work for a Ph.D. at UTSI.